COMPUTATIONAL STUDIES OF THE DEHALOGENATION OF AROMATICS

A THESIS

SUBMITTED TO THE FACULTY OF THE GRADUATE SCHOOL

OF THE UNIVERSITY OF MINNESOTA

BY

DANIEL D. SADOWSKY

IN PARTIAL FULFILLMENT OF THE REQUIREMENTS

FOR THE DEGREE OF

DOCTOR OF PHILOSOPHY

CHRISTOPHER J. CRAMER AND KRISTOPHER MCNEILL

August, 2014

Acknowledgements

Above all, I would like to thank my advisors, Profs. Cramer and McNeill, for their many years of support, encouragement, and patience. As all of the chapters of this thesis are taken either in whole or in part from publications co-authored with them or manuscripts soon to be submitted for publication with them as co-authors, it should also be noted that the text itself is also indebted to them.

Many of the chapters were significantly improved thanks to discussions with colleagues at the University of Minnesota and at ETH Zurich too numerous to mention. The feedback of an anonymous reviewer contributed significantly to the improvement of chapter 3, and discussions with Sam Arey (EPFL) contributed significantly to the improvement of chapter 5.

I would also like to acknowledge the Minnesota Supercomputing Institute for the allocation of high-performance computing resources.

Abstract

The chemical properties affecting dehalogenation reactions occurring by homolytic bond cleavage and hydride transfer are investigated for halogenated aromatics. Gas phase bond dissociation enthalpies and standard enthalpies of formation, aqueous bond dissociation free energies and Gibbs free energies of formation, aqueous Gibbs free energies of dehalogenation, and aqueous two-electron reduction potentials are predicted for benzene and the 36 (poly)fluoro-, (poly)chloro-, and (poly)bromo- benzenes using a validated density functional protocol combined with continuum solvation calculations when appropriate. The nucleophilic aromatic substitution reactions of halogenated aromatics in aqueous solution are investigated, as is the binding of halogenated aromatics to model complexes simulating a rough Rh/Al_2O_3 catalyst. A computational methodology is presented that could be used to extend these studies to highly condensed aromatic systems.

Contents

List of Tables

List of Figures

Chapter 1

Introduction

Halogenated aromatics represent an important class of environmental contaminants for which the exploration of chemical and biological remediation mechanisms has been a particularly active area of research [1–3]. Fluoroaromatics constitute an emerging class of pharmaceuticals, agricultural chemicals, surfactants, and other chemicals of industrial origin [1, 4–6]. Chloroaromatics are ubiquitous environmental contaminants that have historically been used in dissipative applications [2, 7, 8]. Bromoaromatic pollutants include dyes, agricultural chemicals, and especially flame retardants [3, 9–13].

1.0.1 Homolytic Bond Cleavage

One important pathway for the dehalogenation of aromatic compounds is the homolytic cleavage of carbon-halogen bonds. This can be achieved, for example, through thermochemical and sonochemical [14] processes. While thermal treatments of halogenated aromatic materials are often undesirable as they require extreme conditions and have the potential to generate toxic by-products [15], thermochemical dehalogenation has achieved some success in practical applications where conditions are carefully controlled [16–18]. In the case of sonochemical applications, complete mineralization of various chlorinated benzenes in water has been reported [19, 20], and it has also been demonstrated that, for fluorobenzene, chlorobenzene, bromobenzene, and iodobenzene, sonochemical degradation is initiated by homolytic cleavage of the carbon-halogen bond, resulting in benzene as the product (although in the case of fluorobenzene, the cleavage of weaker carbon-hydrogen bonds also leads to polymeric by-products) [21].

Owing to their wide use to elucidate a fundamental understanding of the thermodynamics of the chemical transformations of organic molecules [22, 23] and their special importance to reactions involving homolytic cleavage, an analysis of the gas phase bond dissociation enthalpies and aqueous bond dissociation free energies of all carbon-hydrogen and carbon-halogen bonds for benzene and the (poly)fluoro-, (poly)chloro-, and (poly)bromo- benzenes is undertaken in chapter 3. In doing this, the gas phase enthalpies of formation and aqueous free energies of formation are predicted using an

isodesmic formalism. As the thermodynamics of reactions also give insight into the microbial processes through which they are catalyzed [24], the Gibbs free energies of reaction, with dihydrogen as the electron donor, as well as two-electron reduction potentials against the standard hydrogen electrode are predicted for all possible hydrodehalogenation reactions of the substrates studied.

1.0.2 Hydride Transfer

Another important pathway for the dehalogenation of aromatic compounds is hydride transfer. One simple but energy intensive way that dehalogenation through hydride transfer has been accomplished is through a hydride-halide exchange reaction with metal hydrides [25, 26]. Additionally, there are many transition metal based catalytic systems which can achieve hydrodehalogenation by binding hydrogen and transferring it from the metal center to the aromatic substrate [27–29]. In some systems [28], the carbon-halogen bond is broken by oxidative addition, initiating a cycle that is completed with hydride transfer to the aryl group. In other systems, the nucleophilic attack of the halogenated aromatic by a hydride donor initiates the process. The latter can occur through two different mechanisms. In one mechanism, the hydride attacks a halogen substituted carbon, resulting in hydrodehalogenation in a single concerted step. In a second mechanism, a hydride attacks a halogenated substrate at an unsubstituted site, resulting in the formation of a stable anionic σ-complex. In the latter case, the anionic complex is typically subject to rapid protonation, and can subsequently undergo

β-elimination, resulting in net hydrodehalogenation in two steps. There is evidence that microbial degradation of nitroaromatics proceeds through stepwise hydride transfer [30–32], but we are unaware of any evidence for similar microbial pathways for the degradation of halogenated aromatics. These reactions are studied for the case of the (poly)fluoro-, (poly)chloro-, and (poly)bromo- benzenes in chapter 4.

1.0.3 Rh/Al_2O_3 Catalysis

Several approaches to the use of transition metal compounds to catalyze the dehalogenation of aromatics have been explored [33–35], including recent studies from our laboratory on the catalytic dehalogenation of halogenated benzenes with a Rh/Al_2O_3 catalyst in aqueous solution [36,37]. The later set of studies has produced some interesting but unexplained results; the binding of (poly)fluoro- and (poly)chloro- benzenes to model Rh complexes are studied and compared to this experimental system in chapter 5.

1.0.4 Extensions to Larger Systems

Although substituted benzenes are the only aromatic compounds studied in chapters 3, 4, and 5, there are also many halogenated *polycyclic* aromatic hydrocarbon pollutants which have been detected in the environment and have been shown to have considerable toxicity [38–42]. Moreover, the recent advent of halogenated graphene materials

introduces the possibility of even more highly condensed halogenated aromatic environmental pollutants [43, 44]. While application of the computational modeling techniques discussed in chapters 3, 4, and 5 to the former compounds should be relatively straight forward, the use of electronic structure theory to study the later materials poses particular difficulties owing to their extreme open-shell character. In chapter 6, a theoretical methodology is developed to study large, curved polycyclic aromatics which could be used in future computational studies of these fascinating new materials.

Chapter 2

Nomenclature[1]

The (poly)halogenated benzenes are identified here in accordance with IUPAC conventions, except in tables, where they are identified by their congener class. Each congener class is defined by halogen substitution patterns and is identified by the prefix corresponding to its number of halogen substitutions and additionally, where necessary, by its locant, as detailed in Figure 2.1.

[1] **Adapted with permission from Sadowsky, D.; McNeill, K.; Cramer, C. J. Thermochemical Factors Affecting the Dehalogenation of Aromatics. *Environ. Sci. Technol.*, 2013, *47*, 14194–14203. Copyright 2013 American Chemical Society.**

Figure 2.1: (Poly)halogenated benzene congeners

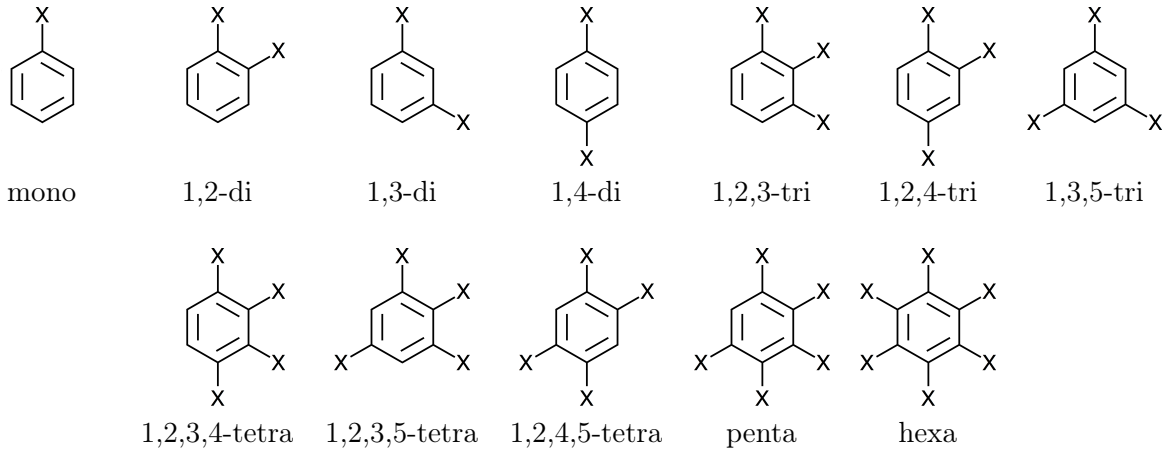

Chapter 3

Thermochemistry[1]

3.1 Introduction

Halogenated aromatics represent an important class of environmental contaminants for which the exploration of chemical and biological remediation mechanisms has been a particularly active area of research. Chlorinated aromatics have perhaps received the most attention, as they are ubiquitous environmental contaminants that have historically been used in dissipative applications [2, 7, 8]. However, the rapidly increasingly levels of brominated organic pollutants, especially flame retardants, in the environment has also been given much attention in recent decades [3, 9–13], and fluorinated aromatics potentially constitute an emerging class of pollutants that include agricultural chemicals and several widely used pharmaceutical products [1, 6].

[1] **Adapted with permission from Sadowsky, D.; McNeill, K.; Cramer, C. J. Thermochemical Factors Affecting the Dehalogenation of Aromatics. *Environ. Sci. Technol.*, 2013, *47*, 14194–14203. Copyright 2013 American Chemical Society.**

Gas-phase standard enthalpies of formation are widely used in the modeling of thermal reactions in atmospheric chemistry [45] and the kinetic modeling of combustion processes [46]. Furthermore, the bond dissociation enthalpies (BDEs) which are derived from these quantities are widely used in explaining chemical phenomena. Taking benzene and the 36 possible (poly)fluoro-, (poly)chloro-, and (poly)bromobenzene congeners as a set representative of this class of compounds, density functional theoretical (DFT) calculations are undertaken in order to predict key physical properties relevant to dehalogenation. Gas-phase standard enthalpies of formation are predicted for all 37 members of the set as well as the 58 radicals which can be formed by homolytic cleavage of a carbon-hydrogen bond of a member of the set. From these results, an analysis of carbon-hydrogen and carbon-halogen BDEs is undertaken. Aqueous Gibbs free energies of formation are also predicted, as well as free energies of hydrodehalogenation and two-electron reduction potentials, which can be useful in understanding the susceptibility of environmental pollutants to microbial degradation [47, 48].

3.2 Materials and Methods

3.2.1 Computational Methods

All DFT calculations are done at the hybrid meta-generalized-gradient level of density functional theory, using the M06-2X functional [49], the standard 6-311+G(3df,2p) basis set, and an integration grid of 99 radial shells and 590 angular points per shell. The

M06-2X functional has been extensively benchmarked and was chosen by reason of its high accuracy for organic compounds [50–53]. The geometry of each structure is optimized to a maximum force of $2.0 \cdot 10^{-6}$ au, a root mean square (RMS) force of $1.0 \cdot 10^{-6}$ au, a maximum internal coordinate displacement of $6.0 \cdot 10^{-6}$ au, and a RMS internal force displacement of $4.0 \cdot 10^{-6}$ au. All optimized geometries are confirmed to be local minima on the model chemistry potential energy surface by analytical calculation of the vibrational frequencies following the usual quantum-mechanical harmonic-oscillator approximation. These vibrational frequencies are scaled by a factor of 0.970, a parameter that has been empirically fit for M06-2X to reproduce experimental zero-point vibrational energies [54], and used in the calculation of zero-point vibrational energies and vibrational partition functions. These quantities, along with the ideal-gas, particle-in-a-box, and rigid-rotator partition functions, are used to calculate thermal contributions to the enthalpy and Gibbs free energy of each structure using the thermo.pl script [55]. Aqueous solvation energies are calculated with the SMD [56] implicit solvation model, and thermal contributions to thermochemical quantities in solution are calculated from additional analytical frequency calculations with the SMD model chemistry [**?**]. All CCSD(T) calculations [57] are done with a Douglas-Kroll-Hess (DKH) 2nd order scalar relativistic Hamiltonian [58–60], point nuclei, and the DKH contracted aug-cc-pVTZ basis [61]. All calculations are performed with the Gaussian 09 electronic structure suite, Revision C.01 [62].

3.2.2 Statistical Methods

The R software environment, version 2.15.2 [63] is used for all linear regression analysis.

3.3 Results and Discussion

3.3.1 Standard Enthalpies of Formation

Gas-phase standard enthalpies of formation are predicted at 298.15 K and 1 atm pressure. One manner in which to take advantage of error cancellation in a given model chemistry is to compute the enthalpies of formation through the use of homodesmotic reactions such as the one in Eq. B.1, where the compound of interest, having n halogen substituents, is formed along with $n - 1$ molecules of benzene from the combination of n molecules of either fluorobenzene, chlorobenzene, or bromobenzene (we follow here the convention established by Wheeler et al. [64] for the definition of the word homodesmotic and related terms). The standard enthalpy of this reaction, defined in terms of reactant and product heats of formation in Eq. 3.2, can also be determined from the calculated enthalpies at the given model chemistry (which reference a zero of enthalpy corresponding to infinite separation of all particles in a vacuum). Combining these as in Eq. 3.3 provides an expression for the standard enthalpy of formation for the species of interest in terms of the enthalpy of reaction calculated at the given model chemistry (designated here as DFT) and the enthalpies of formation of benzene and the singly halogenated benzene references taken from experiment.

$$n\,\mathrm{C_6H_5X} \longrightarrow (n-1)\,\mathrm{C_6H_6} + \mathrm{C_6H_{6-n}X_n} \tag{3.1}$$

$$\Delta_r H^\circ = (n-1)\Delta_f H^\circ(C_6H_6) + \Delta_f H^\circ(C_6H_{6-n}X_n) - n\Delta_f H^\circ(C_6H_5X) \tag{3.2}$$

$$\Delta_f H^\circ(C_6H_{6-n}X_n) = \Delta_r H^\circ_{(DFT)} - (n-1)\Delta_f H^\circ_{(exp.)}(C_6H_6) + n\Delta_f H^\circ_{(exp.)}(C_6H_5X) \tag{3.3}$$

No attempt is made here to estimate the uncertainty inherent in the electronic structure methods used, although this has been quantified elsewhere for homodesmotic reaction energies with M06-2X [64]. The uncertainty owing exclusively to the use of experimental values as references however, can be derived using the rules for the propagation of uncertainty and a value of zero for the uncertainty of the DFT enthalpy of reaction, as is done in Eq. 3.4. Values for the enthalpy of formation of benzene from the recent literature, which include a value derived from the review of experimental data for the liquid enthalpy of formation and enthalpy of vaporization [65], a value calculated using the High accuracy Extrapolated Ab initio Thermochemistry (HEAT) protocol [66], and a value obtained using photoelectron photoion coincidence spectroscopy and an Active Thermochemical Tables analysis from Stevens et al. [67], are all in good agreement. The

latter value, 19.9 $\pm$0.1 kcal mol^{-1}, is selected because of its experimental origin, low uncertainty, and because it was reported along with values for the enthalpies of formation of phenyl radical and all of the monohalogenated benzenes using the same method.

$$\sigma_{\Delta_f H^\circ(C_6H_{6-n}X_n)} = \sqrt{(n-1)^2\sigma^2_{\Delta_f H^\circ(C_6H_6)} + n^2\sigma^2_{\Delta_f H^\circ(C_6H_5X)}} \tag{3.4}$$

The use of the homodesmotic reaction in Eq. B.1 can be expected to result in a good canceling of errors, and has been shown to give accurate standard enthalpy of formation predictions for M06-2X based model chemistries [64]. It has also been shown that hyperhomodesmotic reactions such as the one in Eq. 3.5 offer a slightly better cancelation of errors in most cases [64], although the particular reaction considered in Eq. 3.5 requires reliable experimental values for two halogenated benzene references, which do not exist in all cases. The variable q in Eq. 3.5 refers to the number of *pairs* of halogen substitutions *ortho* to one another.

$$6(n-q)\,\mathrm{C_6H_5X} + q\,\mathrm{C_6X_6} \longrightarrow (6n-5q-6)\,\mathrm{C_6H_6} + 6\,\mathrm{C_6H_{6-n}X_n} \tag{3.5}$$

In the case of the (poly)fluorobenzenes, experimental values are available for selected congeners from separate rotating bomb calorimetry studies [68–70], and these values have been reviewed by Pedley [71]. A value for the standard enthalpy of formation for fluorobenzene which agrees with the value reported by Pedley, but with lower uncertainty, is also available from the work of Stevens et al., and this value is used to

predict the enthalpies of formation using the homodesmotic formalism. In addition, the calorimetry value for hexafluorobenzene is reported to have an uncertainty of 0.3 kcal mol^{-1} by Pedley, and is therefore an attractive choice for use as a second reference in the hyperhomodesmotic reaction in Eq. 3.5. Both the homodesmotic and hyperhomodesmotic predictions are reported in Table 3.1, along with the known experimental values and a previous set of theoretical predictions that have been reported [72]. The mean signed differences (MSD) and root mean squared differences (RMSD) between each set of theoretical predictions and the set of experimental values are also reported. Theoretical values that predict experimental values by design (for example, all of the predictions for fluorobenzene) are omitted from the calculation of these statistical measures and are reported in italics. The equations that are used to calculate the predicted enthalpies of formation and the uncertainties owing to the use of experimental references for the hyperhomodesmotic reaction and all subsequently proposed homodesmotic reactions are explicitly derived in Appendix A.

The set of predictions from the hyperhomodesmotic reaction in Eq. 3.5 show a smaller deviation from the experimental values than those calculated using the homodesmotic reaction in Eq. B.1, presumably due to a better canceling of errors. The agreement of the predictions from the hyperhomodesmotic reaction with the experimental data also suggests that the different sources of experimental data are in good agreement with each other. The exception to this is the value for 1,2,4,5-tetrafluorobenzene from Harrop and Head, which was rejected by Pedley in his review of the values.

Table 3.1: Comparison of experimental and calculated gas-phase enthalpies of formation for (poly)fluorobenzenes (in kcal mol^{-1}).

	Experiment	Gomes et al.[a]	Homodesmotic[b]	Hyperhomodesmotic[c]
benzene	19.7 ± 0.2[d]	*19.7 ± 0.2*[d]	*19.9 ± 0.1*[e]	*19.9 ± 0.1*[e]
	19.9 ± 0.1[e]			
mono	-27.7 ± 0.3[d]	*-27.7 ± 0.3*[d]	*-27.6 ± 0.2*[e]	*-27.6 ± 0.2*[e]
	-27.6 ± 0.2[e]			
1,2-di	-70.2 ± 0.2[d]	-70.8 (± 0.7)	-70.6 ± 0.5	-70.2 ± 0.2
1,3-di	-73.9 ± 0.2[d]	-74.5 (± 0.7)	-74.4 ± 0.5	-74.4 ± 0.5
1,4-di	-73.3 ± 0.2[d]	-73.8 (± 0.7)	-73.8 ± 0.5	-73.8 ± 0.5
1,2,3-tri		-113.4 (± 1.1)	-112.9 ± 0.7	-112.0 ± 0.3
1,2,4-tri		-116.4 (± 1.1)	-116.2 ± 0.7	-115.7 ± 0.5
1,3,5-tri		-120.4 (± 1.1)	-120.6 ± 0.7	-120.6 ± 0.7
1,2,3,4-tetra		-154.8 (± 1.5)	-154.4 ± 1.0	-153.0 ± 0.3
1,2,3,5-tetra		-158.2 (± 1.5)	-157.9 ± 1.0	-157.0 ± 0.5
1,2,4,5-tetra	-154.6 ± 0.8[f]	-157.7 (± 1.5)	-157.5 ± 1.0	-156.5 ± 0.5
penta	-192.8 ± 0.4[d]	-195.5 (± 1.9)	-194.8 ± 1.2	-192.9 ± 0.3
hexa	-228.4 ± 0.3[d]	-232.1 (± 2.2)	-231.2 ± 1.5	*-228.4 ± 0.3*[d]
MSD	-	-1.9	-1.5	-0.6
RMSD	-	2.3	1.9	0.9

[a] Values taken from Gomes et al. (Ref. 72). Uncertainties calculated using Eq. 3.4.
[b] Values calculated using Eqs. 3.3 and 3.4.
[c] Values calculated using equations derived from Eq. 3.5. See SI for details.
[d] Values taken from Pedley (Ref. 71).
[e] Values taken from Stevens et al (Ref. 67).
[f] Value taken from Harrop and Head (Ref. 70).

In the case of the (poly)chlorobenzenes, experimental values for the enthalpy of formation of all congeners exist and have been reviewed by Pedley [71], whose recommendations draw largely from the calorimetry work of Platonov et al [73–76]. For the three trichlorobenzene congeners, an additional set of values has been reported by Yan et al. [77], although these values vary from the values recommended earlier by Pedley by as much as 3.1 kcal mol^{-1}. Several authors have noted the difficulty that chlorinated hydrocarbons pose to accurate calorimetry and urge caution when considering sets of experimental values from individual laboratories [78–80]. With the exception of chlorobenzene, where Pedley's value has been confirmed both by computation [81] and the work of Stevens et al., there are no (poly)chlorobenzene congeners for which replication of measurements by different research groups has produced values in agreement with each other. This makes the homodesmotic formalism, which requires only the values of benzene and chlorobenzene as references, much more attractive than the hyperhomodesmotic formalism. The chlorobenzene value reported by Stevens et al. was chosen as the experimental reference for this formalism, as the uncertainty of 0.1 kcal mol^{-1} associated with this value is a considerable improvement over the 0.3 kcal mol^{-1} uncertainty in the value reported by Pedley. The standard enthalpies of formation predicted using the homodesmotic formalism are reported in Table 3.2 along with the experimental values from Pedley, Stevens et al., and Yan et al., and a previous set of theoretical predictions that exist in the literature, those of León et al. [79]. We do not know how the uncertainties reported in this set of predictions were calculated, but they

Table 3.2: Comparison of experimental and calculated gas-phase enthalpies of formation for (poly)chlorobenzenes (in kcal mol^{-1}).

	Experiment	León et al.[a]	Homodesmotic[b]
benzene	19.7 ± 0.2[c]	*19.7 ± 0.2*[c]	*19.9 ± 0.1*[d]
	19.9 ± 0.1[d]		
mono	12.4 ± 0.3[c]	*12.4 ± 0.3*[c]	*12.5 ± 0.1*[d]
	12.5 ± 0.1[d]		
1,2-di	7.2 ± 0.5[c]	8.1 ± 0.5 (±0.6)	7.6 ± 0.3
1,3-di	6.1 ± 0.5[c]	6.1 ± 0.5 (±0.6)	6.1 ± 0.3
1,4-di	5.4 ± 0.4[c]	5.4 ± 0.5 (±0.6)	6.0 ± 0.3
1,2,3-tri	0.9 ± 0.2[c]	4.6 ± 0.6 (±1.0)	3.4 ± 0.5
	2.0 ± 0.4[e]		
1,2,4-tri	-1.9 ± 0.2[c]	2.2 ± 0.6 (±1.0)	1.7 ± 0.5
	1.2 ± 0.4[e]		
1,3,5-tri	-3.2 ± 0.2[c]	0.1 ± 0.6 (±1.0)	0.4 ± 0.5
	-0.6 ± 0.3[e]		
1,2,3,4-tetra	-6.1 ± 0.2[c]	1.5 ± 0.7 (±1.3)	-0.4 ± 0.6
1,2,3,5-tetra	-8.3 ± 0.2[c]	-0.8 ± 0.7 (±1.3)	-1.8 ± 0.6
1,2,4,5-tetra	-7.8 ± 0.2[c]	-1.1 ± 0.7 (±1.3)	-2.2 ± 0.6
penta	-9.6 ± 2.1[c]	-1.4 ± 0.8 (±1.7)	-3.6 ± 0.8
hexa	-8.5 ± 2.2[c]	-1.1 ± 0.8 (±2.0)	-4.8 ± 0.9
MSD[f]	-	4.5	3.5
RMSD[f]	-	5.4	4.1
MSD[g]	-	1.5	1.0
RMSD[g]	-	1.7	1.1

[a] Ref. 79 (uncertainties in parentheses calculated from Eq. 3.4)
[b] Values calculated using Eqs. 3.3 and 3.4.
[c] Values taken from Pedley (Ref. 71)
[d] Values taken from Stevens et al. (Ref. 67)
[e] Values taken from Yan et al. (Ref. 77)
[f] Differences between calculated values and the experimental values from Ref. 71 ($n = 11$)
[g] Differences between calculated values and the experimental values from Ref. 77 ($n = 3$)

do not agree with the formalism proposed in Eq. 3.4. For comparison, both the reported uncertainties and the uncertainties re-calculated with Eq. 3.4 are given. Interestingly, the predictions from both León et al. and from this work are in better agreement with the work of Yang et al. than with the values reported by Pedley.

In the case of the (poly)bromobenzenes, Stevens et al. report a value for the enthalpy of formation of bromobenzene which is in agreement with the early value of Pedley but with considerably less uncertainty (0.3 kcal mol^{-1} as opposed to 1.0 kcal mol^{-1}). As these are the only experimental values for the (poly)bromobenzenes available with

known uncertainty, the use of the homodesmotic formalism is necessary. As bromine is significantly heavier than fluorine or chlorine, the validity of our non-relativistic model chemistry for predicting standard enthalpies of formation of brominated aromatics is tested. DFT and CCSD(T) single point calculations with a 2nd order scalar relativistic DKH Hamiltonian are considered for select high-symmetry bromobenzenes, the details of which can be found in Appendix B. The calculations indicate that the use of the homodesmotic equation ensures a sufficient cancellation of errors such that the use of a relativistic Hamiltonian and/or a more sophisticated treatment of electronic correlation is not necessary. The standard enthalpies of formation predicted for the (poly)bromobenzenes with the homodesmotic formalism are reported in Table 3.3, along with the recommended predictions for the (poly)fluoro- and (poly)chlorobenzenes.

Table 3.3: Predicted gas-phase standard enthalpies of formation of (poly)halogenated benzenes and phenyl radicals (in kcal mol^{-1}).

	$\Delta_f H°(F)^a$	$\Delta_f H°(Cl)^b$	$\Delta_f H°(Br)^b$
mono	*-27.6 ± 0.2*[c]	*12.5 ± 0.2*[c]	*25.1 ± 0.3*[c]
1,2-di	-70.2 ± 0.2	7.6 ± 0.3	32.9 ± 0.6
1,3-di	-74.4 ± 0.5	6.1 ± 0.3	31.1 ± 0.6
1,4-di	-73.8 ± 0.5	6.0 ± 0.3	31.0 ± 0.6
1,2,3-tri	-112.0 ± 0.3	3.4 ± 0.5	41.8 ± 0.9
1,2,4-tri	-115.7 ± 0.5	1.7 ± 0.5	39.6 ± 0.9
1,3,5-tri	-120.6 ± 0.7	0.4 ± 0.5	37.9 ± 0.9
1,2,3,4-tetra	-153.0 ± 0.3	-0.4 ± 0.6	51.2 ± 1.3
1,2,3,5-tetra	-157.0 ± 0.5	-1.8 ± 0.6	49.0 ± 1.3
1,2,4,5-tetra	-156.5 ± 0.5	-2.2 ± 0.6	48.4 ± 1.3
penta	-192.9 ± 0.3	-3.6 ± 0.8	61.1 ± 1.6
hexa	*-228.4 ± 0.3*[d]	-4.8 ± 0.9	74.4 ± 1.9
2-mono	35.8 ± 0.3	75.0 ± 0.2	87.0 ± 0.3
3-mono	33.4 ± 0.3	73.5 ± 0.2	85.9 ± 0.3
4-mono	34.1 ± 0.3	74.0 ± 0.2	86.5 ± 0.3
2,3-di	-6.6 ± 0.3	69.9 ± 0.4	94.4 ± 0.7
2,4-di	-10.2 ± 0.5	69.2 ± 0.4	93.6 ± 0.7
2,5-di	-10.1 ± 0.5	68.7 ± 0.4	93.1 ± 0.7
2,6-di	-8.2 ± 0.5	70.2 ± 0.4	94.2 ± 0.7
3,4-di	-8.2 ± 0.3	69.3 ± 0.4	94.5 ± 0.7
3,5-di	-13.2 ± 0.5	67.2 ± 0.4	92.0 ± 0.7
2,3,4-tri	-47.9 ± 0.3	66.2 ± 0.5	103.7 ± 1.0
2,3,5-tri	-51.9 ± 0.5	64.2 ± 0.5	101.1 ± 1.0
2,3,6-tri	-49.4 ± 0.5	65.7 ± 0.5	102.2 ± 1.0
2,4,5-tri	-51.3 ± 0.5	65.0 ± 0.5	102.2 ± 1.0
2,4,6-tri	-53.5 ± 0.8	65.1 ± 0.5	101.5 ± 1.0
3,4,5-tri	-50.0 ± 0.3	65.2 ± 0.5	103.4 ± 1.0
2,3,4,5-tetra	-88.4 ± 0.3	62.6 ± 0.7	113.2 ± 1.3
2,3,4,6-tetra	-90.0 ± 0.5	62.5 ± 0.7	111.9 ± 1.3
2,3,5,6-tetra	-89.8 ± 0.5	64.7 ± 0.7	110.5 ± 1.3
2,3,4,5,6-penta	-125.8 ± 0.4	60.5 ± 0.8	123.3 ± 1.6

[a] Values calculated using equations derived from Eqs. 3.5 and 3.7. See SI for details.
[b] Values calculated using Eqs. 3.3 and 3.4, and equations derived from Eq. 3.6. See SI for details.
[c] Values taken from Stevens et al. (Ref. 67).
[d] Values taken from Pedley (Ref. 71).

The methodology used to predict enthalpies of formation above is extended to the radicals formed by homolytic cleavage of carbon-hydrogen bonds through the reactions in Eqs. 3.6 and 3.7 and the value of 80.6 ± 0.1 kcal mol^{-1} reported by Stevens et al. for phenyl radical. The reaction in Eq. 3.7, although analogous to the reaction in Eq. 3.5, is not a hyperhomodesmotic equation under the definition proposed by Wheeler et al., as it does not account for the difference between substituted and unsubstituted sp^2 carbons adjacent to the free valence. As no suitable values for fluorinated phenyl radicals are available for use as references in such a hyperhomodesmotic equation, recourse to the hybrid homodesmotic-hyperhomodesmotic reaction in Eq. 3.7 is necessary. For the chlorinated and brominated radicals, the homodesmotic formalism is used, analogous to the substituted benzene predictions. The predictions of the enthalpies of formation for all of the halogenated radicals are reported in Table 3.3.

$$C_6H_5^\bullet + n\,C_6H_5X \longrightarrow n\,C_6H_6 + C_6H_{5-n}X_n^\bullet \tag{3.6}$$

$$6\,C_6H_5^\bullet + 6(n-q)\,C_6H_5X + q\,C_6X_6 \longrightarrow (6n-5q)\,C_6H_6 + 6\,C_6H_{5-n}X_n^\bullet \tag{3.7}$$

The multiple linear regression model in Eq. 3.8 is proposed in order to investigate the additive contributions to the predicted standard enthalpies of formation. The (poly)halogenated benzenes and phenyl radicals are considered together in the model

by considering their enthalpies of formation in relation to the experimental values ($\Delta H_f^\circ(ref)$) of benzene and phenyl radical, respectively. No additional intercept terms appear in the model. The variables considered are the number of halogen substitutions (n_{C-X}), the number of *pairs* of halogen substitutions in *ortho* ($n_{o,X}$), *meta* ($n_{m,X}$), and *para* ($n_{p,X}$) positions with each other, and additionally in the case of the radicals, the numbers of halogen substitutions *ortho* ($n_{o,R}$), *meta* ($n_{m,R}$), and *para* ($n_{p,R}$) to the free valence. In the case of 2,4,5-trifluorophenyl radical, for example, there are three halogen substitutions ($n_{C-X} = 3$), the fluorines in positions 4 and 5 are *ortho* to each other ($n_{o,X} = 1$), the fluorines in positions 2 and 4 are *meta* to each other ($n_{m,X} = 1$), the fluorines in positions 4 and 5 are *para* to each other ($n_{p,X} = 1$), the fluorine in position 2 is *ortho* to the free valence ($n_{o,R} = 1$), the fluorine in position 5 is *meta* to the free valence ($n_{m,R} = 1$), and the fluorine in position 4 is *para* to the free valence ($n_{p,R} = 1$). As the fluorinated, chlorinated, and brominated congeners share only the reference values of benzene and phenyl radical in common, three separate regressions are considered. For each regression, the estimate and standard error for each parameter and the coefficient of determination (R^2) of the regression are reported in Table 3.4. The $c_{m,R}$ terms for the chlorinated (0.05 ± 0.05) and brominated (-0.11 ± 0.10) congeners have p-values greater than 0.05 (0.31 and 0.28, respectively). These parameters are therefore not significant at the 95% confidence level, and consequently only the regression for the fluorinated congeners was calculated with $n_{m,R}$ included as a variable (in which case the parameter $c_{m,R}$ has a p-value of 2.61×10^{-8}).

Table 3.4: Multiple linear regression of the predicted gas-phase standard enthalpies of formation (in kcal mol^{-1}) of the (poly)halogenated benzenes and phenyl radicals.

	c_{C-X}	$c_{o,X}$	$c_{m,X}$	$c_{p,X}$	$c_{o,R}$	$c_{m,R}$	$c_{p,R}$	R^2
fluoro	-47.43 ± 0.02	4.80 ± 0.02	0.63 ± 0.03	1.24 ± 0.04	2.66 ± 0.03	-0.22 ± 0.03	0.82 ± 0.05	1
chloro	-7.12 ± 0.03	2.10 ± 0.04	0.66 ± 0.04	0.50 ± 0.07	1.50 ± 0.05		0.71 ± 0.08	0.9999
bromo	5.30 ± 0.07	2.63 ± 0.09	0.80 ± 0.09	0.44 ± 0.14	0.84 ± 0.10		0.66 ± 0.16	0.9998

$$\Delta H_f^\circ \sim \Delta H_f^\circ(ref) + c_{C-X}n_{C-X} + c_{o,X}n_{o,X} + c_{m,X}n_{m,X} + c_{p,X}n_{p,X} + c_{o,R}n_{o,R} + c_{m,R}n_{m,R} + c_{p,R}n_{p,R} \tag{3.8}$$

It is clear from the linear regression that the main factor affecting the stability of the halogenated benzenes, besides the number of halogen substitutions (c_{C-X}), is the number of pairs of halogen substitutions *ortho* to one another ($c_{o,X}$). This effect is more pronounced for bromine substitution than it is for chlorine substitution, as one one would expect due to increased steric repulsion with the larger halogen, but the effect is even more pronounced for fluorine substitution. We ascribe this to the unfavorable electrostatic effect of having two very polarized bonds at adjacent substitution sites, and not to steric repulsion; the large *para* fluorine substitution effect ($c_{p,X}$) that is observed is consistent with this analysis. Interestingly, the $c_{o,X}$, $c_{m,X}$, and $c_{p,X}$ parameters for the (poly)fluorobenzenes are roughly proportional to their corresponding substituent chemical shifts in ^{19}F nuclear magnetic resonance spectroscopy [82].

For halogenated phenyl radicals, halogen substitution *ortho* to the free valence causes

an additional large increase in the energy ($c_{o,R}$), especially for fluorinated congeners. Presumably, this owes largely to the destabilization associated with an electron-withdrawing substituent adjacent to an electron-deficient site. The increase in energy, albeit a smaller one, associated with halogen substitution *para* to the free valence ($c_{p,R}$) and the trend of decreasing $c_{o,R}$ and $c_{p,R}$ for less polarized carbon-halogen bonds are also consistent with this analysis.

3.3.2 Bond Dissociation Enthalpies

The gas-phase BDEs associated with the dissociation of the carbon-hydrogen and carbon-halogen bonds of the (poly)halogenated benzenes are reported in Table 3.5. The BDEs are calculated as the enthalpy of reaction of the associated bond dissociation reaction, using the standard enthalpies of formation predicted in this work for each species (in other words, the absolute BDEs are not calculated directly with the DFT method). The enthalpies of formation for the hydrogen and halogen radicals are taken from the Argonne Thermochemical Network [67, 83].

Since breaking carbon-hydrogen bonds does not involve a change in the number of halogen substitutions or the positions of halogen substitutions with respect to one another, the trends in the predicted carbon-hydrogen BDEs can be understood exclusively in terms of the energetic costs of halogen substitution *ortho*, *meta*, and *para* to a free valence. Carbon-hydrogen bonds are stronger when adjacent to carbon-halogen bonds, as breaking a carbon-hydrogen bond adjacent to a carbon-halogen bond requires the

Table 3.5: Gas-phase C-H and C-X bond dissociation enthalpies (kcal mol^{-1}) for (X)-substituted benzene congeners

	carbon-hydrogen bonds				carbon-halogen bonds			
	locant	fluoro	chloro	bromo	locant	fluoro	chloro	bromo
benzene		(112.8)	(112.8)	(112.8)				
mono	2	115.4	114.5	114.0		127.2	97.1	82.3
	3	113.1	113.1	113.0				
	4	113.8	113.6	113.5				
1,2-di	3	115.6	114.4	113.6		124.9	96.4	80.8
	4	114.0	113.8	113.7				
1,3-di	2	118.3	116.2	115.1		126.8	96.4	81.5
	4	116.3	115.2	114.6				
	5	113.4	113.2	113.0				
1,4-di		115.9	114.8	114.2		126.9	97.0	82.2
1,2,3-tri	4	116.2	114.9	114.0	1	124.3	95.4	79.3
	5	114.1	113.9	113.7	2	122.8	95.7	79.0
1,2,4-tri	3	118.4	116.0	114.7	1	124.5	96.4	80.8
	5	116.5	115.4	114.7	2	124.6	95.9	80.3
	6	115.9	114.3	113.6	4	126.4	96.5	81.6
1,3,5-tri		119.2	116.8	115.7		126.4	95.8	80.9
1,2,3,4-tetra		116.7	115.1	114.1	1	124.1	95.6	79.3
					2	122.6	95.1	77.7
1,2,3,5-tetra		119.1	116.4	115.0	1	124.1	94.8	78.8
					2	122.4	95.9	79.3
					5	125.9	96.0	81.1
1,2,4,5-tetra		118.8	115.9	114.2		124.2	96.2	80.6
penta		119.2	116.2	114.3	1	123.5	95.2	78.8
					2	121.9	95.1	77.6
					3	122.1	94.3	76.2
hexa						121.5	94.2	75.6

formation of a radical with a carbon-halogen bond in the *ortho* position, which is high in energy (put differently, the electrophilic *ortho* halogen substituent disfavors a hydrogen atom leaving with an associated electron). Likewise, carbon-hydrogen bonds are also slightly stronger when *para* to carbon-halogen bonds, and are slightly weaker when *meta* to carbon-halogen bonds. These trends are subtle for brominated and chlorinated benzenes, for which the energetic cost of halogen substitution *ortho* and *para* a free valence is low (the reported gas-phase carbon-hydrogen BDEs for the brominated and chlorinated benzenes have ranges of 2.7 kcal mol^{-1} and 3.7 kcal mol^{-1}, respectively). For the fluorinated benzenes, however, carbon-hydrogen BDEs have a much more considerable range of 6.1 kcal mol^{-1}.

Unlike carbon-hydrogen bonds, carbon-halogen bonds are weaker when adjacent to other carbon-halogen bonds, as the removal of the unfavorable interaction between carbon-halogen bonds *ortho* to one another outweighs the energetic cost of forming a radical *ortho* to a halogen substitution. Interestingly, this trend is again stronger for fluorobenzenes than it is in chlorobenzenes, but it is also strong for the bromobenzenes due to the high steric interactions of adjacent bromine substitutions. For example, the weakest carbon-halogen bonds in 1,2,3-trifluorobenzene and 1,2,3-tribromobenzene are the inner ones, whereas the weakest carbon-chlorine bond in 1,2,3-trichlorobenzene is the outer one. This prediction partially explains the recent finding that the removal of the fluorine with locant 2 from 1,2,3,5-tetrafluorobenzene is preferred over the removal

of the fluorines with locants 1 and 3 in the presence of a heterogenous Rh/Al_2O_3 catalyst, while the opposite trend is observed for 1,2,3,5-tetrachlorobenzene [37]. Another interesting prediction is that the weakest carbon-halogen bonds in pentachlorobenzene and pentabromobenzene are those with locant 3, whereas the weakest carbon-fluorine bonds in pentafluorobenzene are those with locants 2 and 4. This can be understood in terms of the unfavorability of having fluorine substitutions *para* to each other; *para* substitution slightly weakens carbon-fluorine bonds, whereas it has little or no effect on carbon-chlorine and carbon-bromine bonds.

3.3.3 Gibbs Free Energies of Formation

The predicted gas-phase enthalpies of formation in Table 3.3 are used to predict the gas-phase Gibbs free energies of formation using DFT predicted entropies as in Eq. 3.9. For benzene and the monohalogenated benzenes, the Henry's law constants (K_H) have been critically reviewed by Mackay and Shiu [84], and these values, along with the necessary correction for the change in standard state, are used to calculate the aqueous Gibbs free energies as in Eq. 3.10. The aqueous Gibbs free energies of reaction for the remaining (poly)halogenated benzenes are predicted using the aqueous Gibbs free energies of reaction of the homodesmotic equation in Eq. B.1. For phenyl radical, the Gibbs free energy of solvation is calculated directly with SMD model chemistry, and the aqueous free energy of formation is predicted as in Eq. 3.11. The aqueous Gibbs free energies of the (poly)halogenated phenyl radicals are then predicted through the homodesmotic

reaction in Eq. 3.6. Both sets of predictions are reported in Table 3.6. The values are reported along with the uncertainty in the predictions which originates exclusively in the use of experimental enthalpy of formation and Henry's law constant data in the predictions. The direct prediction of entropies with DFT will inevitably introduce uncertainty which is not accounted for in these reported uncertainties, although this uncertainty should be expected to be modest [85, 86]. In the case of the phenyl radicals, the direct prediction of free energy of solvation of phenyl radical with the SMD model chemistry introduces additional uncertainty, although estimates for this uncertainty exist in the literature [56, 87].

$$\Delta_f G^\circ_{(g)} = \Delta_f H^\circ_{(g)} - TS^\circ_{(DFT)} \tag{3.9}$$

$$\Delta_f G^\circ_{(aq.)} = \Delta_f H^\circ_{(g)} - TS^\circ_{(DFT)} + RTln(K_{H(exp.)}) + RTln\Big(\frac{1M}{1atm}\Big) \tag{3.10}$$

$$\Delta_f G^\circ_{(aq.)} = \Delta_f H^\circ_{(g)} - TS^\circ_{(DFT)} + \Delta_{solv} G^\circ_{(DFT)} + RTln\Big(\frac{1M}{1atm}\Big) \tag{3.11}$$

Table 3.6: Predicted gas-phase (g) and aqueous (aq) Gibbs free energies of formation of (poly)halogenated benzenes and phenyl radicals (in kcal mol^{-1}).

	$\Delta_f G^\circ(F,g)^a$	$\Delta_f G^\circ(Cl,g)^a$	$\Delta_f G^\circ(Br,g)^a$	$\Delta_f G^\circ(F,aq)^b$	$\Delta_f G^\circ(Cl,aq)^b$	$\Delta_f G^\circ(Br,aq)^b$
benzene	(0.7 ± 0.1)	(0.7 ± 0.1)	(0.7 ± 0.1)	(1.7 ± 0.1)	(1.7 ± 0.1)	(1.7 ± 0.1)
mono	-49.2 ± 0.2	-9.9 ± 0.1	1.8 ± 0.3	-48.1 ± 0.2	-9.1 ± 0.2	2.3 ± 0.3
1,2-di	-93.1 ± 0.2	-16.9 ± 0.3	6.8 ± 0.6	-92.2 ± 0.5	-16.2 ± 0.3	6.9 ± 0.7
1,3-di	-97.3 ± 0.5	-18.5 ± 0.3	5.0 ± 0.6	-96.0 ± 0.5	-17.6 ± 0.3	5.3 ± 0.7
1,4-di	-96.3 ± 0.5	-18.1 ± 0.3	5.2 ± 0.6	-95.2 ± 0.5	-17.5 ± 0.3	5.2 ± 0.7
1,2,3-tri	-136.2 ± 0.3	-23.0 ± 0.5	13.0 ± 0.9	-135.2 ± 0.8	-22.1 ± 0.5	12.9 ± 1.0
1,2,4-tri	-140.3 ± 0.5	-25.2 ± 0.5	10.1 ± 0.9	-139.2 ± 0.8	-24.2 ± 0.5	10.5 ± 1.0
1,3,5-tri	-144.2 ± 0.7	-25.7 ± 0.5	9.5 ± 0.9	-142.1 ± 0.8	-24.3 ± 0.5	10.3 ± 1.0
1,2,3,4-tetra	-178.6 ± 0.3	-28.9 ± 0.6	19.4 ± 1.3	-177.5 ± 1.0	-27.6 ± 0.7	19.6 ± 1.3
1,2,3,5-tetra	-182.5 ± 0.5	-30.4 ± 0.6	17.2 ± 1.3	-181.5 ± 1.0	-28.7 ± 0.7	17.9 ± 1.3
1,2,4,5-tetra	-181.7 ± 0.5	-30.4 ± 0.6	16.9 ± 1.3	-180.5 ± 1.0	-28.9 ± 0.7	17.6 ± 1.3
penta	-219.8 ± 0.3	-34.1 ± 0.8	26.6 ± 1.6	-218.3 ± 1.3	-31.9 ± 0.9	27.4 ± 1.7
hexa	-255.6 ± 0.3	-36.2 ± 0.9	38.3 ± 1.9	-253.8 ± 1.5	-33.1 ± 1.1	39.5 ± 2.0
phenyl	(60.0 ± 0.1)	(60.0 ± 0.1)	(60.0 ± 0.1)	(60.8 ± 0.1)	(60.8 ± 0.1)	(60.8 ± 0.1)
2-mono	13.4 ± 0.3	51.8 ± 0.2	62.9 ± 0.3	14.5 ± 0.3	52.4 ± 0.2	63.2 ± 0.4
3-mono	11.0 ± 0.3	50.4 ± 0.2	61.9 ± 0.3	12.2 ± 0.3	51.1 ± 0.2	62.4 ± 0.4
4-mono	12.2 ± 0.3	51.3 ± 0.2	62.9 ± 0.3	13.1 ± 0.3	51.9 ± 0.2	63.2 ± 0.4
2,3-di	-30.3 ± 0.3	44.6 ± 0.4	67.5 ± 0.7	-29.2 ± 0.5	45.5 ± 0.4	67.6 ± 0.7
2,4-di	-33.9 ± 0.5	43.8 ± 0.4	66.6 ± 0.7	-32.4 ± 0.5	44.7 ± 0.4	66.9 ± 0.7
2,5-di	-33.7 ± 0.5	43.3 ± 0.4	66.1 ± 0.7	-32.3 ± 0.5	44.2 ± 0.4	66.5 ± 0.7
2,6-di	-31.5 ± 0.5	45.1 ± 0.4	67.5 ± 0.7	-29.7 ± 0.5	46.1 ± 0.4	67.7 ± 0.7
3,4-di	-31.9 ± 0.3	44.1 ± 0.4	67.7 ± 0.7	-30.9 ± 0.5	44.9 ± 0.4	68.0 ± 0.7
3,5-di	-36.4 ± 0.5	42.3 ± 0.4	65.5 ± 0.7	-34.7 ± 0.5	43.5 ± 0.4	66.4 ± 0.7
2,3,4-tri	-72.9 ± 0.3	38.9 ± 0.5	74.0 ± 1.0	-71.6 ± 0.8	40.1 ± 0.6	74.1 ± 1.0
2,3,5-tri	-76.9 ± 0.5	36.8 ± 0.5	71.2 ± 1.0	-75.1 ± 0.8	38.3 ± 0.6	71.9 ± 1.0
2,3,6-tri	-74.4 ± 0.5	38.2 ± 0.5	72.2 ± 1.0	-72.6 ± 0.8	39.6 ± 0.6	72.5 ± 1.0
2,4,5-tri	-76.3 ± 0.5	37.6 ± 0.5	72.4 ± 1.0	-74.7 ± 0.8	39.0 ± 0.6	73.0 ± 1.0
2,4,6-tri	-78.1 ± 0.8	37.9 ± 0.5	71.9 ± 1.0	-75.6 ± 0.8	39.6 ± 0.6	72.9 ± 1.0
3,4,5-tri	-74.6 ± 0.3	38.4 ± 0.5	74.2 ± 1.0	-73.3 ± 0.8	39.8 ± 0.6	74.7 ± 1.0
2,3,4,5-tetra	-114.7 ± 0.3	33.3 ± 0.7	80.6 ± 1.3	-113.0 ± 1.0	35.3 ± 0.7	81.3 ± 1.4
2,3,4,6-tetra	-116.4 ± 0.5	33.0 ± 0.7	79.1 ± 1.3	-114.1 ± 1.0	35.2 ± 0.7	80.1 ± 1.4
2,3,5,6-tetra	-115.8 ± 0.5	32.6 ± 0.7	78.1 ± 1.3	-113.6 ± 1.0	34.8 ± 0.9	79.1 ± 1.7
2,3,4,5,6-penta	-153.2 ± 0.4	29.5 ± 0.8	88.3 ± 1.6	-150.7 ± 1.3	32.5 ± 0.9	89.4 ± 1.7

[a] 1 atm standard state
[b] 1 M standard state

3.3.4 Free Energies of Reaction and Redox Potentials

Free energies of reaction for the hydrodehalogenation reaction in Eq. 3.12 are predicted through the summation of the relevant Gibbs free energies of formation. Standard state concentrations of 1M for all aqueous species (and therefore a pH of 0) and a standard pressure of 1 atm for dihydrogen gas are assumed. The gas-phase Gibbs free energy of formation for the proton has been previously calculated using electron convention Fermi-Dirac statistics [88,89], and a value for the free energy of solvation has been derived from experimental data specifically for use with this value [89, 90], both of which are used. For all anions, the experimental electron affinities [91–93] are subtracted from the experimental enthalpies of formation of the corresponding atoms [94], to which the thermal electron correction is added [88]. These anionic gas-phase enthalpies of formation are converted to Gibbs free energies of formation using the experimental standard entropies of the anions [94]. Gibbs free energies of solvation are derived from experimental conventional free energies of solvation [90, 95], and these values, as well as the correction for the change of standard state, are added to the gas-phase free energies of formation to calculate the aqueous free energies of formation for each anion. For all aromatic species, the predicted Gibbs free energies of formation reported in Table 3.6 are used.

$$C_6H_{6-n}X_{n(aq)} + H_{2(g)} \longrightarrow C_6H_{6-n+1}X_{n-1(aq)} + H^+_{(aq)} + X^-_{(aq)} \tag{3.12}$$

The two-electron reduction half-reactions in Eq. 3.13 are likewise considered. By

Table 3.7: Aqueous Gibbs free energies of hydrodehalogenation (in kcal mol^{-1}) and two-electron reduction potentials (in mV) for (poly)halogenated benzenes.

Reactant	Product	$\Delta_r G(F)^{a,c}$	$\Delta_r G(Cl)^{a,c}$	$\Delta_r G(Br)^{a,c}$	$E_0'(F)^{b,c}$	$E_0'(Cl)^{b,c}$	$E_0'(Br)^{b,c}$
mono	benzene	-14.0	-18.4	-20.8	499	596	648
1,2-di	mono	-19.6	-22.2	-24.9	620	677	736
1,3-di	mono	-15.8	-20.7	-23.3	540	645	702
1,4-di	mono	-16.6	-20.8	-23.2	556	648	700
1,2,3-tri	1,2-di	-20.7	-23.3	-26.3	645	702	766
	1,3-di	-24.4	-24.8	-27.9	726	734	800
1,2,4-tri	1,3-di	-20.5	-22.6	-25.4	641	687	747
	1,4-di	-19.7	-22.5	-25.5	624	685	749
	1,2-di	-16.8	-21.2	-23.8	560	655	713
1,3,5-tri	1,3-di	-17.5	-22.5	-25.2	576	685	743
1,2,3,4-tetra	1,2,3-tri	-21.5	-23.7	-27.0	662	711	781
	1,2,4-tri	-25.4	-25.9	-29.4	747	757	834
1,2,3,5-tetra	1,2,4-tri	-21.3	-24.7	-27.7	659	732	796
	1,3,5-tri	-24.3	-24.8	-27.9	724	734	801
	1,2,3-tri	-17.4	-22.6	-25.2	574	686	743
1,2,4,5-tetra	1,2,4-tri	-22.4	-24.6	-27.4	681	729	791
penta	1,2,3,4-tetra	-22.9	-24.9	-28.1	692	737	805
	1,2,3,5-tetra	-26.9	-26.1	-29.8	780	761	843
	1,2,4,5-tetra	-25.9	-26.2	-30.1	758	765	848
hexa	penta	-28.2	-28.0	-32.3	807	804	896

[a] Values calculated using Eq. 3.12.
[b] Values calculated using Eq. 3.14.
[c] At 1 atm standard state for gas-phase species, 1M concentration for aqueous species, and pH 0.

convention, the Gibbs free energy of formation of the gas-phase free electron at 298.15K is zero [88]. The potential of the reaction is calculated from the free energy using the Nernst equation and reported against the standard hydrogen electrode (SHE), as shown in Eq. 3.14 (where F is Faraday's constant, and n is the number of electrons in the half-reaction). A value of 4.281 V is used for the absolute potential of the SHE [89, 95]. The predicted free energies of hydrodehalogenation and two-electron reduction potentials are reported together in Table 3.7.

$$\mathrm{C_6H_{6-n}X_{n(aq)}} + \mathrm{H^+_{(aq)}} + 2\,\mathrm{e^-_{(g)}} \longrightarrow \mathrm{C_6H_{6-n+1}X_{n-1(aq)}} + \mathrm{X^-_{(aq)}} \tag{3.13}$$

$$E^\circ = -\frac{\Delta_r G^\circ}{nF} - SHE \tag{3.14}$$

Trends in the predicted free energies of reaction can be largely explained by the release of the energetic costs associated with pairs of halogen substitutions *ortho*, *meta*, and *para* to each other. They therefore vary much more widely than do the predicted BDEs as, for example, the extra energy released when a halogen substitution *ortho* to another halogen substitution is removed is partially compensated by the energetic cost of forming a radical *ortho* to a halogen substitution. As the *ortho* effect is the largest, it is no surprise that the free energies for defluorination have the largest range, 14.2 kcal mol^{-1}, but that the range of the free energies of debromination, 11.4 kcal mol^{-1}, is larger then that of the free energies of dechlorination, 9.6 kcal mol^{-1}. The *para* effect for fluorine is more subtle, but noticeable. For example, the dehalogenation of 1,4-difluorobenzene is almost 1 kcal mol^{-1} more exothermic than the dehalogenation of 1,3-difluorobenzene, whereas the free energies of dehalogenation of 1,3-dichlorobenzene and 1,4-dichlorobenzene, as well as those of 1,3-dibromobenzene and 1,4-dibromobenzene, do not vary by a large amount. The two-electron reduction potentials naturally follow the same trends as the free energies of hydrodehalogenation. It should be noted that the two-electron reduction potential values for the (poly)chlorinated benzenes are considerably higher than the previous predictions that exist in the literature [47].

3.3.5 Aqueous Bond Dissociation Free Energies

The aqueous Gibbs free energies of formation are also used to predict the aqueous bond dissociation free energies (BDFEs), analogous to the gas-phase BDE predictions above.

These predictions are reported in Table 3.8. Unfortunately, no reliable experimental values for the free energies of solvation of atomic hydrogen and the atomic halogens exist in the literature, so recourse to the direct prediction of these quantities through the SMD formalism is necessary for these species. While the SMD formalism has been extensively parameterized and validated for the free energies of aqueous solvation of neutral organics [56, 87] and can therefore be expected to give reasonable errors for the aromatics considered, its performance for small inorganic radicals is not documented. Thus, the direct prediction of the solvation free energies for these species with the implicit SMD formalism could introduce some error in the predicted aqueous BDFEs. The aqueous BDFEs are generally found to follow the same trends as the gas-phase BDEs.

Table 3.8: Aqueous C-H and C-X bond dissociation free energies (in kcal mol^{-1}) for (X)-substituted benzene congeners

	carbon-hydrogen bonds				carbon-halogen bonds			
	locant	fluoro	chloro	bromo	locant	fluoro	chloro	bromo
benzene		(104.4)	(104.4)	(104.4)				
mono	2	107.8	106.8	106.2		117.0	87.6	73.2
	3	105.5	105.5	105.4				
	4	106.5	106.3	106.2				
1,2-di	3	108.3	106.9	106.0		116.3	86.4	71.7
	4	106.6	106.4	106.3				
1,3-di	2	115.5	109.0	107.7		116.3	86.4	71.7
	4	108.9	107.6	106.8				
	5	106.5	106.4	106.3				
1,4-di		108.2	107.0	106.5		116.5	87.1	72.7
1,2,3-tri	4	109.0	107.5	106.5	1	114.3	85.2	69.4
	5	107.2	107.2	107.1	2	113.7	85.9	69.5
1,2,4-tri	3	111.9	109.1	107.3	1	115.0	86.6	71.1
	5	109.7	108.5	107.8	2	115.1	86.1	70.7
	6	109.3	107.8	106.7	4	116.4	86.8	72.2
1,3,5-tri		111.8	109.2	107.9		115.6	85.5	70.8
1,2,3,4-tetra		109.8	108.1	106.9	1	114.1	85.4	69.2
					2	113.1	84.9	67.5
1,2,3,5-tetra		112.7	109.2	107.5	1	117.1	86.0	69.3
					2	114.1	86.0	69.7
1,2,4,5-tetra		112.2	108.9	106.8		113.9	85.6	70.1
penta		112.9	109.6	107.3	1	113.5	84.8	68.5
					2	112.4	84.8	67.3
					3	112.9	84.3	66.4
hexa						111.3	83.2	64.7

3.4 Environmental Significance

One consistent theme across the range of physical properties studied is that chlorinated and brominated aromatics have more properties in common with each other than they have with fluorinated aromatics. It is well known that carbon-fluorine bonds are stronger than other carbon-halogen bonds and that defluorination is less exothermic than other dehalogenation reactions, making fluorinated aromatics more resistant to both biotic and abiotic degradation. However, the smaller size of the fluorine atom and the increased polarity of the carbon-fluorine bond also result in decreased steric effects and increased electrostatic effects. We predict that the increased electrostatic effects, in particular, are responsible for a significantly greater variation in bond strengths and free energies of hydrodehalogenation for fluorinated aromatics. Presumably, the greater variation in these properties should result in greater selectivity in the degradation of these compounds. We additionally highlight some particular cases where selectivity in fluorinated and chlorinated aromatics should be expected to follow opposing trends.

Chapter 4

Nucleophilic Aromatic Substitution[1]

4.1 Introduction

Chlorinated and brominated aromatics are broad classes of environmental contaminants, examples of which can be found across the globe due to decades of their use in open and dissipative applications [2,3,7–9,12]. As a matter of course, the natural biotic and abiotic degradation of these compounds, as well as engineered solutions towards their remediation have been the subject of much research. In recent years, fluorinated pollutants, including some aromatics, have also been the subject of increasing attention [1,4–6], which

[1] **This chapter has been submitted to *Environmental Science & Technology* for consideration for publication as "Dehalogenation of Aromatics by Nucleophilic Aromatic Substitution". Profs. Kristopher McNeill and Christopher J. Cramer are co-authors of the chapter.**

raises the question of how the unique chemical properties of fluorinated aromatics affect remediation strategies. For example, carbon-fluorine bonds are much stronger than carbon-chlorine and carbon-bromine bonds, and hydrodehalogenation is less exothermic for fluorinated aromatics than it is for chlorinated and brominated aromatics [96]. Additionally, the greater polarity of the carbon-fluorine bond is predicted to result in increased selectivity in dehalogenation processes involving fluorinated aromatics [96].

One class of mechanisms through which the hydrodehalogenation of aromatics can occur is hydride transfer, where the transfer of a hydride to an aromatic substrate from a structure where it is weakly bound drives the heterolytic cleavage of a carbon-halogen bond in the aromatic substrate. For example, hydrodehalogenation reactions involving a large variety of metal and metalloid hydrides and aromatic (as well as aliphatic and allylic) substrates have been demonstrated [33, 34, 97–99]. Hydride transfer from metal nanoparticles used in groundwater remediation has also been suggested to be of importance for the ability of those systems to effect hydrodehalogenation [100]. There are several mechanisms through which hydrodehalogenation by metal and metalloid hydrides is proposed to take place; one mechanism that is invoked for aromatic substrates is nucleophilic aromatic substitution [33, 101, 102].

One interesting aspect about nucleophilic aromatic substitution is the observation that substitution at fluorinated sites is preferred over substitution at chlorinated and

brominated sites. This is in contrast to nucleophilic *aliphatic* substitution, where chlorinated and brominated sites are preferred. The observation is also remarkable considering the strength of the carbon-fluorine bond in comparison to carbon-chlorine and carbon-bromine bonds. This phenomenon is well known and has been exploited in chemical synthesis, for example, for the selective functionalization of perfluorinated aromatics [102–104]. A second interesting aspect of nucleophilic aromatic substitution is its biological importance. Both glutathione *S*-transferases [105] and 4-chlorobenzoyl-CoA dehalogenase [106, 107] are known to catalyze hydrodehalogenation reactions through nucleophilic aromatic substitution reactions, although with non-hydridic nucleophiles. Interestingly, fluorinated substrates are favored by the glutathione pathway [108], but not by the 4-chlorobenzoyl-CoA dehalogenase pathway [109].

Previous theoretical studies have made significant contributions to our understanding of nucleophilic aromatic substitution, especially the periodic trends in reactivity that are observed and the factors that can give rise to either a concerted or stepwise mechanism [110–112]. One aspect that has eluded comprehensive study is the extent to which the substitution patterns of the aromatic substrates themselves influence selectivity in nucleophilic aromatic substitution reactions, especially in the context of dehalogenation. Additionally, previous theoretical studies of nucleophilic aromatic substitution have focussed on gas phase reactivity. As both microbial degradation and abiotic remediation technologies such as pump-and-treat systems [113] and permeable reactive barrier systems [114] employ the aqueous phase, the estimation of the effect of solvation

on reactivity is of particular importance to our understanding of these pathways.

The task of explaining the entire range of reactivity possible for a given process is a daunting one. Previous contributions to the nucleophilic aromatic substitution literature have approached this problem by exclusively studying identity reactions [111, 112] under the assumption that the results can be generalized to non-identity substitution reactions in the case that information about the exothermicity of those reactions is available. Here, as we are specifically interested in aqueous dehalogenation, we choose an alternative limiting case, that of hydride, a strong base and good nucleophile with no adjacent steric bulk. The choice of hydride as a nucleophile also has the advantage that it can stand as a proxy for the various metal and metalloid hydrides which are frequently used in dehalogenation catalysis (although it should be noted that nucleophilic aromatic substitution is not the only mechanism available to this class of catalysts). We additionally perform calculations on the nucleophilic aromatic substitution reactions of a smaller set of substrates with hydroxide and hydrosulfide anions in order to test the behavior of these other nucleophiles, which are also of environmental relevance.

4.2 Computational Methods

The hybrid *meta*-generalized gradient level of density functional theory is used for all calculations, specifically the M06-2X functional [49], which has been extensively benchmarked and was chosen owing to its high accuracy for organic compounds [50–52]. The effect of solvation is estimated through use of the SMD [56] implicit solvation model for

all calculations. The standard 6-311+G(3df,2p) basis set and an integration grid of 99 radial shells and 590 angular points per shell are used, and the geometry of each structure is optimized until a maximum force of $2.0 \cdot 10^{-6}$ a.u., a root mean square (RMS) force of $1.0 \cdot 10^{-6}$ a.u., a maximum internal coordinate displacement of $6.0 \cdot 10^{-6}$ a.u., and a RMS internal force displacement of $4.0 \cdot 10^{-6}$ a.u. are reached. All optimized geometries and transition states are confirmed to be stationary points on the model chemistry potential energy surface with the correct number of negative eigenvalues in the local Hessian matrix by analytical calculation of the vibrational frequencies following the usual quantum-mechanical harmonic-oscillator approximation. These harmonic frequencies are scaled by a factor of 0.970, a parameter which has been empirically fit to M06-2X calculations in order to reproduce experimental zero-point vibrational energies [54], and used in the calculation of zero-point vibrational energies and vibrational partition functions. Prior to scaling, calculated vibrational frequencies less than 50 cm^{-1} are set at 50 cm^{-1} in order to eliminate the spurious large fluctuations in predicted entropies associated with finite integration grids leading to poorly converged low-frequency values, as well as to account for the breakdown of the quantum mechanical harmonic oscillator approximation for such normal modes in any case. In cases where the number of imaginary frequencies in a high-symmetry geometry is grid sensitive (with imaginary frequencies becoming real with increasing grid size), the spurious imaginary frequencies are also set to 50 cm^{-1}. All calculations are performed with the Gaussian 09 electronic structure suite, Revision C.01 [62]. All visualizations of geometries and molecular

orbitals are generated using Avogadro version 1.1.0 [115].

4.3 Results and Discussion

4.3.1 Nucleophilic Attack of Hydride

Transition states are optimized for the nucleophilic attack of hydride on benzene and on each symmetry unique carbon site of the 36 (poly)fluoro-, (poly)chloro-, and (poly)bromobenzenes. In the case of unsubstituted sites, the transition states are found to lead towards anionic σ-complexes without exception. An intrinsic reaction coordinate (IRC) calculation conducted for the case of benzene confirms this reaction path. Key bond lengths from the optimized structures of the transition state and the stable σ-complex for the reaction of hydride with benzene are reported in Fig. 4.1.

Figure 4.1: Reaction scheme for the nucleophilic addition of hydride onto benzene, along with key bond lengths (in Å) for the structures of the transition state (TS) and the anionic σ-complex intermediate (int).

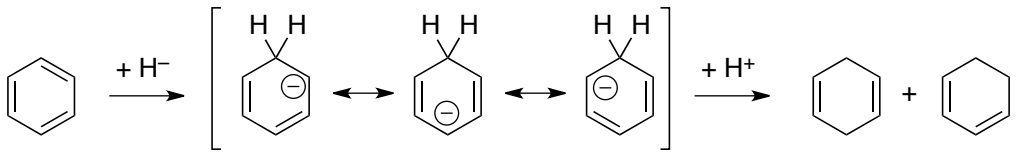

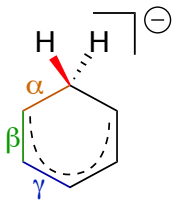

bond	TS	int
$\mathbf{r}_{C-H}$	1.701	1.115
$\mathbf{r}_{C-H}$	1.080	1.095
$\mathbf{r}_{C-C,\alpha}$	1.430	1.512
$\mathbf{r}_{C-C,\beta}$	1.377	1.364
$\mathbf{r}_{C-C,\gamma}$	1.402	1.420

The transition states at substituted sites, however, are found to lead to the concerted dissociation of the halogen as an anion in every case. An IRC calculation confirms this reaction path for the case of fluorobenzene. Key bond lengths for the optimized structures of the transition states for this reaction and the analogous ones for chlorobenzene and bromobenzene are reported in Fig. 4.2, alongside potential energy surfaces for each of the three reactions.

The activation free energies for all of the optimized transition states, as well as the respective free energies of reaction relative to an infinite separation of nucleophile and substrate are reported in Table 4.1. Each reported transition state in Table 4.1 is classified as being associated either with a concerted substitution reaction (in the case of nucleophilic attacks at substituted sites, which are indicated with an "X") or an addition reaction (in the case of nucleophilic attacks at unsubstituted sites, which are indicated with an "H").

It is notable that many of the addition reactions are predicted to be exothermic. While the reverse reactions are hypothetically accessible at room temperature in many cases, one might assume, as we do in Fig. 4.1, that protonation of the intermediate is more rapid under most environmental conditions. To test this assumption, various possible unimolecular reactions of the anionic intermediates are considered. For example, the transition states for 1,2-, 1,3-, and 1,4- hydride transfers in the anionic intermediate formed by benzene and hydride (where all three correspond to identity reactions) are predicted to have activation free energies of 66.4, 67.2, and 34.1 kcal mol^{-1}, respectively.

Table 4.1: Activation free energies and free energies of reaction (in kcal mol^{-1}) for the hypothetical nucleophilic addition(H)/substitution(X) reactions of hydride relative to an infinite separation of reactants in solution.

	Site	Type	$\Delta^{\ddagger}G$			$\Delta_{rxn}G$(addition)			$\Delta_{rxn}G$(substitution)		
			F	Cl	Br	F	Cl	Br	F	Cl	Br
benzene		H	(27.2)	(27.2)	(27.2)	(7.5)	(7.5)	(7.5)			
mono	1	X	22.5	25.6	27.1				-52.7	-70.5	-69.1
	2	H	25.9	22.9	23.3	7.4	3.4	3.4			
	3	H	25.4	25.0	24.9	3.7	2.6	2.9			
	4	H	29.4	26.5	26.3	10.7	5.1	5.1			
1,2-di	1	X	18.2	20.8	22.8				-58.3	-74.2	-73.2
	3	H	23.5	20.3	20.6	2.9	-2.1	-2.1			
	4	H	26.8	23.8	25.0	5.7	-0.1	0.0			
1,3-di	1	X	20.4	23.0	24.0				-54.6	-72.7	-71.6
	2	H	23.6	17.9	18.0	4.8	-3.0	-3.2			
	4	H	27.3	21.4	21.1	12.5	0.1	-0.4			
	5	H	23.0	22.0	21.6	0.4	-3.6	-3.4			
1,4-di	1	X	22.8	23.8	25.1				-55.4	-72.9	-71.5
	2	H	22.5	19.6	19.8	2.8	-3.4	-2.9			
1,2,3-tri	1	X	16.0	18.8	20.6				-59.4	-75.4	-74.5
	2	X	14.1	16.5	19.2				-63.2	-76.8	-76.1
	4	H	24.5	19.0	18.8	4.1	-4.9	-5.2			
	5	H	24.1	20.9	20.6	-0.1	-5.7	-6.0			
1,2,4-tri	1	X	19.0	19.9	21.5				-59.3	-74.7	-73.7
	2	X	16.4	18.9	20.6				-58.5	-74.6	-73.8
	3	H	21.4	15.9	15.9	0.5	-8.3	-8.4			
	4	X	21.3	22.0	23.1				-55.5	-73.2	-72.1
	5	H	24.6	19.1	18.9	4.0	-5.0	-5.4			
	6	H	21.1	17.8	17.7	-3.0	-8.1	-8.3			
1,3,5-tri	1	X	17.7	20.0	20.6				-56.3	-74.6	-73.5
	2	H	24.5	15.7	15.6	9.0	-6.6	-7.3			
1,2,3,4-tetra	1	X	16.6	17.5	19.4				-60.2	-75.8	-75.3
	2	X	12.4	14.5	16.8				-64.1	-77.9	-77.7
	5	H	21.7	16.2	16.4	-5.7	-10.8	-12.2			
1,2,3,5-tetra	1	X	14.5	16.2	17.9				-60.1	-76.8	-75.9
	2	X	15.0	15.1	17.2				-63.1	-76.9	-76.2
	4	H	23.0	14.1	14.0	0.9	-11.0	-20.1			
	5	X	19.4	19.8	20.5				-56.2	-74.6	-73.5
1,2,4,5-tetra	1	X	16.1	16.8	18.3				-61.1	-76.6	-75.7
	3	H	18.3	12.6	12.8	-6.0	-14.4	-22.6			
penta	1	X	14.2	15.2	16.9				-61.6	-77.0	-76.3
	2	X	12.4	13.3	15.6				-65.7	-78.1	-78.1
	3	X	10.2	12.7	15.3				-64.6	-78.2	-78.3
	6	H	19.4	11.8	12.2	-10.5	-17.0	-28.3			
hexa		X	9.3	10.9	13.0				-66.9	-80.1	-80.5

Figure 4.2: Reaction scheme for the nucleophilic substitution of hydride onto fluorobenzene (F), chlorobenzene (Cl), and bromobenzene (Br), along with key bond lengths (in Å) for the structures of the transition states.

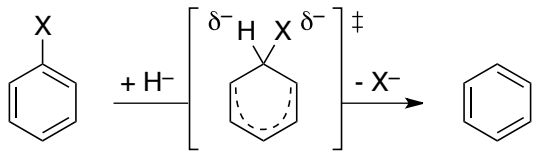

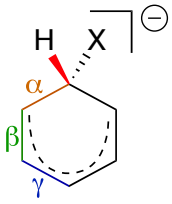

bond	F	Cl	Br
$\mathbf{r}_{C-H}$	1.765	1.764	1.777
$\mathbf{r}_{C-X}$	1.380	1.786	1.946
$\mathbf{r}_{C-C,\alpha}$	1.410	1.415	1.416
$\mathbf{r}_{C-C,\beta}$	1.381	1.380	1.379
$\mathbf{r}_{C-C,\gamma}$	1.396	1.397	1.398

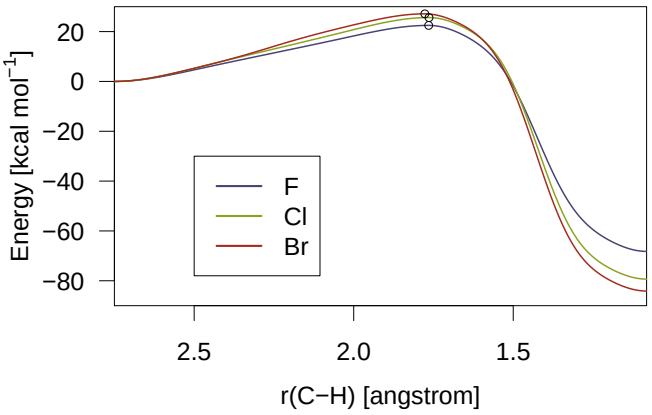

The electrocyclic ring closure of the same intermediate leading to the bicyclo[3.1.0]hex-1-enyl anion is predicted to have an activation free energy of 22.1 kcal mol^{-1}, which is only slightly higher than the activation free energy of the reverse reaction to form

benzene and hydride (19.7 kcal mol^{-1}), but still unlikely to occur under relevant conditions. Additionally, we studied the heterolytic dissociation of carbon-halogen bonds in several anionic intermediates and found no cases where such reactions competed with the reverse reaction. While the fate of these anionic intermediates is ultimately beyond the scope of this contribution, it is plausible that protonation could occur at sites *ortho* to the hydride attack, where there are significant negative charges, which would allow for hydrodehalogenation by way of an E2 elimination. In any case, our analysis here is limited to relative energetics of the initial substitution and addition reactions, both of which are assumed to be, in effect, irreversible.

Concerted substitution mechanisms are found to have lower activation energies than addition mechanisms for all (poly)fluorobenzene congeners except 1,4-difluorobenzene. In cases where multiple adjacent fluorinated sites are available, the innermost site has the lowest activation energy in all cases except that of 1,2,3,5-tetrafluorobenzene. In contrast, addition mechanisms are predicted to have lower activation free energies than substitution mechanisms for all (poly)chloro- and (poly)bromo- benzenes except 1,2,3-trichlorobenzene and 1,2,3,4-tetrachlorobenzene. Where multiple unsubstituted sites are available for (poly)chloro- and (poly)bromo- benzenes, sites adjacent to the maximum number of halogenated sites are found to be the lowest in all cases. A diagram depicting the sites with the lowest activation energies of hydride attack for each set of congeners is found in Figure 4.3.

The activation free energies for substitution reactions are predicted to be lower for

Figure 4.3: (Poly)halogenated benzene congeners with the preferred site of nucleophilic attack for the fluorinated, chlorinated, and brominated cases indicated (Color key: F = blue, Cl = light green, Br = dark red; Grayscale key: F = medium gray, Cl = light gray, Br = black).

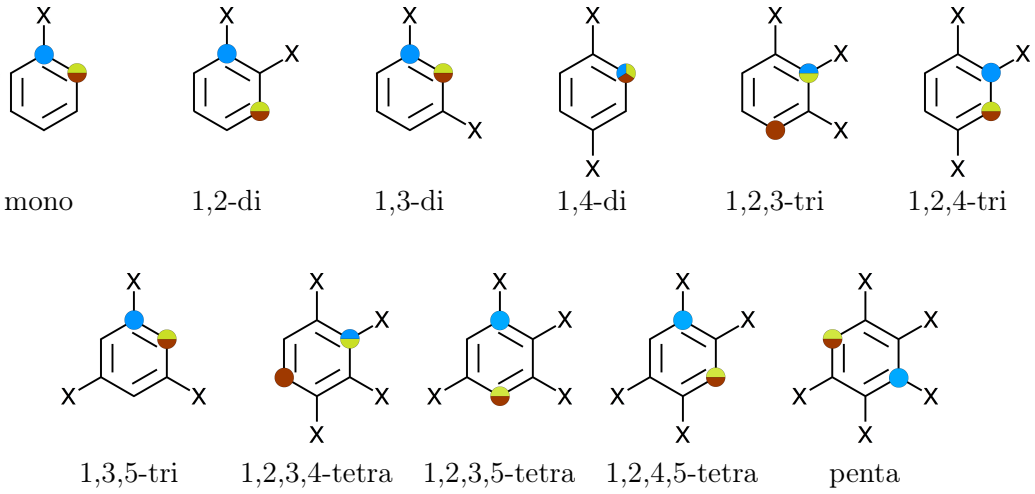

the fluorinated benzenes than the chlorinated and brominated benzenes, even though the exothermicities of the corresponding reactions follow the opposite trend (which is not surprising considering the previously mentioned experimental studies). Presumably, this discrepancy is explained by the structure of the transition states: carbon atoms that are bonded to more electronegative halogens would be expected to have a more positive local charge, and therefore function as better sites for nucleophilic attack. The prediction that the difference in the activation free energies of fluorobenzene and chlorobenzene is significantly larger than the difference between those for chlorobenzene and bromobenzene is consistent with this explanation, as the difference in electronegativity between

fluorine and chlorine is large compared to the difference between chlorine and bromine.

Another expected result is that the activation free energies for substitution reactions on structures with more carbon-halogen bonds are predicted to be significantly lower in energy. It is known experimentally, for example, that the reaction of hexafluorobenzene with sodium methoxide is 8 orders of magnitude faster than the corresponding reaction with fluorobenzene [116,117]. Our prediction with hydride as a nucleophile is a difference in activation free energies of 13.2 kcal mol^{-1}, which corresponds to 9 orders of magnitude in reaction rates.

Activation free energies for substituted reactions are especially lowered by substitution *ortho* to the attack site. This can be partially explained by the energetic cost of two carbon-halogen bonds in *ortho* position to each other. This energetic cost has been shown to be caused, in the case of fluorine, by two strong dipoles in nearly parallel position, and in the case of chlorine and bromine, largely by steric effects [96]. The magnitudes of the energetic costs are approximated to be 4.8, 2.1, and 2.6 kcal mol^{-1} for (poly)fluoro-, (poly)chloro-, and (poly)bromo- benzenes, respectively. The carbon-halogen bonds at the site of nucleophilic attack in the transition state structures all exhibit a slight deviation from planarity, so it could be expected that *ortho* interaction would be weakened, and therefore that the transition states would be correspondingly stabilized. From this analysis alone, one would expect a much greater stabilization of the 1,2-difluorobenzene transition state compared to the 1,2-dichlorobenzene and 1,2-dibromobenzene transition states; however, all three transition states are predicted to

be approximately 5 kcal mol^{-1} lower in energy than those for fluorobenzene, chlorobenzene, and bromobenzene, respectively. The electrostatics of the hydride attack must therefore also be considered. To some extent, carbon-halogen bonds should not only make the electrostatic potential above the α-carbon site more positive, but should also make an electropositive contribution to the electrostatic potential above adjacent sites and above the ring as a whole. It has been observed by Salabov et al. [118] that this effect is actually much more significant for carbon-chlorine and carbon-bromine bonds in aromatic systems than it is for carbon-fluorine bonds. Thus, it could be understood that the approximately proportional stabilization of transition states for substitution *ortho* to carbon-halogen bonds is coincidental, and due to a combination of unequal contributions from these two effects.

This analysis is confirmed by the transition states for hydride addition at unsubstituted sites. The activation free energies for the transition states are lower for structures with an increased number of carbon-halogen bonds, especially *ortho* to the site of nucleophilic attack, but only in the case of the (poly)chloro- and (poly)bromo- benzenes is this trend strong enough to make the activation free energies lower than those for the corresponding addition reactions.

Generally, the formation of the σ-anionic intermediates ($\Delta_{rxn}G$(addition) in Table 4.1) is predicted to be more exothermic with increasing halogen substitution, presumably because halogen substitution of the aromatic ring helps stabilize the extra electron. However, there is also a clear energetic cost associated with halogen substitution *ortho*,

and especially *para*, to the sp^3 carbon in the σ-anionic intermediates, and this energetic cost is particularly pronounced in the case of the fluorinated benzenes. This has been explained in terms of the highest occupied molecular orbital (HOMO) of these anions, which puts a significant amount of electron density in the conjugated π system on the carbon atoms *ortho*, and especially *para*, to the sp^3 carbon (see Figure 4.4) [119]. This results in a significant amount of exchange repulsion between the doubly occupied p-orbitals of the halogen substituent and the HOMO orbital, which results in an increase in energy. Carbon-fluorine bonds have much greater π overlap than carbon-chlorine and carbon-bromine bonds by nature of their shorter bond lengths and the similar size of carbon and fluorine p-orbitals, so a greater energetic perturbation for the fluorinated aromatics should be expected.

Figure 4.4: HOMO of anionic σ-complex formed from hydride and benzene (isosurface value = 0.075).

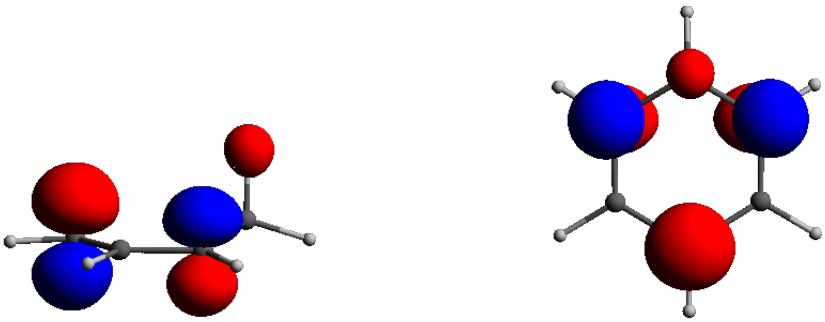

The trends in the stabilities of the σ-anionic complexes have an observable correlation with the trends in their corresponding activation free energies for the

(poly)fluorobenzenes. In the case of fluorobenzene, for example, hydride addition *meta* to the carbon-fluorine bond is favored over addition *ortho*, and especially *para*, to the carbon-fluorine bond, although no addition reaction is favored over the substitution reaction that is also available. In the case of the (poly)chloro- and (poly)bromobenzenes, where the energetic perturbation is smaller, there is no observable correlation, presumably owing to the greater influence of the electrostatic stabilization of the hydride attack on the activation free energies. Thus, hydride attack *ortho* to the carbon-halogen bond is favored for chlorobenzene and bromobenzene. The exchange repulsion effect has a further influence on substitution reactions for the (poly)fluorobenzenes. In the case of 1,4-difluorobenzene, for example, the energetic cost of hydride attack *para* to a carbon-fluorine bond is large enough to make the addition mechanism favored over the substitution mechanism. No such effect is observed in the substitution reactions of the (poly)chloro- and (poly)bromobenzenes.

4.3.2 Additional Nucleophiles

For a limited set of substrates, transition states are also optimized for nucleophilic attacks by hydroxide and hydrosulfide anions. The activation free energies of these transition states are reported in Table 4.2, with the activation free energies of the corresponding transition states with hydride as the nucleophile reproduced for convenience. For the reactions of hydride, hydroxide, and hydrosulfide with fluorobenzene, the key geometrical parameters of each transition state, as well as potential energy surfaces constructed

from constrained geometry optimizations are reported in Figure 4.5. For substitution reactions, the trends in activation free energies are found to be qualitatively consistent with the trends predicted with hydride as the nucleophile, although the activation free energies are higher for hydroxide and those for hydrosulfide are even higher than those for hydroxide. This follows the trend that stronger bases are stronger nucleophiles, although it is not in agreement with the observation that thiols, for example glutathione *S*-transferases, are effective nucleophiles for halogenated aromatics. It is plausible that for hydrosulfide and other thiols, an alternate mechanism involving electron transfer [120, 121] exists which could explain this discrepancy.

For addition reactions involving hydroxyl, however, there is an even greater difference in the activation free energies between hydride and hydroxide, to the point where substitution with hydroxide is preferred relative to addition with hydroxide for chlorobenzene and bromobenzene (which is the opposite of what is predicted for hydride). In the case of the nucleophilic attack of hydrosulfide on unsubstituted carbons, there is no stable anionic intermediate, and therefore no addition reactions occur. Instead, there is a concerted substitution transition state which is very high in energy (for example, a 74.5 kcal/mol free energy of reaction is predicted in the case of benzene). An IRC calculation for the attack of hydrosulfide on benzene supports this reaction path.

Figure 4.5: Reaction scheme for the nucleophilic substitution of hydride (H), hydroxide (OH), and hydrosulfide (SH) onto fluorobenzene, along with key bond lengths (in Å) for the structures of the transition states.

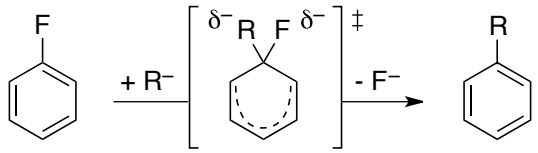

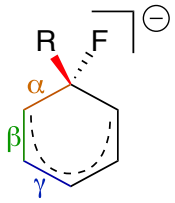

bond	H	OH	SH
$\mathbf{r}_{C-R}$	1.765	1.881	2.050
$\mathbf{r}_{C-F}$	1.380	1.376	1.441
$\mathbf{r}_{C-C,\alpha}$	1.410	1.415	1.439
$\mathbf{r}_{C-C,\beta}$	1.381	1.382	1.378
$\mathbf{r}_{C-C,\gamma}$	1.396	1.396	1.399

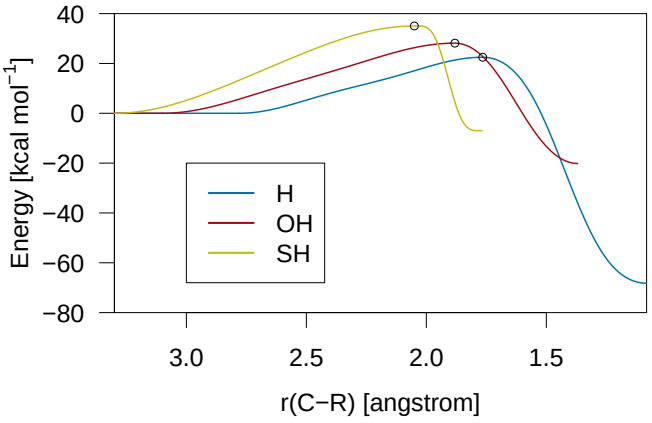

4.4 Environmental Significance

For the limiting case of hydride as a nucleophile, we demonstrate that concerted nucleophilic substitution reactions are generally preferred in defluorination, whereas stepwise reactions initiated by nucleophilic addition *ortho* to carbon-halogen bonds are generally

Table 4.2: Activation free energies (in kcal mol^{-1}) of the transition states for selected nucleophilic addition(H)/substitution(X) reactions with hydride (H), hydroxide (OH), and hydrosulfide (SH) anions as nucleophiles.

	Site	Type	$\Delta^{\ddagger}G$(H)			$\Delta^{\ddagger}G$(OH)			$\Delta^{\ddagger}G$(SH)		
			F	Cl	Br	F	Cl	Br	F	Cl	Br
benzene		H	(27.2)	(27.2)	(27.2)	(37.5)	(37.5)	(37.5)			
mono	1	X	22.5	25.6	27.1	28.1	34.4	35.7	35.0	37.9	37.8
	2	H	25.9	22.9	23.3	37.9	34.9	35.3			
	3	H	25.4	25.0	24.9	35.1	35.0	35.1			
	4	H	29.4	26.5	26.3	40.7	36.8	36.5			
1,2-di	1	X	18.2	20.8	22.8	27.1	31.6	34.2	31.6	34.2	34.9
1,3-di	1	X	20.4	23.0	24.0	26.8	31.5	32.7	31.8	34.3	34.1
1,4-di	1	X	22.8	23.8	25.1	28.6	32.5	33.6	36.3	35.7	35.2
hexa		X	9.3	10.9	13.0	19.2	22.1	25.3	20.6	21.1	22.7

preferred in dechlorination and debromination. In addition, a data set is generated which should hopefully facilitate mechanistic comparisons in the field of dehalogenation. For example, the carbon-fluorine bond in pentafluorobenzene with locant 3 has been predicted to be the most susceptible to nucleophilic attack by the calculations described here (and incidentally, several reports in the synthesis literature [122–124]), while the carbon-fluorine bond with locants 2 and 4 has elsewhere been predicted to be the weakest with respect to homolytic bond dissociation by essentially the same computational methodology [96]. The predictions also help explain the observation that 1,3,5-trifluorobenzene and 1,2,4-trifluorobenzene are observed as intermediates in the aqueous hydrodefluorination of 1,2,3,5-tetrafluorobenzene with hydrogen gas over a rhodium surface, while 1,2,4-trichlorobenzene and 1,2,3-trichlorobenzene are observed for the hydrodechlorination of 1,2,3,5-tetrachlorobenzene under the same conditions [37]: from the predictions here, we would expect the concerted substitution reactions at the carbon-fluorine bonds with locants 1 and 2 to dominate for 1,2,3,5-tetrafluorobenzene, but we would expect the addition reaction at locant 4 to dominate for 1,2,3,5-tetrachlorobenzene, possibly

followed by the addition of a proton on an adjacent carbon and subsequent elimination. Finally, the results highlight the potential importance of nucleophilic aromatic substitution as a mechanism not only for the degradation of fluorinated aromatics, which are otherwise more resistant to hydrodehalogenation than chlorinated and brominated aromatics, but also for highly substituted halogenated aromatics in general.

Chapter 5

Binding to Rhodium Surfaces

5.1 Introduction

Halogenated aromatics are common groundwater pollutants, and one strategy used for the remediation of sites contaminated with halogenated aromatics is the use of pump-and-treat systems [113]. Recently, fluorinated aromatic compounds have found increasing use in agriculture, medicine, and in the chemical industry [1,6,125], which has led to increased attention to their dehalogenation pathways both in the natural environment and in remediation systems [36,37,126–128].

Unfortunately, Pd-based pump-and-treat systems have been shown to have a low affinity for fluorinated aromatics [129–131], although a Rh-based catalytic system reported by Baumgartner et al. has recently been demonstrated to effectively catalyze the

complete dehalogenation and dehydrogenation of both fluorinated and chlorinated aromatic substrates under mild conditions [36, 37]. One interesting observation about this particular system is that, whereas the observed rates of dehalogenation for the chlorinated aromatics depend largely on the number of halogen substitutions (with increasing substitution resulting in slower dehalogenation), the rates for the fluorinated aromatics depend largely on the number of halogen substitutions *adjacent* to each other (with higher numbers of substitutions resulting in faster dehalogenation) [37].

One plausible mechanism through which dehalogenation might occur in the system described by Baumgartner et al. is a nucleophilic aromatic substitution mechanism, where a hydride from the Rh surface acts as a nucleophile. A recent density functional theoretical study of the dehalogenation of aromatics by nucleophilic aromatic substitution by a hydride nucleophile in aqueous solution by Sadowsky et al. [132] has also predicted the trend observed by Baumgartner et al. that fluorinated aromatics with higher numbers of adjacent halogen substitutions should be expected to degrade faster. However, it has been shown both experimentally and computationally that aromatics with more total halogen substitutions react much faster than aromatics with less total halogen substitutions [116, 117, 132], whereas Baumgartner et al. observe a very strong trend to the opposite effect. For both (poly)fluoro- and (poly)chloro- benzenes, the computational free energy of activation predictions of Sadowsky et al. are presented beside the negative logarithm of the experimentally observed reaction rates of Baumgartner et al. in Figure 5.1.

Figure 5.1: Relative rates of dehalogenation over a Rh/Al_2O_3 catalyst observed experimentally by Baumgartner et al. [37] (in negative log form) compared to computational predictions of free energies of activation for nucleophilic aromatic substitution reactions leading to dehalogenation in aqueous solution reported by Sadowsky et al. [132]. (in kcal mol^{-1}).

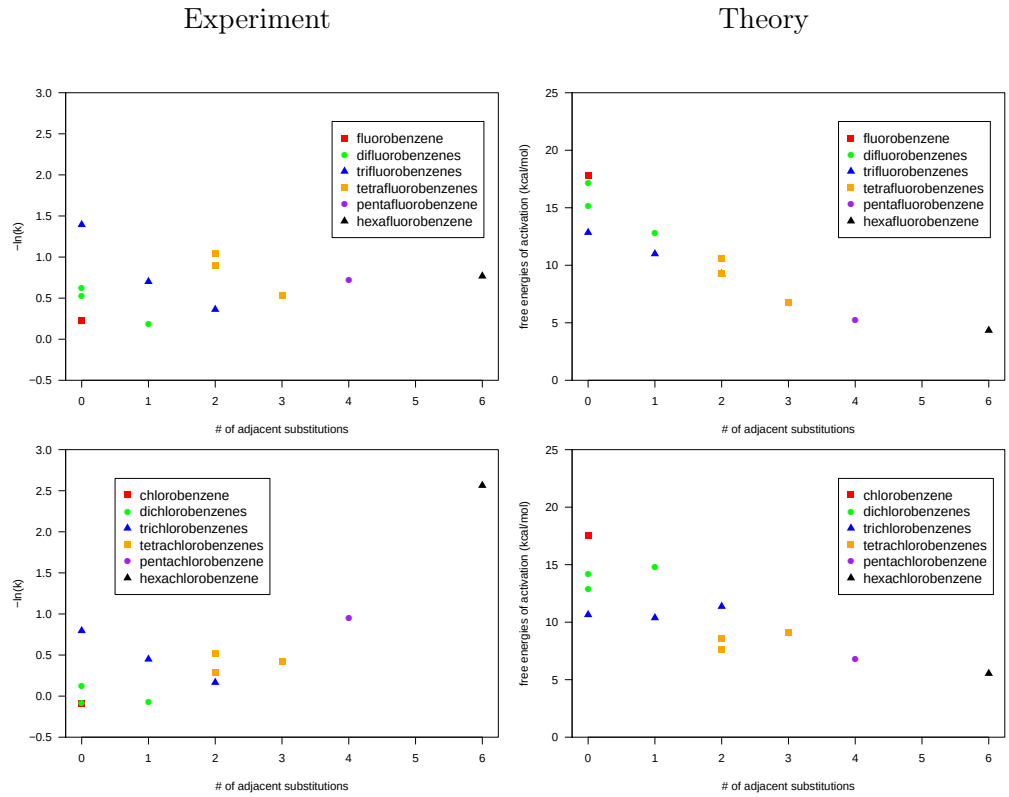

Knowledge of the binding of halogenated aromatics to Rh surfaces could therefore yield significant insight into the mechanism of dehalogenation. If, for example, it can be shown that there is significantly decreased binding for highly substituted aromatics, then the proposed nucleophilic aromatic substitution mechanism is still plausible. In this contribution, the binding of (poly)fluoro- and (poly)chloro- benzenes to two model

complexes, a Rh cation and a neutral Rh trimer, are studied using a density functional theoretical protocol.

5.2 Materials and Methods

5.2.1 Computational Methods

All DFT calculations are carried out at the hybrid generalized-gradient level of density functional theory using the B1LYP functional [133], which has been demonstrated to perform well for 4d transition metals and ions [134]. The standard 6-311+G(3df,2p) basis set are used for all main group elements. For transition metals, the SDD quasi-relativistic pseudopotentials [135] and their associated basis sets are used. An integration grid of 99 radial shells and 590 angular points per shell is used and the geometry of each structure is optimized to a maximum force of $2.0 \cdot 10^{-6}$ au, a root mean square (RMS) force of $1.0 \cdot 10^{-6}$ au, a maximum internal coordinate displacement of $6.0 \cdot 10^{-6}$ au, and a RMS internal force displacement of $4.0 \cdot 10^{-6}$ au. All optimized geometries are confirmed to be local minima on the model chemistry potential energy surface by analytical calculation of the vibrational frequencies following the usual quantum-mechanical harmonic-oscillator approximation. These vibrational frequencies are scaled by a factor of 0.978, a parameter that has been empirically fit for B1LYP to reproduce experimental zero-point vibrational energies [54], and used in the calculation of zero-point vibrational energies and vibrational partition functions. These quantities, along with the ideal-gas,

particle-in-a-box, and rigid-rotator partition functions, are used to calculate thermal contributions to the enthalpy and Gibbs free energy of each structure using the thermo.pl script [55]. All calculations are performed with the Gaussian 09 electronic structure suite, Revision C.01 [62].

5.2.2 Statistical Methods

The R software environment, version 2.15.2 [63] is used for all linear regression analysis.

5.3 Results and Discussion

5.3.1 Binding with Neutral Rh Trimer

We first explore the hypothesis that aqueous adsorption of aromatic substrates on to the rhodium surface described by Baumgartner et al. is largely a consequence of the aromatic ring forming three η^2 interactions with adjacent Rh atoms on the Rh surface. A neutral Rh trimer with Rh–Rh bond lengths constrained to a distance of 2.689 Å is used as a model for this mode of interaction, where the value of 2.689 Å is taken from the experimental bond distance for bulk Rh [136]. The electronic energies of binding of the (poly)halogenated benzenes to these geometrically constrained trimers are reported in Table 5.4. For many of the substrates, there is only one unique binding configuration; for the substrates that have two possible configurations, both are optimized. In Table 5.4, the binding modes which include an η^2 interaction with the C atoms with locants 1 and 2 are listed first, followed by the binding modes which include an η^2 interaction

with the C atoms with locants 2 and 3. As full optimizations are not performed, it is not possible to calculate vibrational partition functions for these complexes. Thus, only the electronic energies of binding, and not free energies of binding, are reported in Table 5.4. The complexes formed by benzene, hexafluorobenzene, and hexachlorobenzene are notable for their high symmetry (C_{3v}), making a full geometric analysis feasible; for these three complexes, all seven geometric degrees of freedom are tabulated in Figure 5.2.

Figure 5.2: Geometrical degrees of freedom (in Å and degrees) for $Rh_3C_6X_6$ (X = H, F, Cl). The Rh-Rh bond distances are given in italics to indicate that the bond distance is constrained.

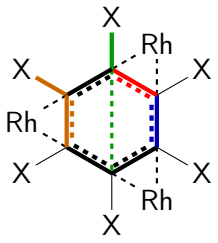

	H	F	Cl
$\mathbf{r}_{Rh-Rh}$	*2.689*	*2.689*	*2.689*
$\mathbf{r}_{Rh-C}$	2.127	2.066	2.075
$\mathbf{r}_{C-C,bound}$	1.429	1.443	1.453
$\mathbf{r}_{C-C,unbound}$	1.457	1.472	1.482
$\mathbf{r}_{C-X}$	1.083	1.349	1.757
$\mathbf{A}_{C-C-X,para}$	162.5	154.1	159.8
$\mathbf{A}_{C-C-X,ortho,bound}$	119.5	118.2	118.7

In order to study the additive contributions of substitution patterns to the predicted binding energies, the multiple linear regression in Eq. 5.1 is proposed. The energies are analyzed in terms of the number of η^2 interactions with pairs of unsubstituted carbons (n_{HH}), pairs of substituted carbons (n_{FF} and n_{ClCl}), and mixed substituted and unsubstituted pairs of carbons (n_{HF} and n_{HCl}). An example of the assignment of these parameters can be found in Figure 5.2. The results of the multiple linear regression are given in Table 5.3.

Table 5.1: Electronic energies of binding for (poly)fluoro- (F) and (poly)chloro- (Cl) benzenes with a geometrically constrained Rh trimer (in kcal mol^{-1}).

	PG	F	Cl
benzene	C_{3v}	*(-30.2)*	*(-30.2)*
mono	C_1	-29.2	-30.5
1,2-di	C_s	-29.6	-31.1
	C_s	-29.2	-30.0
1,3-di	C_1	-28.3	-31.0
1,4-di	C_s	-28.5	-30.6
1,2,3-tri	C_1	-29.7	-30.6
1,2,4-tri	C_1	-28.8	-31.3
	C_1	-28.4	-30.2
1,3,5-tri	C_3	-27.7	-31.6
1,2,3,4-tetra	C_s	-30.4	-30.7
	C_s	-30.0	-29.6
1,2,3,5-tetra	C_1	-29.2	-30.9
1,2,4,5-tetra	C_s	-29.0	-30.6
penta	C_1	-30.7	-29.9
hexa	C_{3v}	-32.4	-28.8

$$\Delta E_B \approx c_{HH}n_{HH} + c_{HF}n_{HF} + c_{FF}n_{FF} + c_{HCl}n_{HCl} + c_{ClCl}n_{ClCl} \tag{5.1}$$

The regression demonstrates that the most favorable bonding interaction is with pairs of fluorinated sites (c_{FF}), while the least favorable interaction is with mixed pairs of fluorinated and unsubstituted sites (c_{HF}). Interestingly, this trend is reversed for

Table 5.2: Classification of η^2 interactions for 1,2,4-trifluorobenzene.

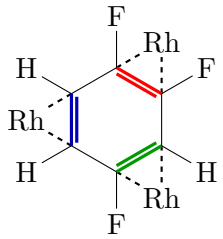

$n_{HH} = 1$, $n_{HF} = 1$, $n_{FF} = 1$

Table 5.3: Multiple linear regression of the electronic energies of binding of (poly)halogenated benzenes and Rh trimer (in kcal mol^{-1}).

c_{HH}	c_{HF}	c_{FF}	c_{HCl}	c_{ClCl}	R^2
-10.0 ± 0.1	-9.3 ± 0.1	-10.5 ± 0.1	-10.3 ± 0.1	-9.9 ± 0.1	0.9999

chlorinated aromatics; interactions with mixed pairs of chlorinated and unsubstituted sites (c_{HCl}) are more favorable than pairs of unsubstituted sites (c_{HH}), while interactions with two chlorinated sites (c_{ClCl}) are slightly less favorable than interactions with two unsubstituted sites (c_{HH}). The strength of the correlation suggests one could arrive at an understanding of the binding of all of the substrates from an analysis of just five of the substrates considered: benzene, 1,3,5-trifluorobenzene, hexafluorobenzene, 1,3,5-trichlorobenzene, and hexachlorobenzene.

A partial explanation of the observed trends in binding energies can be found in the $\pi^\star$ orbitals of the substrates. The ionization energies of all of the substrates are higher in magnitude than that of the Rh trimer, and so one would expect some degree of charge transfer from the Rh trimer to the substrate $\pi^\star$ orbitals in the bound complexes. The energies of the $\pi^\star$ orbitals of selected substrates are reported in Figure 5.4, along with the sum of the APT charges [137] on the substrates while bound to the rhodium trimer. The results confirm that substrates with the lowest $\pi^\star$ energy levels have significantly more charge transfer from the rhodium trimer to the aromatic substrate. The geometries of these compounds in their bound complexes is also worth noting; as reported in Figure 5.2, hexachlorobenzene has slightly longer C–C bonds than hexafluorobenzene, and even longer C–C bonds than benzene. In other words, complexes with more charge

transfer have weaker C–C bonding (owing to increased $\pi^\star$ density). The trend in $\pi^\star$ energies gives a plausible explanation for why the (poly)chlorobenzenes, on average, bind better than the (poly)fluorobenzenes. It also suggests a reason for why 1,3,5-trichlorobenzene binds particularly well; while the $\pi^\star$ orbitals of 1,3,5-trifluorobenzene are about half way between the levels of benzene and hexafluorobenzene, the $\pi^\star$ orbitals of 1,3,5-trichlorobenzene are significantly lower than the mean of the levels of benzene and hexachlorobenzene.

Table 5.4: Energies of the lowest $\pi^\star$ orbitals (in eV) of selected substrates and the sum of the APT charges on the substrates while bound to Rh_3.

	$e(\pi^\star)$	$q(C_6X_6)$
benzene	-0.14	0.23
1,3,5-trifluorobenzene	-0.59	0.05
hexafluorobenzene	-0.94	-0.09
1,3,5-trichlorobenzene	-1.10	0.00
hexachlorobenzene	-1.54	-0.17

However, the charge transfer analysis does not offer a full explanation of the results. An analysis of the geometric deformation of the substrates is therefore carried out through partial optimizations of benzene, hexafluorobenzene, and hexachlorobenzene with the H, F, and Cl nuclei constrained to four different symmetric out-of-plane angles ($\theta = 5°, 10°, 15°, 30°$). The differences in the electronic energies of the substrates at the constrained geometries with respect to the electronic energies at their unconstrained geometries, referred to hereinafter as the deformation energies of the respective substrates, are plotted against the angular constraints, or deformation angles, of the

respective substrates in Figure 5.3.

Figure 5.3: Deformation energies (in kcal mol^{-1}) of C_6X_6 (X=H,F,Cl) plotted against their respective deformation angles. Points circled in red are the extrapolated deformation energies at the out-of-plane angles of the Rh_3-bound C_6X_6 geometries. Vertical dashed lines mark the out-of-plane angles of the hydrogen (left) and fluorine (right) atoms in the bound geometry of 1,3,5-trifluorobenzene.

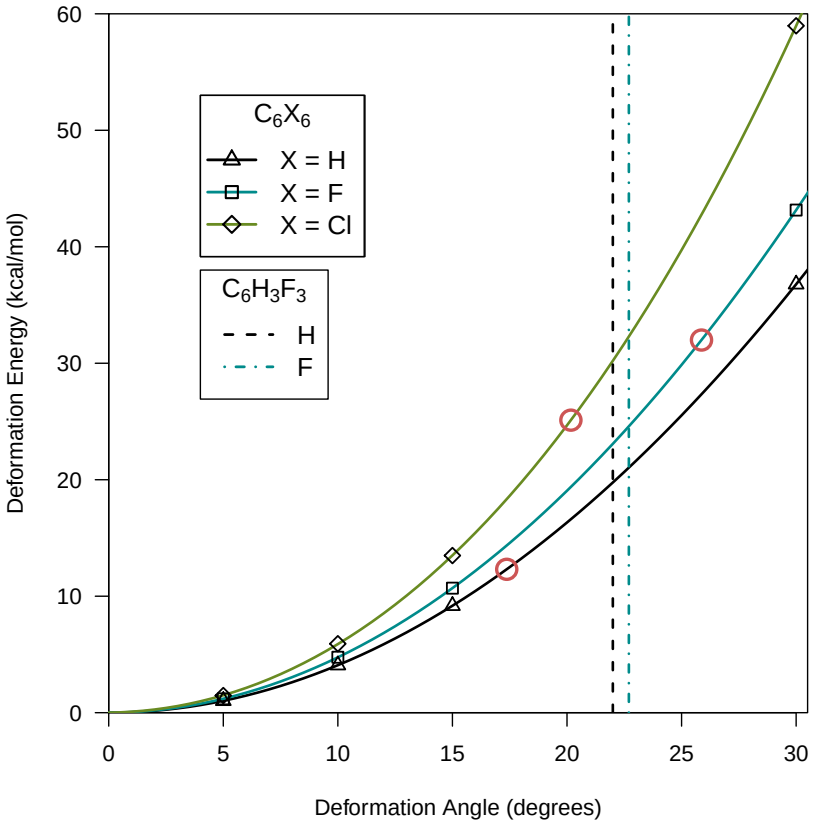

Symmetric out-of-plane bending appears to come at a significantly greater energetic cost for the substituted benzenes than it does for benzene, and appears to come at a

particularly high cost for hexachlorobenzene. This latter observation offers an attractive explanation for why hexafluorobenzene has a stronger predicted binding energy than does hexachlorobenzene, despite hexachlorobenzene having the more favorable π orbital arrangement for charge transfer. Inspection of Figure 5.2 shows that the out-of-plane angles also correlate with rhodium-carbon bond distances, suggesting that hexafluorobenzene is able to bind closer to the rhodium trimer, resulting in a stronger interaction, due to its relative ease of out-of-plane bending. This analysis also offers an explanation for the poor binding of 1,3,5-trifluorobenzene. While fluorinated sites have a tendency to bind close to the rhodium surface, with a significant degree of tetrahedralization, unsubstituted sites have a tendency to bind farther away, with less tetrahedralization. 1,3,5-trifluorobenzene is thus forced into a compromise between the two (as visualized by the vertical dashed lines in Figure 5.3), which comes at a severe energetic cost for the unsubstituted sites and restrains the substituted sites from their ideal binding position.

The electronic energies of binding for the (poly)fluoro- and (poly)chloro- benzenes with Rh_3 are reported beside the experimental rates of dehalogenation from Baumgartner et al. in Table 5.4. Although the experimentally observed trend that binding strongly increases with an increasing number of adjacent fluorine substitutions is correctly predicted by the Rh_3 model, the model also incorrectly predicts that an increased *total* number of fluorine substitutions results in increased binding. On the other hand, the Rh_3 model fails completely for the (poly)chlorobenzenes. It does correctly predict the correct trend in respect to the *total* number of halogen substitutions, but not with a

Figure 5.4: Relative rates of dehalogenation over a Rh/Al_2O_3 catalyst observed experimentally by Baumgartner et al. [37] (in negative log form) compared to computational predictions of the energies of binding in Table (in kcal mol^{-1}).

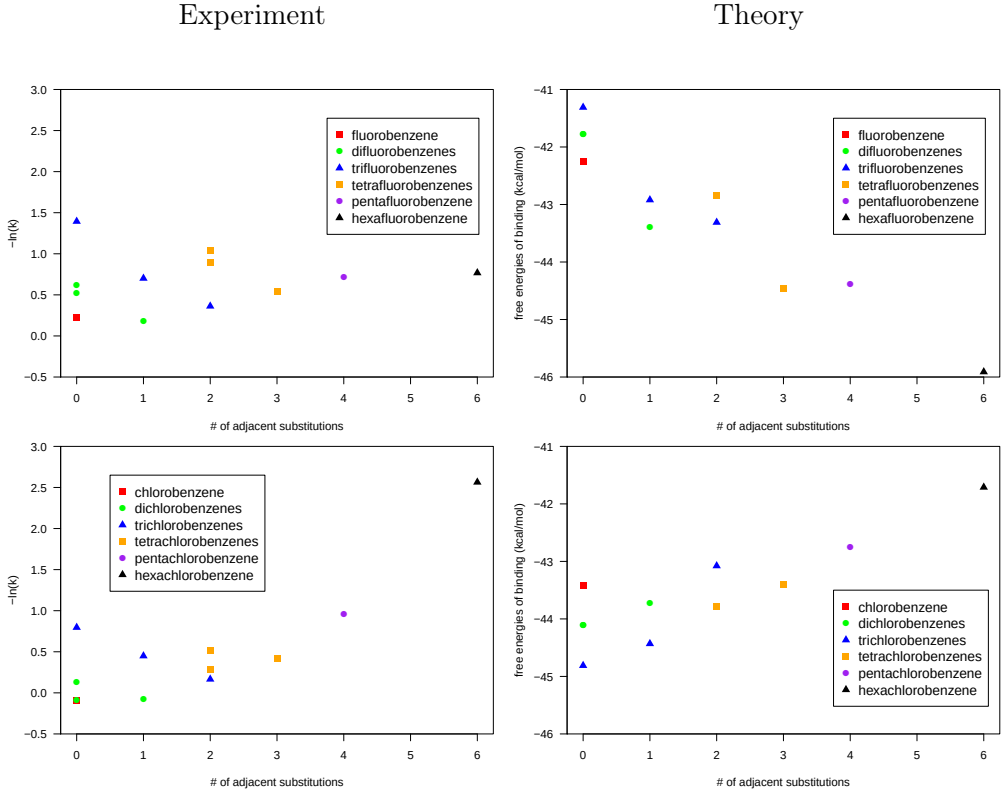

large enough slope to correct for the much faster reactivity predicted for increasing total chlorine substitutions that the nucleophilic aromatic substitution hypothesis predicts.

5.3.2 Binding with Monatomic Rh Cation

We therefore explore an alternative hypothesis, namely that the binding of the aromatic substrates to the rhodium surfaces is largely electrostatic in nature. This hypothesis is tested by studying the complexes formed from the interaction of the (poly)fluoro- and

(poly)chloro- benzenes and a rhodium cation. The Gibbs free energies of binding of these complexes are reported in Table 5.5.

Table 5.5: Gibbs free energies of binding of (poly)halogenated benzenes with Rh cation (in kcal mol^{-1}).

	PG	$\Delta G(F)$	$\Delta G(Cl)$
benzene	C_{6v}	*(-46.1)*	*(-46.1)*
mono	C_s	-39.8	-40.4
1,2-di	C_s	-34.8	-37.0
1,3-di	C_s	-34.3	-36.2
1,4-di	C_{2v}	-34.2	-35.9
1,2,3-tri	C_s	-29.8	-33.6
1,2,4-tri	C_1	-28.8	-32.2
1,3,5-tri	C_{3v}	-28.6	-32.0
1,2,3,4-tetra	C_s	-24.5	-30.2
1,2,3,5-tetra	C_s	-24.2	-29.6
1,2,4,5-tetra	C_{2v}	-24.0	-29.3
penta	C_s	-20.0	-25.8
hexa	C_{6v}	-15.8	-25.2

The binding free energies follow two major trends. The most significant trend is that with increasing halogen substitution, the binding weakens. This trend is particularly pronounced for fluorine substitution. A second trend is that among the (poly)halogenated benzenes with the same number of halogen substitutions, structures with the highest number of adjacent substituted sites are predicted to have the strongest binding. The first trend can be explained by the well-known effect that increasing halogen substitution causes a weakening and eventual inversion of the quadrupole moment of benzene, which otherwise has a negative electrostatic potential at its center of mass and along its central axis above the ring due to the polarization of the carbon-hydrogen bond. It is therefore not surprising that this trend is particularly pronounced for (poly)fluorobenzenes, as C–F bonds are more highly polarized than C–Cl bonds. Among substrates with the

same number of halogen substitutions, the substrates with the most adjacent substituted sites have by mathematical necessity also the most adjacent unsubstituted sites. The dipole moment that results from this explains the latter trend. In the presence of a substrate with a dipole moment, the cation will bind off-center in the direction of the largest grouping of unsubstituted sites, which is more electrostatically favorable. The free energies of binding for the (poly)fluoro- and (poly)chloro- benzenes are reported beside the experimental rates of dehalogenation from Baumgartner et al. in Figure 5.5.

Figure 5.5: Relative rates of dehalogenation over a Rh/Al_2O_3 catalyst observed experimentally by Baumgartner et al. [37] (in negative log form) compared to computational predictions of the free energies of binding in Table (in kcal mol^{-1}).

Experiment Theory

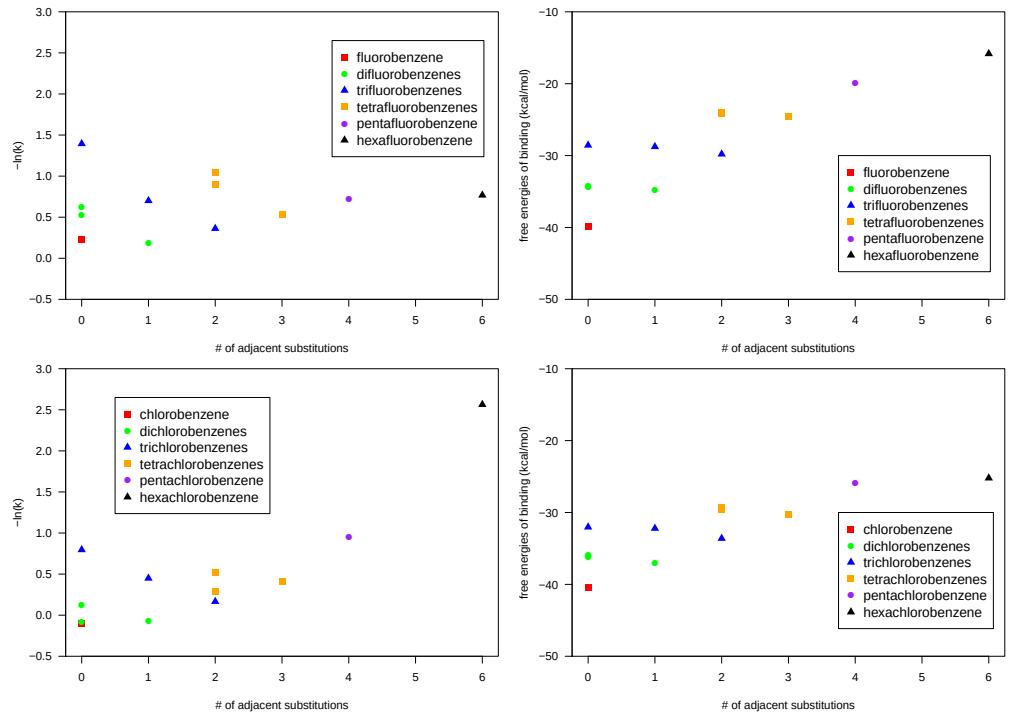

One possible explanation for the apparent correlation between the Rh cation binding free energies and the experimental reaction rates is that the Rh particles have a positive charge and therefore a positive ζ-potential, which is known to occur for Rh/Al_2O_3 particles in aqueous solution [138]. However, a cation-π interaction is not a very sophisticated model for a metal surface with a positive ζ-potential, and possibly overestimates the real electrostatic effect. It is also plausible that there are multiple binding modes, and that the ones which are more electrostatic in nature (for example, binding at the site of surface defects) lead to increased reactivity.

5.3.3 Vibrational Spectroscopy

Vibrational spectroscopy provides a convenient means to compare the model binding complexes studied here with experimental observations of Rh-aqueous interfaces. In one particularly relevant study, Zou et al. [139] have reported surface-enhanced Raman (SERS) spectra of benzene adsorbed onto Rh- and Pd- plated electrodes in aqueous solution. Key mode assignments from these spectra are reported in Table 5.6 along with the computationally predicted vibrational modes of benzene and the model $M_3(C_6H_6)$ (M = Rh, Pd) complexes. Table 5.6 also reports the vibrational frequencies of the $Rh(C_6H_6)^+$ model complex; however, comparison to an analogous C_{6v} palladium complex is not possible due to the instability of the Pd(I) ion. Instead the vibrational frequencies of the C_{6v} $Pd(C_6H_6)^{2+}$ complex are reported. The convention established by Wilson [140] is used to identify each mode in Table 5.6 and thereafter.

Table 5.6: Comparison of experimental aqueous SERS frequencies of benzene adsorbed on Rh and Pd electrodes and computed quasi-harmonic frequencies of benzene bound to model Rh and Pd surfaces (in cm^{-1}).

			Rh			Pd		
description	mode	benzene	exp.[a]	M_3	M^+	exp.[a]	M_3	M^{2+}
M-C stretching	ν_{M-C}		355	380	223	250	281	223
C-C out-of-plane bending	$\nu_{16}(e_{2u})$	405	495	468	401	430	446	349
C-C-C in-plane bending	$\nu_6(e_{2g})$	609	605	571	600	590	583	579
C-H out-of-plane bending (symmetric)	$\nu_{11}(a_{2u})$	681	795	778	780	735	723	804
ring breathing	$\nu_1(a_{1g})$	994	885/970[b]	863	968	930/955[b]	892	951
C-H in-plane bending	$\nu_{15}(b_{2u})$	1150	*1140*[c]	1140	1159	*1155*[c]	1145	1178
C-H in-plane bending	$\nu_9(e_{2g})$	1178	*1140*[c]	1109	1163	*1155*[c]	1132	1160
C-H in-plane bending (symmetric)	$\nu_3(a_{2g})$	1362	1350	1320	1356	1330	1336	1362

[a] Ref. 139. [b] See text for explanation. [c] These modes are tentatively assigned as ν_9 in ref. 139, although Zou et al. note the possibility that ν_{15} could be the correct assignment.

One interesting feature of the spectra reported by Zou et al. is the observation of two ν_1 modes. The ratio of the intensities of the two peaks are reported to be concentration dependent, with the higher frequency ν_1 peak disappearing when the aqueous benzene solution is sparged. On the basis of this evidence, Zou et al. ascribe the higher-frequency peak to a "physisorbed" state and the lower frequency peak to a stronger, "chemisorbed" state. The calculated frequencies of the M_3 complexes are in very good agreement with the vibrational frequencies observed by Zou et al., including the lower ν_1 frequencies but excluding the higher ones. On the other hand, the calculated frequencies of the M^+ and M^{2+} complexes are not in very good general agreement with the frequencies observed by Zou et al., with the notable exception of the higher ν_1 values. The results suggest that the dominant bound geometry of benzene at an aqueous-Rh interface is one with three η^2 interactions similar to the Rh_3 model. However, there are many plausible binding geometries that could be responsible for the "physisorbed" state identified by

Zou et al.; the data in Table 5.6 is insufficient to draw conclusions. It is worth noting that the electrode used by Zou et al. is described as being on average 4 ML thick, and very smooth. It is therefore very likely that the Rh surface described by Baumgartner et al., with reported mean particle diameter of 5 μm, contains significantly more defect sites. It is also plausable that, whether or not cation-π bonding is responsible for the "physisorbed" state observed by Zou et al., it could occur at defect sites of positively charged Rh particles.

5.3.4 Free Energies of Solvation

Thus far, two types of data have been considered: factors affecting the binding of aromatics to Rh surfaces and factors affecting the reactivity of the aromatics free of any consideration of the Rh surface. Another possibility is that, once the aromatic substrate is bound to the Rh surface in a geometry analogous to the M_3 model complexes, one or more of the η^2 interactions with the Rh surface must unbind in order that the reaction can proceed via the proposed nucleophilic aromatic substitution mechanism at the unbound portion of the substrate. If this is indeed the case, one would expect the reaction rates to have an inverse correlation with the affinity of the unbound part of the substrate for aqueous solution. As a crude approximation to this, the free energies of solvation of each substrate (in its entirety) are considered. Sadowsky et al. have previously reported computational predictions of the free energies of solvation of the

(poly)fluoro- and (poly)chloro- benzenes using a combined density functional theoretical and continuum solvation model with an isodesmic formalism that makes careful use of experimental Henry's law constant data [96]. Figure 5.6 compares the experimental rates of Baumgartner et al. with computational predictions of Sadowsky et al.

Figure 5.6: Relative rates of dehalogenation over a Rh/Al_2O_3 catalyst observed experimentally by Baumgartner et al. [37] (in negative log form) compared to computational predictions of the free energies of solvation reported by Sadowsky et al. [96] (in kcal mol^{-1}).

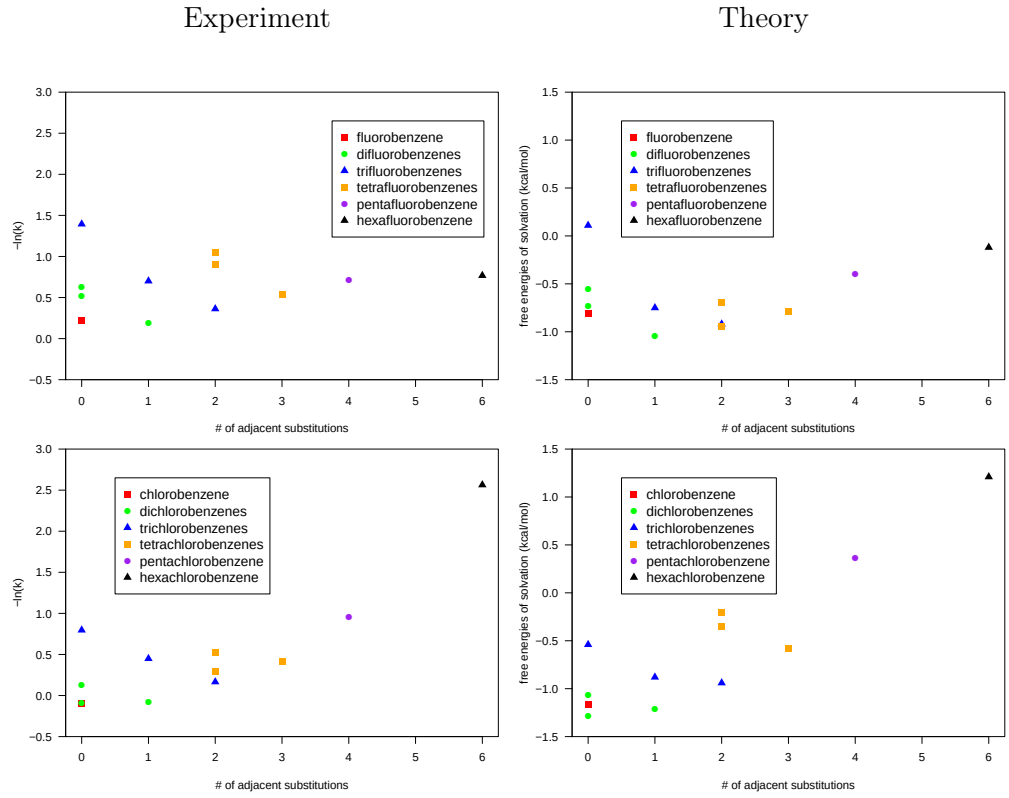

The correlation of the free energies of solvation with the experimental rates is strong, and is especially notable in that it is the only data set considered here which correctly

predicts especially slow reactivity for hexachlorobenzene.

The binding and reactivity of aromatic substrates at rough aqueous-Rh/Al_2O_3 interfaces is complex. We propose that an understanding or even a quantitative prediction of the major binding mode available to an aromatic substrate at such an interface in insufficient to understanding and predicting the reactivity of that substrate on that surface. Rather, one must aim for an understanding of the weak or partially bound geometries available to substrates. In the specific case of the system reported by Baumgartner et al., we propose that physisorbed states, electrostatic interactions with surface defects, and η^4 binding modes may play key roles in understanding catalytic dehalogenation at Rh/Al_2O_3 surfaces.

Chapter 6

Extensions to Highly Condensed Aromatic Systems[1]

6.1 Introduction

Carbon nanotubes (CNTs) are an emerging class of materials whose remarkable properties have generated considerable scientific and commercial interest along with human and ecological health concerns. CNTs have been demonstrated to have not only significant toxicity to human cell lines [141–143], but also significant solubility in aqueous solutions of natural organic matter [144]. With accelerating global production capacity,

[1] **Adapted with permission of The Royal Society of Chemistry. Sadowsky, D.; McNeill, K.; Cramer, C.J. Electronic structures of [n]-cyclacenes (n= 6-12) and short, hydrogen-capped, carbon nanotubes. *Faraday Discussions*, 2010, *145,* 507-521.**

CNTs could thus become a hazardous but poorly understood aquatic pollutant. Understanding the environmental transformations of CNTs, such as their reactions with photochemically produced reactive intermediates, could be key to better understanding their fate in aquatic systems since such transformations play critical roles in the environmental fate of many other pollutants [145–147]. For example, early experimental [148–150] and theoretical [151–155] work has shown that nanotubes are susceptible to reaction with singlet oxygen (and certain fullerenes and nanotubes are singlet oxygen sensitizers [148, 156] but the identification of subsequent products has been difficult to accomplish experimentally, although 1,2- and 1,4-endoperoxides are typically invoked as initial reactive intermediates. The study of this chemistry has been hindered by the analytical challenges associated with characterizing these heterogeneous systems.

Single-walled (SW) CNTs have been studied widely with electronic structure calculations, largely through the use of periodic boundary conditions [157–160]. Although these methods have had great success in predicting electronic and material properties of pristine SWNTs, models with periodic boundary conditions are less useful for the study of localized phenomena like photochemical degradation or other surface reactivity involving significant covalent modification and/or distortion of the CNT molecular framework, unless very large unit cells are chosen so as to guarantee a lack of interaction between periodically reproduced modification sites. In such instances, it may be more computationally efficient to employ a finite-length nanotube model, although the adoption of such a model does required that one ensure that results are not complicated

by edge effects if too small a length is chosen. Of course, the edge reactivity of actual nanotubes released into the environment may itself be of interest, in which case the utility of the finite length model is obvious, and indeed an interesting question is the degree to which edge effects do influence reactivity.

Recourse to finite-length nanotube models also facilitates the use of implicit solvation models [161, 162] that play a key role in the construction of overall modeling protocols having relevance for the study of reactions under environmental conditions. Noting all of these relative advantages and disadvantages, finite-length models have come into increasing use in calculations of CNT electronic properties [163–165] and the convergence of their electronic properties to a continuum limit with increasing length has also been studied [165–167].

In order to study the potential chemical reactivity of carbon nanotubes and their degradation products in the environment, and to aid in the experimental characterization of such materials, an ideal theoretical model should offer, at low computational cost, an ability to model geometric and energetic perturbations associated with changes in local structure induced by adsorbed species or reactions that break C–C bonds. In addition, reasonably accurate predictions of relevant spectroscopic data (e.g., in the UV/Vis or infrared regions of the spectrum) should be possible. For systems of the size envisioned to be environmentally relevant, it is clear that only density functional theory (DFT) is likely to offer an immediate, practical, quantum mechanical alternative [168], although it is possible that semiempirical models like size-consistent-charge density functional tight

binding (SCC-DFTB) theory may also ultimately prove useful [169, 170].

A significant challenge associated with using Kohn-Sham (KS) DFT to model short nanotubes, however, is that the single-determinantal nature of the KS formalism is subject to instability if the frontier orbital separation (i.e., the energy gap between the occupied and unoccupied orbitals) becomes sufficiently small. In such instances, restricted solutions to the restricted KS DFT self-consistent field equations become unstable to symmetry breaking to unrestricted solutions having poorly defined spin states. For instance, Chen et al. [171] have reported that [6]-cyclacene is predicted to have a singlet ground state with DFT, in agreement with multireference second-order perturbation theory calculations, but only when a broken-symmetry (BS) KS formalism is employed. We note that Hachmann et al. [172], based on density matrix renormalization group calculations of the linear polyacenes for lengths up to 12, have also reported substantial multireference character in the singlet ground states with increasing length, so the cyclic nature of the cyclacenes is not solely responsible for this phenomenon, and polyacenes as a general class appear to pose significant challenges to single determinantal electronic structure methods like Kohn-Sham DFT.

Here, we undertake a characterization of the length-dependent electronic structures of various hydrogen-capped, zig-zag, single-walled, carbon nanotubes, having walls composed of 6 to 12 rings around and lengths ranging from 1 (a [n]-cyclacene) to 6, using broken-symmetry density functional theory together with a spin purification formalism.

We examine the relative utilities of the local M06-L functional and the perennially popular hybrid B3LYP functional. In the [n]-cyclacene cases, we also compare our BS DFT predictions to CASSCF/CASPT2 multireference second-order perturbation theory calculations, as the latter model handles the multiconfigurational character of potential bi- or polyradicaloid singlet states in a rigorous fashion.

6.2 Computational Methods

6.2.1 Geometries

All geometries were fully optimized at the M06-L [173] level of theory using the 6-31G(d) set [174]. Separate geometries were optimized for each spin state and for singlet states a broken-symmetry formalism was employed. As M06-L is a local functional, it is possible to speed the computation of Coulomb integrals by adopting the resolution of the identity approximation with a fitting basis set [175–178], and we took advantage of this efficiency. All geometries were verified as local minima by the computation of analytical vibrational frequencies.

6.2.2 DFT energies

In certain chemical species, e.g., polynuclear transition-metal compounds, one may consider the overall molecular system to be composed of one or more subsystems over each of which unpaired spin is localized. In such instances, it can be convenient to use a

spin-labeled model Hamiltonian that describes the spin-spin interactions between localized centers as though they were coupled angular momenta; the appropriate formalism for such a treatment was first described by Heisenberg [179] and Dirac [180] and later elaborated by Van Vleck [181] and Slater [182]. If, for the sake of simplicity, we restrict ourselves to considering two subsystems A and B, the eigenstate energies of the Heisenberg-Dirac Hamiltonian are given by

$$E_S = -J_{AB}S(S+1) \tag{6.1}$$

where the coupling energy parameter J_{AB} can be determined from electron repulsion integrals and the spin S takes on whole or half-integer values ranging from $|S_A - S_B|$ to $|S_A + S_B|$.

Continuing to consider the simplest case, let us assume only one unpaired electron in each subsystem A and B. In that case, the wave function for the high-spin triplet state should be well represented by a single Slater determinant formed from the usual molecular orbitals determined as linear combinations of atomic orbitals; such situations are well suited for treatment by DFT within the single determinantal Kohn-Sham formalism. In contrast, the wave function for the antiferromagnetically coupled singlet state, in the limit of weak coupling, requires at least two determinants for a balanced description and is thus problematic for Kohn-Sham DFT [161], so that it is not generally possible to compute the energy difference between the two states directly [183–185]. However, as

originally discussed by Ziegler et al. [186] and Noodleman [187], a non-physical broken-spin-symmetry state, deriving from an unrestricted DFT calculation in which the equal numbers of alpha and beta electrons are allowed to occupy spatially distinct orbitals, can be useful for predicting the coupling parameter J_{AB} for use in eq. 6.1. In particular, Noodleman [187] originally indicated that in the limit of weak coupling [188, 189].

$$J_{AB} = -\frac{^{HS}E - ^{BS}E}{4|S_A||S_B|} \tag{6.2}$$

where HSE and BSE are the energies computed from the high-spin and broken-symmetry determinants, respectively, for the same molecular geometry, and SA and SB are the spins on centers A and B, respectively (e.g., both $\frac{1}{2}$ in the example of one spin on each center). Subsequently, Yamaguchi and co-workers [190, 191] suggested a modification designed to be valid for couplings ranging from weak to strong, namely

$$J_{AB} = -\frac{^{HS}E - ^{BS}E}{^{HS}<S^2> - ^{BS}<S^2>} \tag{6.3}$$

where $<S^2>$ is the expectation value of the total spin operator applied to the appropriate determinant. In the limit of weak coupling, for the example of one spin on each center A and B, we would expect $^{HS}<S^2>$ to be 2 (the correct eigenvalue for a triplet) and $^{BS}<S^2>$ to be 1 (the average of a singlet and a triplet) and the equivalence of eqs. 6.2 and 6.3 is demonstrated. In the limit of strong coupling, i.e., where a restricted DFT formalism would be appropriate for the singlet state, $^{BS}<S^2>$ will be zero (i.e., there

is no broken symmetry at all), and using the value for J_{AB} computed from eq. 6.3 in eq. 6.1 will cause the difference between the singlet and triplet states to be simply ${}^{HS}E$ – ${}^{BS}E$, which is the proper result (a so-called ΔSCF result) if both states are suited to computation by a single determinantal formalism. The Heisenberg-Dirac model has been used extensively in conjunction with DFT to explain magnetic properties in metal coordination compounds [192–194]. One of our goals in this work is to examine its utility when applied to the [n]-cyclacene series and short nanotubes, where it is less obvious that subsystems as distinct as metal atoms can be easily identified, and it can moreover be difficult to decide the proper spin state to assign as the high-spin limit in eq. 6.3.

6.2.3 Multireference energies

CASSCF/CASPT2 calculations [195] were performed for the DFT optimized [n]-cyclacene geometries. The CASSCF model constructs pure spin states as proper combinations of spin-adapted configurations, thereby accounting for the non-dynamical correlation associated with an open-shell singlet, for example, and the CASPT2 model adds an accounting for dynamical electron correlation energy at the level of second-order perturbation theory applied to the CASSCF reference.

The [n]-cyclacenes with an even-numbered primary axis of rotation were treated in D_{2h} symmetry and were run with an 8 electrons in 10 orbitals, denoted (8,10), active space. This active space was selected based on an examination of the relative energies

(and near degeneracies) of the frontier orbitals in the various systems. Systematic consideration of larger and smaller active spaces established that the inclusion of additional occupied or virtual orbitals failed to change the occupation numbers of those orbitals from very near 2 and 0, respectively, and moreover had little effect on computed state-energy splittings. Shrinking the active space to smaller than (8,10), on the other hand, led to large changes in predicted state-energy splittings and significant changes in orbital occupation numbers and overall wave functions. A similar analysis of the [n]-cyclacenes with an odd-numbered primary axis of rotation, which were treated in C_{2v} symmetry, led to the selection of a (12,12) active space. Additional discussion of certain key molecular orbitals is provided in the Results section.

6.2.4 Software

Initial geometries were generated in $D_{(n)h}$ symmetry with the assistance of the online nanotube structure generator TubeGen v.3.3 [196]. All DFT computations were performed with MN-GFM version 4.1 [197], a locally modified version of Gaussian 03 revision D.01 [198]. All CASSCF/CASPT2 calculations were performed with MOLCAS 7.0 [199].

6.3 Results and Discussion

6.3.1 [n]-Cyclacene geometries

We start with the "monomers" of the zig-zag hydrogen-capped nanotube series, the [n]-cyclacenes. With respect to DFT, the M06-L functional [173] is an attractive choice of functional for initial consideration for two reasons. First, as a local functional that can be combined with the resolution of the identity formalism to speed the computation of Coulomb integrals, it is much more efficient for large systems than a hybrid functional. Second, the M05 and M06 family of functionals has been demonstrated to be superior to most other functionals in current use with respect to accurately accounting for attractive non-bonded interactions like dispersion [200–203]. It is not immediately clear that dispersion will be an important consideration in [n]-cyclacenes or short nanotubes, but their construction from polarizable π systems certainly offers the possibility. Thus, all molecular geometries were optimized at the M06-L/6-31G(d) level. As an alternative functional against which to compare, we also consider below the B3LYP functional [204–207], which has seen extensive application to problems of organic structure and reactivity.

Geometry comparisons of the [n]-cyclacenes within the constraints of $D_{(n)h}$ symmetry are particularly facile in so far as each congener is completely characterized by the same geometrical parameters, of which there are only six. These degrees of freedom are the C-H bond length, the declination angle the C-H bonds make relative to the principal symmetry axis, the length of the C-C bonds parallel to the principal symmetry axis, the

length of the remaining "zig-zag" C-C bonds, the interannular dihedral angle ω_1, and the intraannular dihedral angle ω_2 (see Figure 6.1).

Figure 6.1: Geometric degrees of freedom in [n]-cyclacenes.

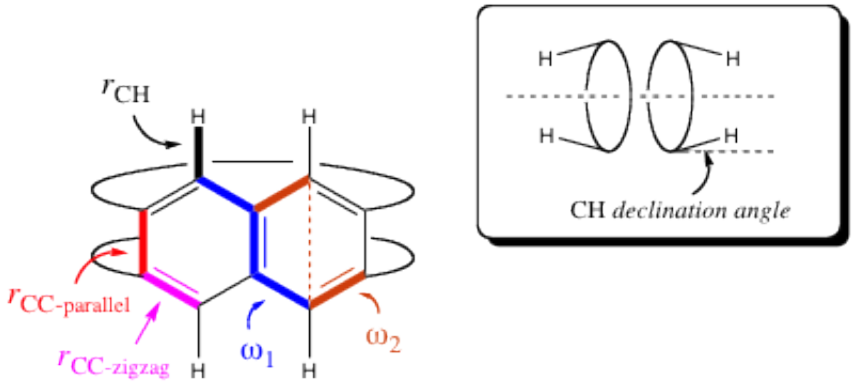

The carbon-hydrogen bond length remains relatively constant (about 1.091 Å) in the [n]-cyclacenes for n = 6-12. With respect to the radial angle made by the C–H bonds relative to the principal symmetry axis, the cyclic nature of the molecules imposes an outward pyramidalization on every carbon atom, with the degree of pyramidalization increasing with decreasing n (see further discussion below). On that basis, one would expect the C-H bonds to depress, or orient inward, relative to the principal axis, and this effect is indeed observed. It ranges from 3.3 deg for n = 6 to 1.9 deg for n = 12. Even for n = 6, this value is not particularly large, but the variation is in the sense expected.

The length of the carbon-carbon bond parallel to the principal symmetry axis increases with increasing cyclacene radius, although the total change from n = 6 to n =

12 is fairly small at 0.012 Å (Table 6.1). This bond length is somewhat sensitive to the spin state under consideration. It is longer by 0.004 Å for triplets relative to singlets and 0.009 Å shorter for quintets, consistent with an electronic structure that localizes interacting spins along each edge of the cyclacene (this point is discussed in more detail below). In such a situation, singlet coupling would be expected to shorten the bond joining the two edges, while triplet coupling will lengthen it to reduce interannular exchange repulsion. Quintet coupling in the smaller cyclacenes causes the parallel C–C bond length to shorten again, as intraannular repulsion now dominates over interannular repulsion, but this effect vanishes with larger size as the two spins on each edge become well separated (vide infra). In principal, the broken-symmetry approach may well overestimate the parallel C–C bond length in the singlet states, since the KS determinants are contaminated by higher spin states. Examples are known in binuclear copper systems [208,209] for example, where singlet geometries optimized using the restricted DFT formalism are energetically more favorable than those optimized at the BS DFT level, even though the restricted method cannot be used to reliably estimate those energies. We were not able to test that issue here, however, as the restricted self-consistent field equations proved very difficult or impossible to converge in most instances.

As might be expected given the benzenoid character of the rings, the other symmetry-unique carbon-carbon bonds, the zig-zag bonds, lengthen or shorten in response to shortening or lengthening of the parallel C–C bonds. The shortest such bond is 1.404 for the triplet state of [12]-cyclacene and the longest is 1.417 for the quintet state of

Table 6.1: Lengths (Å) of C-C bonds for different [n]-cyclacene spin states optimized at the M06-L level of theory.

	Spin State		
n	Singlet	Triplet	Quintet
6	1.446[a]	1.450	
	1.416	1.416	
7	1.466		1.441
	1.409		1.417
8	1.453	1.456	
	1.409	1.409	
9	1.452		1.449
	1.410		1.410
10	1.456	1.460	
	1.406	1.406	
11	1.453		1.453
	1.408		1.407
12	1.458	1.462	
	1.405	1.404	

[a] Bond lenghts are listed for the C-C bond parallel to the principal symmetry axis (above) and the zig-zag C-C bond (below).

[7]-cyclacene, where exchange repulsion between two unpaired spins on the same ring is maximized. We note that the energetic differences associated with different spin-state geometries are not very large. The difference in triplet electronic energies, for example, between the singlet and triplet optimized geometries for the even-numbered cyclacenes is as low as 0.4 kJ/mol in some cases. Of course, if these small differences are additive they may prove more important in the modeling of longer SWNTs.

Finally, symmetry constrains the sum of the two dihedral angles illustrated in Figure 6.1 for any [n]-cyclacene to be equal to twice the interior angle of a corresponding $2n$-sided regular polygon. It is interesting to consider the degree to which strain in the

cyclacene series is associated with these dihedral angles, since they are diagnostic for n. We have approached this question in the following fashion. As the molecular formula for each cyclacene may be expressed as $(C_4H_2)_n$, we may compute the normalized energy of a C_4H_2 fragment in any $[n]$-cyclacene by dividing its total energy by n. If we then plot this normalized energy vs. n^{-1} and fit a curve to this plot, we can determine from the intercept the fragment energy associated with the "unstrained" cyclacene composed of an infinite number of rings (and hence being effectively locally planar at any given ring). The strain energy in a given cyclacene may then be defined as

$$E_{strain}^{[n]} = E^{[n]} - nE_{strain-free}^{(C_4H_2)} \tag{6.4}$$

We may then ask the question, in an acyclic system, what is the strain energy associated with the bending of an otherwise planar polyacene? To model bending of the interannular dihedral angle, we have chosen naphthalene and to model bending of the intraannular dihedral angle we have chosen anthracene. In each case, we have computed the increase in electronic energy as a function of the relevant dihedral angle, optimizing all other degrees of freedom. Over the range of dihedral angles from 150 to 180 deg, the electronic energies are well fit by the expressions

$$E_{strain}^{naphthalene} = a(180 - \omega_1)^2 \tag{6.5}$$

and

$$E_{strain}^{anthracene} = b(180 - \omega_2)^2 \tag{6.6}$$

where ω_1 and ω_2 are the inter- and intraannular dihedral angles, respectively, and a and b take on values of 0.0785 and 0.0792 kJ/mol-deg^2, respectively, at the M06-L/6-31G(d) level.

We may then define a non-interacting reference strain (nirs) energy for a given [n]-cyclacene as

$$E_{nirs}^{[n]} = n[E_{strain}^{naphthalene}(\omega_1^{[n]}) + E_{strain}^{anthracene}(\omega_2^{[n]})] \tag{6.7}$$

Table 6.2: Strain energies in [n]-cyclacenes[a].

	Dihedral angles (deg)		Strain energies (kJ/mol)	
n	ω_1	ω_2	Eq. 4	Eq. 7
6	150.8	149.2	138.1	136.8
7	155.0	153.5	106.8	100.7
8	158.3	156.7	76.2	77.0
9	160.6	159.4	64.1	60.7
10	162.4	161.6	49.2	49.2
11	164.2	163.1	42.2	40.4
12	165.6	164.4	34.2	34.2

[a] Bond lenghts are listed for the C-C bond parallel to the principal symmetry axis (above) and the zig-zag C-C bond (below).

A comparison of strain energies computed from eqs. 6.4 and 6.7 for a given value of n then permits an evaluation of any additional electronic or steric effects associated with the cyclic nature of the [n]-cyclacene. Table 6.2 provides this analysis.

Comparing the strain energies computed from eqs. 6.4 and 6.7, we see that the largest difference between the two, which is for [7]-cyclacene, is only 5.9 kJ/mol, and in the other cases the average difference is only 1.2 kcal/mol. Thus, there seems to be no special stabilizing (or destabilizing) influence associated with the cyclic character of the cyclacenes. The strain is very well approximated as the sum of the individual torsional strains that would be present in the cyclacene's isolated constituent fragments, although the odd numbered cyclacenes show marginally more sensitivity than the even numbered ones in this respect.

6.3.2 [n]-Cyclacene electronic structures

We now consider in more detail the nature of the various cyclacene electronic structures. As described in the methods section, using BS DFT calculations to determine singlet energies requires computation of $< S^2 >$ for the KS determinants. Table 6.3 lists these values at the M06-L and B3LYP levels with the 6-31G(d) basis set. With M06-L, the total spin expectation values for even values of n are near 1, which would be consistent with a determinant formulated as an equal mixture of singlet and triplet states. For odd values of n, on the other hand, the expectation values are near 2, which would consistent with an equal mixture of singlet and quintet.

With B3LYP, the $< S^2 >$ expectation values are about 5% larger than those of M06-L for odd values of n, but about 60% larger for even values of n after 6. Larger values for B3LYP are consistent with the typical observation that hybrid functionals,

Table 6.3: Expectation values (unitless) of S^2 for BS DFT calculations on singlet [n]-cyclacenes with the 6-31G(d) basis set[a].

	Functional	
n	M06-L	B3LYP
6	0.95	1.16
7	1.64	1.66
8	0.88	1.28
9	2.11	2.22
10	0.99	1.62
11	2.35	2.51
12	1.35	2.12

[a] M06-L/6-31G(d) geometries.

like B3LYP, are more prone to spin contamination than local functionals, like M06-L [208–210]. The greater sensitivity in the even numbered cyclacenes compared to the odd ones may simply reflect the lower energy of the quintet states that contaminate a mixed singlet-triplet wave function compared to septet states that would contaminate a mixed singlet-quintet wave function.

We now consider the values of $2J$ computed from eq. 6.3 for M06-L and B3LYP with the 6-31G(d) basis set. From eq. 6.1, we see that $2J$ corresponds to the singlet-triplet splitting with a positive value implying a singlet ground state. As noted in the methods section, in order to use eq. 6.3 one must make a choice of the proper high-spin reference state. With M06-L it seems clear that the triplet state should be chosen for the even-numbered cyclacenes and the quintet state for the odd-numbered ones (although it also seems clear that were the size of the cyclacenes to increase, this choice might become less clear). In the case of B3LYP, on the other hand, one might argue in the even n

cases for either the triplet or the quintet state as the high-spin reference given the larger predicted values of $< S^2 >$. Thus, for even values of n in Table 6.4, we tabulate $2J$ for both choices. With the M06-L functional, to examine the influence of basis set choice, we also include results using the considerably more complete 6-311+G(2df,p) basis set [**?**].

Table 6.4: Predicted $2J$ values (kJ/mol) for the [n]-cyclacenes using eq. 3.[a]

	M06-L		B3LYP	
n	6-31G(d)	6-311+G(2df,p)	$^{HS} < S^2 >= 2$	$^{HS} < S^2 >= 6$
6	51.5	52.8	66.8	103.3
7	32.2	31.7		41.3
8	54.8	54.8	91.4	92.8
9	19.2	17.6		29.0
10	56.9	68.6	229.1	74.4
11	15.9	14.6		27.9
12	46.0	44.8	[b]	68.8

[a] The high-spin reference state for M06-L calculations is taken to be triplet for even n and quintet for odd n. For B3LYP, both triplet and quintet states are considered for even n, and the quintet for odd n.
[b] Not practical as $^{BS} < S^2 >$ exceeds 2.

The data in Table 6.4 indicate that, at least for the M06-L functional, $2J$ values are not particularly sensitive to improving the 6-31G(d) basis set to 6-311+G(2df,p), which bodes well for the modeling longer SWNTs, where there will be substantially more efficiency associated with using 6-31G(d). Comparing M06-L to B3LYP, it is evident that for even values of n, the increasing deviation of $^{BS} < S^2 >$ from values near 1.0 (see Table 6.3) for B3LYP leads to much larger predicted $2J$ values compared to M06-L. As discussed in more detail below, the M06-L values are in better quantitative agreement with CASPT2. It is not obvious whether one should ascribe the larger values

of $^{BS} < S^2 >$ for B3LYP to spin contamination, associated with the greater sensitivity of a hybrid functional to this phenomenon compared to a local one, or to a legitimate switch to a reference state of higher spin. As Table 6.4 indicates, computation of $2J$ values using a high-spin quintet as reference does not lead to improved results in the smaller cyclacenes, but improvements do begin to appear in the larger ones.

The broken-symmetry character of the singlet wave functions in the cyclacenes is in any case indicative of spin localization with weak coupling. To better understand this phenomenon, it is instructive to consider the computed frontier molecular orbitals (MOs). In figure 6.2, the highest occupied α and β MOs are illustrated for [8]-cyclacene (these orbitals also serve as the lowest unoccupied molecular orbitals (LUMOs) for the other spin). Each MO is constructed primarily from the 2p orbitals of the hydrogen-bearing carbon atoms that contribute to the SWNT π system. The phases of the 2p orbitals alternate as one proceeds around the torus, and in each case the BS MO has large amplitude on one edge and small amplitude on the other. The α and β MOs differ in the relative phases of the small amplitude component compared to the large one. Thus, in the α MO, the two edges are in phase with one another, while in the β MO, the two edges are out of phase. Thus, the α and β MOs may themselves be viewed as linear combinations of the canonical π orbitals that would be formed from in-phase and out-of-phase combinations of the two edges with equal amplitudes. In the case of the α MO, the weight of the in-phase combination is somewhat larger, and the converse is true for the β MO. Such behavior is expected if the two canonical p orbitals in question

Figure 6.2: Highest occupied α (left) and β (right) orbitals of [8]-cyclacene at the BS M06-L/6-31G(d) level.

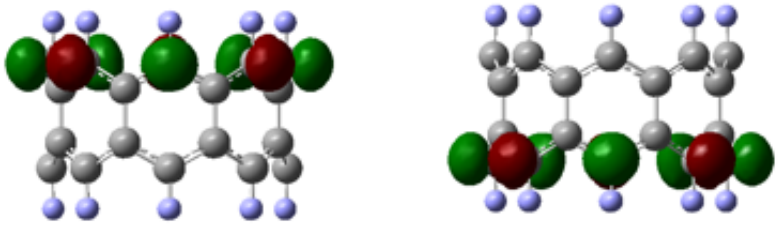

represent the HOMO and LUMO from a restricted calculation with a narrow energy separation, as proves to be the case in all of the even n cyclacenes. The importance of the even character of n is that it permits alternation of the 2p orbital phases to satisfy the cyclic boundary condition.

When n is odd, on the other hand, in addition to the frontier energy separation itself being narrow, the canonical HOMO and LUMO orbitals are each doubly degenerate (in analogy to the π_2 and π_3 orbitals of cyclopropenium, for example). Thus, as illustrated in Figure 6.3, spin localizes left/right in addition to edge/edge. The orbital pictures in Figures 6.2 and 6.3 thus rationalize the triplet and quintet choices for the high-spin reference states in computing $2J$ for even and odd n cyclacenes, respectively, and suggest that using the quintet reference for even n with B3LYP is not really physically justified, in spite of the higher spin contamination of the BS KS determinant.

To further clarify these issues, we also carried out CASPT2 calculations on the cyclacenes, and the results are presented in Table 6.5 comparing predicted triplet (even n) and triplet and quintet (odd n) state energy splittings from BS DFT to those computed

Figure 6.3: Degenerate pairs of highest occupied α (left) and β (right) orbitals of [9]-cyclacene at the BS M06-L/6-31G(d) level.

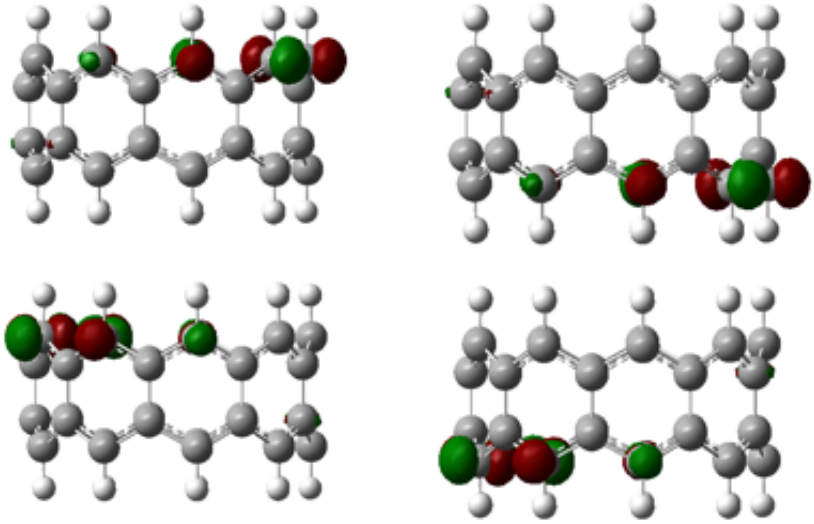

in a more rigorous fashion at the CASPT2 level.

Several trends are worthy of note. First, for n even, there is fairly good agreement between CASPT2 and M06-L for the predicted singlet-triplet splittings; the mean unsigned deviation over n = 6, 8, 10, and 12 is 7 kJ/mol. For n odd, on the other hand, M06-L consistently underestimates the CASPT2 result by 10–18 kJ/mol. As expected, then, the predicted quintet energies are underestimated by roughly triple this amount. The B3LYP results, by contrast, are consistently larger for the state-energy splittings than are those from M06-L. While these results overestimate the CASPT2 results for n even, they come closer to the CASPT2 results than does M06-L for n odd.

The DFT levels predict a steady decrease in the energy of the triplet state relative to the singlet state in both the odd and even n series with increasing n. This trend is

Table 6.5: Predicted state energies (kJ/mol) relative to the singlet ground state for the [n]-cyclacenes.[a]

n	State	M06-L	B3LYP	CASPT2
6	$^3B_{1u}$	51.5	66.8	50.2
7	$^3B_2$	32.2	41.3	50.2
	$^5A_1$	97.1	123.9	172.8
8	$^3B_{1u}$	54.8	91.4	60.7
9	$^3B_2$	19.2	29.0	33.5
	$^5A_1$	57.3	87.0	94.6
10	$^3B_{1u}$	56.9	229.1	47.7
11	$^3B_2$	15.9	27.9	
	$^5A_1$	47.7	83.8	77.5
12	$^3B_{1u}$	46.0	[c]	57.6

[a] The ground state is $^1A_{1g}$ for even n and $^1A_1$ for odd n.
[b] Triplet and quintet energies computed as $2J$ and $6J$, respectively, from eq. 6.3 with the high-spin reference state taken as the triplet for even n and the quintet for odd n unless otherwise indicated. DFT calculations use the 6-31G(d) basis set.
[c] Not practical as $^{BS} < S^2 >$ exceeds 2.

reproduced at the CASPT2 level for odd n, but for even n the splitting for $n = 12$ is predicted to be larger than that for $n = 10$. We speculate, however, that the active space employed for the $n = 12$ calculation may no longer be adequate given the size of the cyclacene. The ideal active space, of course, would be the complete set of π orbitals, but such a calculation vastly exceeds practical limits (as such, the cyclacenes would be interesting test cases for the newly developed RASPT2 model [211], which allows for larger active spaces by reducing the number of allowed excitations within the space, but such testing is beyond the scope of the present work). The cyclacenes thus show behavior similar to the linear polyacenes, where decreasing singlet-triplet splittings have been predicted with increasing length [172].

As one additional means of quantifying the di- or polyradical character of the cyclacenes, we consider the occupation numbers of the orbitals included in the various CAS spaces. In the (8,10) spaces for n even, the occupation numbers of orbital 4 drop from 1.54 for $n = 6$ to 1.41 for $n = 12$, while those for orbital 5 increase from 0.45 to 0.59. In the (12,12) spaces for n odd, the occupation numbers of orbitals 5 and 6 drop from 1.74 and 1.46, respectively, for $n = 7$, to 1.56 and 1.45 for $n = 11$, while those for orbitals 7 and 8 increase from 0.54 and 0.26, respectively, to 0.54 and 0.42. This behavior is consistent with the quintet contamination observed at the BS DFT level and the orbital behavior shown in Figure 3.

6.3.3 Single-walled carbon nanotubes

For the cases of $n = 8$ and 9, we examined the trends in state-energy splittings as the cyclacene was extended to generate short, hydrogen-capped SWNTs, which would be termed (8,0) and (9,0) zig-zag SWNTs (Figure 6.6). We identify the length of these tubes with the integer Λ where $\Lambda = 1$ for a cyclacene. In Table 6.7 we list the singlet-triplet splittings ($E_T - E_S$) computed as $2J$ with J coming from eq. 6.3 at the M06-L/6-31G(d) level as a function of Λ. We also list the HOMO–LUMO gaps predicted at the BS M06-L level.

Using eq. 6.3 to predict singlet-triplet splittings leads to some ambiguity, at least in the case of $n = 8$, given that it is not obvious what spin to choose for the high spin reference. As $^{BS} < S^2 >$ continues to increase with increasing length Λ, it becomes a

Table 6.6: End-on and side-on views of singlet Λ-(8,0)-SWNT for the case of Λ=6.

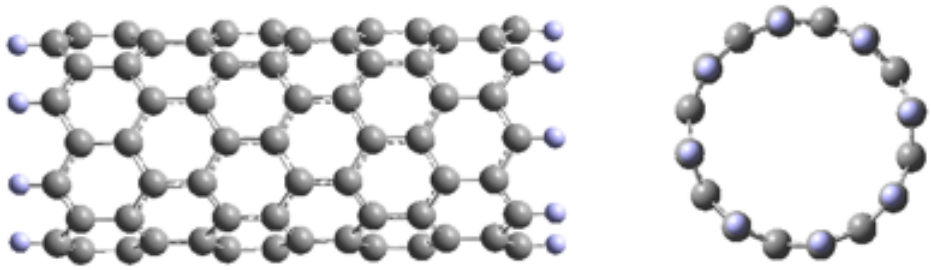

Table 6.7: Λ-(n,0)-SWNT properties predicted at M06-L/6-31G(d) level.[a]

n	Λ	$^{BS}<S^2>$	$^{HS}<S^2>$	$E_T - E_S$	$E_{LUMO} - E_{HOMO}$
8	1	0.88	2.00	54.8	98.7
	2	1.56	6.00	47.7	94.6
	3	1.97	6.00	33.9	95.4
	4	2.46	12.00	28.5	90.4
	5	2.85	12.00	5.9	82.8
	6	3.09	12.00	3.3	78.7
9	1	2.11	6.00	19.2	108.4
	2	2.35	6.00	10.5	104.2
	3	2.40	6.00	6.7	102.9
	4	2.43	6.00	4.6	102.5
	5	2.46	6.00	2.3	102.1
	6	2.49	6.00	1.9	102.0

[a] Expectation values of S^2 are unitless, energy separations are in kJ/mol.

matter of judgment. Of course, if the energy separation between the BS and HS states becomes small, as occurs with increasing Λ in both cases above, the impact of this choice in eq. 6.3 is fairly small.

There is a good convergence in the HOMO–LUMO separations in the (8,0) and (9,0) tubes with increasing Λ, with limiting values of roughly 75 and 100 kJ/mol being

predicted. Considering a different propagating unit than a cyclacene, namely a Clar sextet, Baldoni et al. predicted HOMO–LUMO separations of 169 and 121 kJ/mol for 6-(8,0) and 6-(9,0) tubes, respectively, but these values were not yet well converged based on comparisons to Λ=5 (the use of the Clar sextet causes the growing tubes to have raked edges, as opposed to cyclacene-like edges, so direct comparison of the two values may not be entirely warranted; in addition, it appears that the Baldoni et al. results are taken from restricted singlet calculations, as opposed to BS ones). On the other hand, Barone et al. [159] predict the first optical transition of an infinite length (8,0) nanotube to occur at about 150 kJ/mol (using the TPSSh functional) and suggest that band gaps and optical transitions should be quantitatively similar in SWNTs. However, Wang et al. [160] have also computed the (8,0) band gap for an infinite SWNT and predict a value of 61.7 kJ/mol with the VSXC functional, which is closer to our converging M06-L value. The sensitivity of SWNT band gaps to choice of functional has been noted previously [159] and merits further attention as it is likely to influence studies of reactivity as well.

Irrespective of band gap, the singlet-triplet energy separation (or, put differently, $2J$) in both the (8,0) and (9,0) nanotubes is predicted to approach zero with increasing length. Thus, one might expect a potential for considerable radical character in the reactivity of (n,0) nanotubes with increasing length. As such, zig-zag nanotubes may be particularly susceptible to oxidation by molecular oxygen, whether in the singlet or triplet states, and future studies assessing reaction paths using BS DFT should provide

more insight into this issue.

6.4 Conclusions

Modeling studies based on a combination of density functional and multiconfigurational wave function theories indicate an increase in diradical and eventually polyradical character in [n]-cyclacenes with increasing n. This character also increases as the cyclacenes are extended to form finite-length (n,0) single-walled nanotubes. Broken-symmetry DFT can account for this character in size ranges where multireference wave function theory becomes impractical and may provide an efficient means for modeling the reactions of such finite length nanotubes with other molecules, e.g., molecular oxygen.

References

[1] Blake D. Key, Robert D. Howell, and Craig S. Criddle. Fluorinated organics in the biosphere. *Environmental Science & Technology*, 31(9):2445–2454, 1997.

[2] Eva C. Voldner and Yi-Fan Li. Global usage of selected persistent organochlorines. *Science of The Total Environment*, 160-161(0):201–210, 1995.

[3] Cynthia A de Wit. An overview of brominated flame retardants in the environment. *Chemosphere*, 46(5):583–624, l 2002.

[4] Alasdair H. Neilson and Ann-Sofie Allard. Degradation and transformation of organic fluorine compounds. In A.H. Neilson, editor, *Organofluorines*, volume 3N of *The Handbook of Environmental Chemistry*, pages 137–202. Springer Berlin Heidelberg, 2002.

[5] D. E. C. Adams and R. U. Halden. *Fluorinated Chemicals and the Impacts of Anthropogenic Use*, chapter 29, pages 539–560.

[6] David O'Hagan. Fluorine in health care: Organofluorine containing blockbuster drugs. *Journal of Fluorine Chemistry*, 131(11):1071–1081, 2010.

[7] Knut Breivik, Andy Sweetman, Jozef M. Pacyna, and Kevin C. Jones. Towards a global historical emission inventory for selected pcb congeners – a mass balance approach: 3. an update. *Science of The Total Environment*, 377(2—3):296–307, 2007.

[8] Rainer Lohmann, Knut Breivik, Jordi Dachs, and Derek Muir. Global fate of pops: Current and future research directions. *Environmental Pollution*, 150(1):150–165, 2007.

[9] Linda S Birnbaum and Daniele F Staskal. Brominated flame retardants: cause for concern? *Environmental health perspectives*, 112(1):9, 2004.

[10] G.T. Yogui and J.L. Sericano. Polybrominated diphenyl ether flame retardants in the u.s. marine environment: A review. *Environment International*, 35(3):655–666, 2009.

[11] Adrian Covaci, Stuart Harrad, Mohamed A-E Abdallah, Nadeem Ali, Robin J Law, Dorte Herzke, and Cynthia A de Wit. Novel brominated flame retardants: a review of their analysis, environmental fate and behaviour. *Environment International*, 37(2):532–556, 2011.

[12] Cynthia A de Wit, Amelie Kierkegaard, Niklas Ricklund, and Ulla Sellström. Emerging brominated flame retardants in the environment. In *Brominated Flame Retardants*, pages 241–286. Springer, 2011.

[13] Yan Lin, Xinghua Qiu, Yifan Zhao, Jin Ma, Qiaoyun Yang, and Tong Zhu. Polybromobenzene pollutants in the atmosphere of north china: Levels, distribution, and sources. *Environmental Science & Technology*, 47(22):12761–12767, 2014/07/10 2013.

[14] YG Adewuyi. Sonochemistry: Environmental science and engineering applications. *Industrial & Engineering Chemistry Research*, 40(22):4681–4715, 2001.

[15] RR Bumb, WB Crummett, SS Cutie, Gledhill, RH Hummel, RO Kagel, LL Lamparski, EV Luoma, DL Miller, TJ Nestrick, LA Shadoff, RH Stehl, and JS Woods. Trace chemistries of fire: a source of chlorinated dioxins. *Science*, 210(4468):385–390, 1980.

[16] H Bockhorn, A Hornung, U Hornung, P Jakobströer, and M Kraus. Dehydrochlorination of plastic mixtures. *Journal of Analytical and Applied Pyrolysis*, 49(1-2):97–106, 1999.

[17] M. Blazso, Z. Czégény, and C. Csoma. Pyrolysis and debromination of flame retarded polymers of electronic scrap studied by analytical pyrolysis. *Journal of Analytical and Applied Pyrolysis*, 64(2):249–261, 2002.

[18] MP Luda, N. Euringer, U. Moratti, and M. Zanetti. WEEE recycling: pyrolysis of fire retardant model polymers. *Waste Management*, 25(2):203–208, 2005.

[19] Christian Petrier, Yi Jiang, and Marie-Françoise Lamy. Ultrasound and environment: Sonochemical destruction of chloroaromatic derivatives. *Environmental Science & Technology*, 32(9):1316–1318, 1998.

[20] Yi Jiang, Christian Pétrier, and T David Waite. Kinetics and mechanisms of ultrasonic degradation of volatile chlorinated aromatics in aqueous solutions. *Ultrasonics Sonochemistry*, 9(6):317–323, 2002.

[21] D. Drijvers, H. Van Langenhove, and V. Herrygers. Sonolysis of fluoro-, chloro-, bromo- and iodobenzene: a comparative study. *Ultrasonics Sonochemistry*, 7(2):87–95, 2000.

[22] S.W. Benson. *Thermochemical Kinetics*. Wiley-Interscience, New York, 2nd edition, 1976.

[23] Stephen J. Blanksby and G. Barney Ellison. Bond dissociation energies of organic molecules. *Accounts of Chemical Research*, 36(4):255–263, 2003.

[24] D. Jan. Thermodynamic considerations for dehalogenation. *Dehalogenation*, pages 89–114, 2004.

[25] S. C. Kao and Marcetta Y. Darensbourg. Relative reactivities of anionic transition metal hydrides. reduction of alkyl halides. *Organometallics*, 3(4):646–647, 1984.

[26] C. Carfagna, A. Musco, R. Pontellini, and G. Terzoni. MgH2 as a reducing agent in the presence of transition metal halides: Part I. reduction of organic halides. *Journal of Molecular Catalysis*, 57(1):23–28, 1989.

[27] Yuji Ukisu and Tatsuo Miyadera. Hydrogen-transfer hydrodehalogenation of aromatic halides with alcohols in the presence of noble metal catalysts. *Journal of Molecular Catalysis A: Chemical*, 125(2-3):135–142, 1997.

[28] Mihai S. Viciu, Gabriela A. Grasa, and Steven P. Nolan. Catalytic dehalogenation of aryl halides mediated by a palladium/imidazolium salt system. *Organometallics*, 20(16):3607–3612, 2001.

[29] Stuart A. MacGregor, David McKay, Julien A. Panetier, and Michael K. Whittlesey. Computational study of the hydrodefluorination of fluoroarenes at [Ru(NHC)(PR_3)$_2$(CO)(H_2)]: predicted scope and regioselectivities. *Dalton Trans.*, 42:7386–7395, 2013.

[30] H Lenke and H J Knackmuss. Initial hydrogenation during catabolism of picric acid by rhodococcus erythropolis hl 24-2. *Applied and Environmental Microbiology*, 58(9):2933–2937, 1992.

[31] E Duque, A Haidour, F Godoy, and J L Ramos. Construction of a pseudomonas hybrid strain that mineralizes 2,4,6-trinitrotoluene. *Journal of Bacteriology*, 175(8):2278–2283, 1993.

[32] C Vorbeck, H Lenke, P Fischer, and H J Knackmuss. Identification of a hydride-meisenheimer complex as a metabolite of 2,4,6-trinitrotoluene by a mycobacterium strain. *Journal of Bacteriology*, 176(3):932–934, 1994.

[33] Bradley M. Kraft, Rene J. Lachicotte, and William D. Jones. Aliphatic and aromatic carbon-fluorine bond activation with $Cp^{\star}_{2}ZrH_{2}$: Mechanisms of hydrodefluorination. *Journal of the American Chemical Society*, 123(44):10973–10979, 2001.

[34] Francisco Alonso, Irina P Beletskaya, and Miguel Yus. Metal-mediated reductive hydrodehalogenation of organic halides. *Chemical reviews*, 102(11):4009–4092, 2002.

[35] Hugo Torrens. Carbonfluorine bond activation by platinum group metal complexes. *Coordination chemistry reviews*, 249(17):1957–1985, 2005.

[36] Rebekka Baumgartner and Kristopher McNeill. Hydrodefluorination and hydrogenation of fluorobenzene under mild aqueous conditions. *Environmental Science & Technology*, 46(18):10199–10205, 2012.

[37] Rebekka Baumgartner, Greta K. Stieger, and Kristopher McNeill. Complete hydrodehalogenation of polyfluorinated and other polyhalogenated benzenes under mild catalytic conditions. *Environmental Science & Technology*, 47(12):6545–6553, 2013.

[38] Peter P Fu, Linda S Von Tungeln, Li-Hsueh Chiu, and Zang Yuan Own. Halogenated-polycyclic aromatic hydrocarbons: A class of genotoxic environmental pollutants. *Journal of Environmental Science & Health Part C*, 17(2):71–109, 1999.

[39] Hongtao Yu. Environmental carcinogenic polycyclic aromatic hydrocarbons: photochemistry and phototoxicity. *Journal of Environmental Science and Health, Part C*, 20(2):149–183, 2002.

[40] Yuichi Horii, Gon Ok, Takeshi Ohura, and Kurunthachalam Kannan. Occurrence and profiles of chlorinated and brominated polycyclic aromatic hydrocarbons in waste incinerators. *Environmental Science & Technology*, 42(6):1904–1909, 2008.

[41] Takeshi Ohura, Kei-ichi Sawada, Takashi Amagai, and Miho Shinomiya. Discovery of novel halogenated polycyclic aromatic hydrocarbons in urban particulate matters: Occurrence, photostability, and ahr activity. *Environmental Science & Technology*, 43(7):2269–2275, 2009.

[42] Jing Ma, Yuichi Horii, Jinping Cheng, Wenhua Wang, Qian Wu, Takeshi Ohura, and Kurunthachalam Kannan. Chlorinated and parent polycyclic aromatic hydrocarbons in environmental samples from an electronic waste recycling facility and a chemical industrial complex in china. *Environmental Science & Technology*, 43(3):643–649, 2014/07/22 2009.

[43] František Karlický, Kasibhatta Kumara Ramanatha Datta, Michal Otyepka, and Radek Zbořil. Halogenated graphenes: Rapidly growing family of graphene derivatives. *ACS Nano*, 7(8):6434–6464, 2013.

[44] Wei Zhe Teo, Elaine Lay Khim Chng, Zdenek Sofer, and Martin Pumera. Cytotoxicity of halogenated graphenes. *Nanoscale*, 6:1173–1180, 2014.

[45] R Atkinson, DL Baulch, RA Cox, RF Hampson Jr, JA Kerr, and J Troe. Evaluated kinetic and photochemical data for atmospheric chemistry. *Journal of Physical and Chemical Reference Data*, 21(6), 2010.

[46] James A Miller, Robert J Kee, and Charles K Westbrook. Chemical kinetics and combustion modeling. *Annual Review of Physical Chemistry*, 41(1):345–387, 1990.

[47] Jan Dolfing and B. Keith Harrison. Gibbs free energy of formation of halogenated aromatic compounds and their potential role as electron acceptors in anaerobic environments. *Environmental Science & Technology*, 26(11):2213–2218, 1992.

[48] Hauke Smidt and Willem M de Vos. Anaerobic microbial dehalogenation. *Annu. Rev. Microbiol.*, 58:43–73, 2004.

[49] Yan Zhao and Donald G. Truhlar. The M06 suite of density functionals for main group thermochemistry, thermochemical kinetics, noncovalent interactions, excited states, and transition elements: two new functionals and systematic testing of four

m06-class functionals and 12 other functionals. *Theoretical Chemistry Accounts*, 120:215–241, 2008.

[50] Yan Zhao and Donald G. Truhlar. Density functionals with broad applicability in chemistry. *Accounts of Chemical Research*, 41(2):157–167, 2008.

[51] Yan Zhao and Donald G. Truhlar. Density functional theory for reaction energies: Test of meta and hybrid meta functionals, range-separated functionals, and other high-performance functionals. *Journal of Chemical Theory and Computation*, 7(3):669–676, 2011.

[52] Bun Chan and Leo Radom. Hierarchy of relative bond dissociation enthalpies and their use to efficiently compute accurate absolute bond dissociation enthalpies for C–H, C–C, and C–F bonds. *The Journal of Physical Chemistry A*, 117(17):3666–3675, 2013.

[53] Jennifer J. Guerard and J. Samuel Arey. Critical evaluation of implicit solvent models for predicting aqueous oxidation potentials of neutral organic compounds. *Journal of Chemical Theory and Computation*, 9(11):5046–5058, 2013.

[54] I. M. Alecu, Jingjing Zheng, Yan Zhao, and Donald G. Truhlar. Computational thermochemistry: Scale factor databases and scale factors for vibrational frequencies obtained from electronic model chemistries. *Journal of Chemical Theory and Computation*, 6(9):2872–2887, 2010.

[55] K.K. Irikura. Thermo.pl. National Institute of Standards and Technology, 2002.

[56] Aleksandr V. Marenich, Christopher J. Cramer, and Donald G. Truhlar. Universal solvation model based on solute electron density and on a continuum model of the solvent defined by the bulk dielectric constant and atomic surface tensions. *The Journal of Physical Chemistry B*, 113(18):6378–6396, 2009.

[57] Krishnan Raghavachari, Gary W. Trucks, John A. Pople, and Martin Head-Gordon. A fifth-order perturbation comparison of electron correlation theories. *Chemical Physics Letters*, 157(6):479–483, 1989.

[58] Marvin Douglas and Norman M Kroll. Quantum electrodynamical corrections to the fine structure of helium. *Annals of Physics*, 82(1):89–155, 1974.

[59] Bernd A. Hess. Relativistic electronic-structure calculations employing a two-component no-pair formalism with external-field projection operators. *Phys. Rev. A*, 33:3742–3748, Jun 1986.

[60] Georg Jansen and Bernd A. Hess. Revision of the douglas-kroll transformation. *Phys. Rev. A*, 39:6016–6017, Jun 1989.

[61] Wibe A De Jong, Robert J Harrison, and David A Dixon. Parallel douglas–kroll energy and gradients in nwchem: estimating scalar relativistic effects using douglas–kroll contracted basis sets. *The Journal of Chemical Physics*, 114:48, 2001.

[62] M. J. Frisch, G. W. Trucks, H. B. Schlegel, G. E. Scuseria, M. A. Robb, J. R. Cheeseman, G. Scalmani, V. Barone, B. Mennucci, G. A. Petersson, H. Nakatsuji, M. Caricato, X. Li, H. P. Hratchian, A. F. Izmaylov, J. Bloino, G. Zheng, J. L. Sonnenberg, M. Hada, M. Ehara, K. Toyota, R. Fukuda, J. Hasegawa, M. Ishida, T. Nakajima, Y. Honda, O. Kitao, H. Nakai, T. Vreven, J. A. Montgomery, Jr., J. E. Peralta, F. Ogliaro, M. Bearpark, J. J. Heyd, E. Brothers, K. N. Kudin, V. N. Staroverov, R. Kobayashi, J. Normand, K. Raghavachari, A. Rendell, J. C. Burant, S. S. Iyengar, J. Tomasi, M. Cossi, N. Rega, J. M. Millam, M. Klene, J. E. Knox, J. B. Cross, V. Bakken, C. Adamo, J. Jaramillo, R. Gomperts, R. E. Stratmann, O. Yazyev, A. J. Austin, R. Cammi, C. Pomelli, J. W. Ochterski, R. L. Martin, K. Morokuma, V. G. Zakrzewski, G. A. Voth, P. Salvador, J. J. Dannenberg, S. Dapprich, A. D. Daniels, Ö. Farkas, J. B. Foresman, J. V. Ortiz, J. Cioslowski, and D. J. Fox. Gaussian 09, revision c.1. Technical report, 2009. Gaussian Inc. Wallingford CT 2009.

[63] R Core Team. *R: A Language and Environment for Statistical Computing*. R Foundation for Statistical Computing, Vienna, Austria, 2012. ISBN 3-900051-07-0.

[64] Steven E. Wheeler, Kendall N. Houk, Paul v. R. Schleyer, and Wesley D. Allen. A hierarchy of homodesmotic reactions for thermochemistry. *Journal of the American Chemical Society*, 131(7):2547–2560, 2009.

[65] M.V. Roux, M. Temprado, J.S. Chickos, and Y. Nagano. Critically evaluated thermochemical properties of polycyclic aromatic hydrocarbons. *J. Phys. Chem. Ref. Data*, 37(4):1855–1996, 2008.

[66] Michael E. Harding, Juana Vazquez, Jurgen Gauss, John F. Stanton, and Mihaly Kallay. Towards highly accurate ab initio thermochemistry of larger systems: Benzene. *The Journal of Chemical Physics*, 135(4):044513, 2011.

[67] William R. Stevens, Branko Ruscic, and Tomas Baer. Heats of formation of $C_6H_5^\star$, $C_6H_5^+$, and C_6H_5NO by threshold photoelectron photoion coincidence and active thermochemical tables analysis. *The Journal of Physical Chemistry A*, 114(50):13134–13145, 2010.

[68] J.L.; Scott D.W.; McCullough J.P. Good, W.D.; Lacina. Combustion calorimetry of organic fluorine compounds. the heats of combustion and formation of the difluorobenzenes, 4-fluorotoluene and m-trifluorotoluic acid. *Journal of Physical Chemistry*, 66:1529–1532, 1962.

[69] J.D. Cox, H.A. Gundry, D. Harrop, and A.J. Head. Thermodynamic properties of fluorine compounds. 9. enthalpies of formation of some compounds containing the pentafluorophenyl group. *J. Chem. Thermodyn.*, 1:77–87, 1969.

[70] A.J. Harrop, D.; Head. Thermodynamic properties of fluorine compounds. 18. enthalpy of combustion of 1,2,4,5-tetrafluorobenzene. *J. Chem. Thermodyn.*, 10(705-706), 1978.

[71] JB Pedley. *Thermochemical data and structures of organic compounds*, volume 1. CRC Press, 1994.

[72] José R.B. Gomes and Manuel A.V. Ribeiro da Silva. Gas-phase enthalpies of formation of the fluorobenzenes family and their dewar isomers from ab initio calculations. *Journal of Molecular Structure: {THEOCHEM}*, 778(1–3):77–84, 2006.

[73] VA Platonov and Yu N Simulin. Standard enthalpies of formation of 1,2,3-trichlorobenzene, 1,2,4,5-tetrachlorobenzene, and hexachlorobenzene. *Russ. J. Phys. Chem.*, 57:840–842, 1983.

[74] VA Platonov and Yu N Simulin. Experimental determination of the standard enthalpies of formation of polychlorobenzenes. II. standard enthalpies of formation of dichlorobenzenes. *Russ. J. Phys. Chem*, 58:1630–1632, 1984.

[75] VA Platonov, Yu N Simulin, and MM Rozenberg. Standard heat of formation of pentachlorobenzene. calculation of δhc (g) and δes (g) of polychlorobenzenes by the Tatevskii method. *Russ. J. Phys. Chem.*, 59:814–817, 1985.

[76] VA Platonov and Yu N Simulin. Experimental determination of standard heats of formation of polychlorobenzenes III. standard heats of formation of mono-, 1, 2, 4-tri-, 1, 3, 5-tri-, 1, 2, 3, 4-tetra-and 1, 2, 3, 5-tetrachlorobenzenes. *Russ. J. Phys. Chem.*, 59:300, 1985.

[77] H. Yan, J. Gu, X. An, and R. Hu. Standard enthalpies of formation and enthlpies of isomerization of trichlorobenzenes. *Huaxue Xuebao*, 45:1184–1187, 1987.

[78] D. Thompson. Enthalpies of formation and entropies of chlorinated dibenzo-p-dioxins and dibenzofurans; selected data for computer-based studies. *Thermochimica Acta*, 261:7–20, 1995.

[79] Luis A. León, Rafael Notario, Jairo Quijano, and Claudia Sánchez. Structures and enthalpies of formation in the gas phase of the most toxic polychlorinated dibenzo-p-dioxins. a DFT study. *The Journal of Physical Chemistry A*, 106(28):6618–6627, 2002.

[80] Jeffrey A. Manion. Evaluated enthalpies of formation of the stable closed shell C1 and C2 chlorinated hydrocarbons. *Journal of Physical and Chemical Reference Data*, 31(1):123–172, 2002.

[81] Larry A. Curtiss, Krishnan Raghavachari, Paul C. Redfern, and John A. Pople. Gaussian-3 theory using scaled energies. *The Journal of Chemical Physics*, 112(3):1125–1132, 2000.

[82] Michael J. Fifolt, Stanley A. Sojka, Roger A. Wolfe, Daniel S. Hojnicki, Joseph F. Bieron, and Frank J. Dinan. A chemical shift additivity method for the prediction of fluorine-19 chemical shifts in fluoroaromatic compounds. *The Journal of Organic Chemistry*, 54(13):3019–3023, 1989.

[83] Branko Ruscic, Reinhardt E. Pinzon, Melita L. Morton, Gregor von Laszevski, Sandra J. Bittner, Sandeep G. Nijsure, Kaizar A. Amin, Michael Minkoff, and Albert F. Wagner. Introduction to active thermochemical tables: Several "key" enthalpies of formation revisited. *The Journal of Physical Chemistry A*, 108(45):9979–9997, 2013/08/22 2004.

[84] Donald Mackay and Wan Ying Shiu. A critical review of henry's law constants for chemicals of environmental interest. *Journal of Physical and Chemical Reference Data*, 10(4):1175–1199, 1981.

[85] J. Peter Guthrie. Use of DFT methods for the calculation of the entropy of gas phase organic molecules: An examination of the quality of results from a simple approach. *The Journal of Physical Chemistry A*, 105(37):8495–8499, 2001.

[86] Mohamad H. Kassaee, David J. Keffer, and William V. Steele. A comparison between entropies of aromatic compounds from quantum mechanical calculations and experiment. *Journal of Molecular Structure: {THEOCHEM}*, 802(1–3):23–34, 2007.

[87] Aleksandr V. Marenich, Christopher J. Cramer, and Donald G. Truhlar. Performance of SM6, SM8, and SMD on the SAMPL1 test set for the prediction of small-molecule solvation free energies. *The Journal of Physical Chemistry B*, 113(14):4538–4543, 2009.

[88] John E. Bartmess. Thermodynamics of the electron and the proton. *The Journal of Physical Chemistry*, 98(25):6420–6424, 1994.

[89] Abdirisak A. Isse and Armando Gennaro. Absolute potential of the standard hydrogen electrode and the problem of interconversion of potentials in different solvents. *The Journal of Physical Chemistry B*, 114(23):7894–7899, 2010.

[90] Michael D. Tissandier, Kenneth A. Cowen, Wan Yong Feng, Ellen Gundlach, Michael H. Cohen, Alan D. Earhart, James V. Coe, and Thomas R. Tuttle. The proton's absolute aqueous enthalpy and gibbs free energy of solvation from cluster-ion solvation data. *The Journal of Physical Chemistry A*, 102(40):7787–7794, 1998.

[91] C. Blondel, P. Cacciani, C. Delsart, and R. Trainham. High-resolution determination of the electron affinity of fluorine and bromine using crossed ion and laser beams. *Phys. Rev. A*, 40:3698–3701, Oct 1989.

[92] R Trainham, G D Fletcher, and D J Larson. One- and two-photon detachment of the negative chlorine ion. *Journal of Physics B: Atomic and Molecular Physics*, 20(23):L777, 1987.

[93] Christophe Blondel, Christian Delsart, and Fabienne Goldfarb. Electron spectrometry at the μeV level and the electron affinities of Si and F. *Journal of Physics B: Atomic, Molecular and Optical Physics*, 34(9):L281–L288, 2001.

[94] D.D.; Medvedev V.A. Cox, J.D.; Wagman. *CODATA Key Values for Thermodynamics*, volume 1. Hemisphere Publishing Corp., New York, 1984.

[95] Casey P. Kelly, Christopher J. Cramer, and Donald G. Truhlar. Aqueous solvation free energies of ions and ion-water clusters based on an accurate value for the absolute aqueous solvation free energy of the proton. *The Journal of Physical Chemistry B*, 110(32):16066–16081, 2006.

[96] Daniel Sadowsky, Kristopher McNeill, and Christopher J. Cramer. Thermochemical factors affecting the dehalogenation of aromatics. *Environmental Science & Technology*, 47(24):14194–14203, 2013.

[97] Jaqueline L. Kiplinger, Thomas G. Richmond, and Carolyn E. Osterberg. Activation of carbon-fluorine bonds by metal complexes bond activation with mechanisms. *Chemical Reviews*, 94(2):373–431, 1994.

[98] M Aresta, P Caramuscio, L De Stefano, and T Pastore. Solid state dehalogenation of pcbs in contaminated soil using $nabh_4$. *Waste Management*, 23(4):315–319, 2003.

[99] Laurent Maron, Evan L. Werkema, Lionel Perrin, Odile Eisenstein, and Richard A. Andersen. Hydrogen for fluorine exchange in C_6F_6 and C_6F_5H by monomeric 1,3,4-$[(Me_3C)_3C_5H_2]_2CeH$: Experimental and computational studies. *Journal of the American Chemical Society*, 127(1):279–292, 2005.

[100] Bettina Schrick, Jennifer L. Blough, A. Daniel Jones, and Thomas E. Mallouk. Hydrodechlorination of trichloroethylene to hydrocarbons using bimetallic nickel–iron nanoparticles. *Chemistry of Materials*, 14(12):5140–5147, 2002.

[101] G. A. Artamkina, M. P. Egorov, and I. P. Beletskaya. Some aspects of anionic sigma-complexes. *Chemical Reviews*, 82(4):427–459, 1982.

[102] V.M. Vlasov. Fluoride ion as a nucleophile and a leaving group in aromatic nucleophilic substitution reactions. *Journal of Fluorine Chemistry*, 61(3):193–216, 1993.

[103] Juan Burdeniuc, Brigitte Jedicka, and Robert H. Crabtree. Recent advances in c–F bond activation. *Chemische Berichte*, 130(2):145–154, 1997.

[104] Hideki Amii and Kenji Uneyama. C–F bond activation in organic synthesis. *Chemical Reviews*, 109(5):2119–2183, 2009.

[105] Ya-Jun Zheng and Rick L. Ornstein. Mechanism of nucleophilic aromatic substitution of 1-chloro-2,4-dinitrobenzene by glutathione in the gas phase and in solution. implications for the mode of action of glutathione S-transferases. *Journal of the American Chemical Society*, 119(4):648–655, 1997.

[106] JD Scholten, KH Chang, PC Babbitt, H Charest, M Sylvestre, and D Dunaway-Mariano. Novel enzymic hydrolytic dehalogenation of a chlorinated aromatic. *Science*, 253(5016):182–185, 1991.

[107] Dingguo Xu, Yanseng Wei, Jingbo Wu, Debra Dunaway-Mariano, Hua Guo, Qiang Cui, and Jiali Gao. QM/MM studies of the enzyme-catalyzed dechlorination of 4-chlorobenzoyl-CoA provide insight into reaction energetics. *Journal of the American Chemical Society*, 126(42):13649–13658, 2004.

[108] Wen Jian Chen, Gerard F Graminski, and Richard N Armstrong. Dissection of the catalytic mechanism of isozyme 4-4 of glutathione S-transferase with alternative substrates. *Biochemistry*, 27(2):647–654, 1988.

[109] Gwen P. Crooks and Shelley D. Copley. A surprising effect of leaving group on the nucleophilic aromatic substitution reaction catalyzed by 4-chlorobenzoyl coa dehalogenase. *Journal of the American Chemical Society*, 115(14):6422–6423, 1993.

[110] Shinichi Yamabe, Tsutomu Minato, and Yumi Kawabata. The importance of the $\sigma^\star$–$\pi^\star$ orbital mixing for the nucleophilic displacement on the unsaturated carbon. *Canadian Journal of Chemistry*, 62(2):235–240, 1984.

[111] Mikhail N. Glukhovtsev, Robert D. Bach, and Sergei Laiter. Single–step and multistep mechanisms of aromatic nucleophilic substitution of halobenzenes and halonitrobenzenes with halide anions: ab initio computational study. *The Journal of Organic Chemistry*, 62(12):4036–4046, 1997.

[112] Israel Fernández, Gernot Frenking, and Einar Uggerud. Rate-determining factors in nucleophilic aromatic substitution reactions. *The Journal of Organic Chemistry*, 75(9):2971–2980, 2010.

[113] Douglas M. Mackay and John A. Cherry. Groundwater contamination: pump-and-treat remediation. *Environmental Science & Technology*, 23(6):630–636, 1989.

[114] R. Thiruvenkatachari, S. Vigneswaran, and R. Naidu. Permeable reactive barrier for groundwater remediation. *Journal of Industrial and Engineering Chemistry*, 14(2):145–156, 3 2008.

[115] Marcus D Hanwell, Donald E Curtis, David C Lonie, Tim Vandermeersch, Eva Zurek, and Geoffrey R Hutchison. Avogadro: an advanced semantic chemical editor, visualization, and analysis platform. *Journal of cheminformatics*, 4(1):1–17, 2012.

[116] R. Bolton and J.P.B. Sandall. Nucleophilic displacement in polyhalogenoaromatic compounds. Part 12. Additivity of fluorine substituent effects in methoxydefluorination. *Journal of Fluorine Chemistry*, 21(4):459–467, 1982.

[117] P.P. Rodionov and G.G. Furin. Kinetics of nucleophilic substitution reactions of polyfluoroaromatic compounds. *Journal of Fluorine Chemistry*, 47(3):361–434, 1990.

[118] Boris Galabov, Valia Nikolova, and Sonia Ilieva. Does the molecular electrostatic potential reflect the effects of substituents in aromatic systems? *Chemistry – A European Journal*, 19(16):5149–5155, 2013.

[119] Richard D. Chambers, Deborah Close, W. Kenneth R. Musgrave, John S. Waterhouse, and D. Lyn H. Williams. Mechanisms for reactions of halogenated compounds. Part 2. Orienting effects of chlorine substituents in nucleophilic aromatic substitution. *J. Chem. Soc., Perkin Trans. 2*, pages 1774–1778, 1977.

[120] E. C. Ashby, W. S. Park, A. B. Goel, and Wei Yang Su. Single electron transfer in reactions of alkyl halides with lithium thiolates. *The Journal of Organic Chemistry*, 50(25):5184–5193, 1985.

[121] Roberto A. Rossi, Adriana B. Pierini, and Alicia B. Peñéñory. Nucleophilic substitution reactions by electron transfer. *Chemical Reviews*, 103(1):71–168, 2002.

[122] J. Burdon. A rationalization of orientation and reactivity in the nucleophilic replacement reactions of aromatic polyhalo-compounds. *Tetrahedron*, 21(12):3373–3380, 1965.

[123] Robert Filler, Nagaraj R. Ayyangar, Wlodzimierz Gustowski, and Hyung H. Kang. New reactions of polyfluoroaromatic compounds. pentafluorophenylalanine and tetrafluorotyrosine. *The Journal of Organic Chemistry*, 34(3):534–538, 1969.

[124] Paul L. Coe, David Oldfield, and John Colin Tatlow. Aromatic polyfluorocompounds. part LVIII. the reaction of n-butyllithium with metnyl-, fluoromethyl-, and difluorometnyl-pentafluorobenzene. *Journal of Fluorine Chemistry*, 29(3):341–347, 1985.

[125] Katherine H. Langford, Sigurd Øxnevad, Merete Schøyen, and Kevin V. Thomas. Do antiparasitic medicines used in aquaculture pose a risk to the norwegian aquatic environment? *Environmental Science & Technology*, 48(14):7774–7780, 2014.

[126] C. Vargas, B. Song, M. Camps, and M. M. Häggblom. Anaerobic degradation of fluorinated aromatic compounds. *Applied Microbiology and Biotechnology*, 53:342–347, 2000.

[127] M.F. Carvalho, C.C.T. Alves, M.I.M. Ferreira, P. De Marco, and P.M.L. Castro. Isolation and initial characterization of a bacterial consortium able to mineralize fluorobenzene. *Applied and Environmental Microbiology*, 68(1):102–105, 2002.

[128] M.F. Carvalho, M.I.M. Ferreira, I.S. Moreira, P.M.L. Castro, and Janssen B. J. Degradation of fluorobenzene by rhizobiales strain F11 via ortho cleavage of 4-fluorocatechol and catechol. *Applied and Environmental Microbiology*, 72:7413–7417, 2006.

[129] M. Angeles Aramendía, Víctor Borau, Isabel M García, César Jiménez, Alberto Marinas, José M Marinas, and Francisco J Urbano. Hydrogenolysis of aryl halides by hydrogen gas and hydrogen transfer over palladium-supported catalysts. *Comptes Rendus de l'Académie des Sciences - Series IIC - Chemistry*, 3(6):465–470, 11 2000.

[130] Pascal P Cellier, Jean-Francis Spindler, Marc Taillefer, and Henri-Jean Cristau.

Pd/C-catalyzed room-temperature hydrodehalogenation of aryl halides with hydrazine hydrochloride. *Tetrahedron Letters*, 44(38):7191–7195, 9 2003.

[131] Katrin Mackenzie, Heike Frenzel, and Frank-Dieter Kopinke. Hydrodehalogenation of halogenated hydrocarbons in water with Pd catalysts: Reaction rates and surface competition. *Applied Catalysis B: Environmental*, 63(3–4):161–167, 3 2006.

[132] Daniel Sadowsky, Kristopher McNeill, and Christopher J. Cramer. Dehalogenation of aromatics by nucleophilic aromatic substitution. *Environmental Science & Technology*, In Review.

[133] C. Adamo and V. Barone. Toward reliable adiabatic connection models free from adjustable parameters. *Chemical Physics Letters*, 274(1-3):242–250, 1997.

[134] Sijie Luo and Donald G. Truhlar. How evenly can approximate density functionals treat the different multiplicities and ionization states of 4d transition metal atoms? *Journal of Chemical Theory and Computation*, 8(11):4112–4126, 2012.

[135] D. Andrae, U. Häußermann, M. Dolg, H. Stoll, and H. Preuß. Energy-adjusted ab initio pseudopotentials for the second and third row transition elements. *Theoretica Chimica Acta*, 77:123–141, 1990.

[136] Pierre Villars and Lauriston D Calvert. *Pearson's handbook of crystallographic data for intermetallic phases*, volume 2. American Society for Metals Metals Park, OH, 1985.

[137] J. Cioslowski. A new population analysis based on atomic polar tensors. *Journal of the American Chemical Society*, 111(22):8333–8336, 1989.

[138] Alain Roucoux, Jürgen Schulz, and Henri Patin. Arene hydrogenation with a stabilised aqueous rhodium(0) suspension: A major effect of the surfactant counteranion. *Advanced Synthesis & Catalysis*, 345(1-2):222–229, 2003.

[139] Shouzhong Zou, Christopher T. Williams, Eddy K.-Y. Chen, and Michael J. Weaver. Surface-enhanced raman scattering as a ubiquitous vibrational probe of transition-metal interfaces: Benzene and related chemisorbates on palladium and rhodium in aqueous solution. *The Journal of Physical Chemistry B*, 102(45):9039–9049, 1998.

[140] E. Bright Wilson. The normal modes and frequencies of vibration of the regular plane hexagon model of the benzene molecule. *Phys. Rev.*, 45:706–714, May 1934.

[141] David B Warheit, BR Laurence, Kenneth L Reed, DH Roach, GAM Reynolds, and TR Webb. Comparative pulmonary toxicity assessment of single-wall carbon nanotubes in rats. *Toxicological Sciences*, 77(1):117–125, 2004.

[142] Guang Jia, Haifang Wang, Lei Yan, Xiang Wang, Rongjuan Pei, Tao Yan, Yuliang Zhao, and Xinbiao Guo. Cytotoxicity of carbon nanomaterials: Single-wall nanotube, multi-wall nanotube, and fullerene. *Environmental Science & Technology*, 39(5):1378–1383, 2005.

[143] David B Warheit. What is currently known about the health risks related to carbon nanotube exposures? *Carbon*, 44(6):1064–1069, 2006. Toxicology of Carbon Nanomaterials.

[144] Hoon Hyung, John D. Fortner, Joseph B. Hughes, and Jae-Hong Kim. Natural organic matter stabilizes carbon nanotubes in the aqueous phase. *Environmental Science & Technology*, 41(1):179–184, 2007.

[145] RP Schwarzenbach, PM Gschwend, and DM Imboden. *Environmental Organic Chemistry*. John Wiley, 1993.

[146] Hyun-Hee Cho, Billy A. Smith, Joshua D. Wnuk, D. Howard Fairbrother, and William P. Ball. Influence of surface oxides on the adsorption of naphthalene onto multiwalled carbon nanotubes. *Environmental Science & Technology*, 42(8):2899–2905, 2008.

[147] Bo Pan and Baoshan Xing. Adsorption mechanisms of organic chemicals on carbon nanotubes. *Environmental Science & Technology*, 42(24):9005–9013, 2008.

[148] T Savage, S Bhattacharya, B Sadanadan, J Gaillard, T M Tritt, Y-P Sun, Y Wu, S Nayak, R Car, N Marzari, P M Ajayan, and A M Rao. Photoinduced oxidation of carbon nanotubes. *Journal of Physics: Condensed Matter*, 15(35):5915, 2003.

[149] Gordana Dukovic, Brian E. White, Zhiyong Zhou, Feng Wang, Steffen Jockusch, Michael L. Steigerwald, Tony F. Heinz, Richard A. Friesner, Nicholas J. Turro, and

Louis E. Brus. Reversible surface oxidation and efficient luminescence quenching in semiconductor single-wall carbon nanotubes. *Journal of the American Chemical Society*, 126(46):15269–15276, 2014/07/09 2004.

[150] Mark A. Hamon, Kristina L. Stensaas, Miles A. Sugar, Katherine C. Tumminello, and Anna K. Allred. Reacting soluble single-walled carbon nanotubes with singlet oxygen. *Chemical Physics Letters*, 447(1–3):1–4, 10 2007.

[151] Siu-Pang Chan, Gang Chen, X. G. Gong, and Zhi-Feng Liu. Oxidation of carbon nanotubes by singlet O_2. *Phys. Rev. Lett.*, 90:086403, Feb 2003.

[152] George E. Froudakis, Melanie Schnell, Max Mühlhäuser, Sigrid D. Peyerimhoff, Antonis N. Andriotis, Madhu Menon, and R. Michael Sheetz. Pathways for oxygen adsorption on single-wall carbon nanotubes. *Phys. Rev. B*, 68:115435, Sep 2003.

[153] M. Grujicic, G. Cao, A. M. Rao, T. M. Tritt, and S. Nayak. UV-light enhanced oxidation of carbon nanotubes. *Applied Surface Science*, 214(1–4):289–303, 5 2003.

[154] Alessandra Ricca, Charles W. Bauschlicher, and Amitesh Maiti. Comparison of the reactivity of O_2 with a (10,0) and a (9,0) carbon nanotube. *Phys. Rev. B*, 68:035433, Jul 2003.

[155] Yong-fan Zhang and Zhi-feng Liu. Oxidation of zigzag carbon nanotubes by singlet O_2: Dependence on the tube diameter and the electronic structure. *The Journal of Physical Chemistry B*, 108(31):11435–11441, 2004.

[156] Bin Fan, Roland Hany, Jacques-Edouard Moser, and Frank Nüesch. Enhanced cyanine solar cell performance upon oxygen doping. *Organic Electronics*, 9(1):85–94, 2 2008.

[157] Philippe Lambin. Electronic structure of carbon nanotubes. *Comptes Rendus Physique*, 4(9):1009–1019, 11 2003.

[158] G. Y. Guo, K. C. Chu, Ding-sheng Wang, and Chun-gang Duan. Linear and nonlinear optical properties of carbon nanotubes from first-principles calculations. *Phys. Rev. B*, 69:205416, May 2004.

[159] Verónica Barone, Juan E. Peralta, Michael Wert, Jochen Heyd, and Gustavo E. Scuseria. Density functional theory study of optical transitions in semiconducting single-walled carbon nanotubes. *Nano Letters*, 5(8):1621–1624, 2005.

[160] Houng-Wei Wang, Bo-Cheng Wang, Wen-Hao Chen, and Michitoshi Hayashi. Localized gaussian type orbital-periodic boundary condition-density functional theory study of infinite-length single-walled carbon nanotubes with various tubular diameters. *The Journal of Physical Chemistry A*, 112(8):1783–1790, 2008.

[161] Christopher J Cramer and Donald G Truhlar. Implicit solvation models: equilibria, structure, spectra, and dynamics. *Chemical Reviews*, 99(8):2161–2200, 1999.

[162] Jacopo Tomasi, Benedetta Mennucci, and Roberto Cammi. Quantum mechanical continuum solvation models. *Chemical reviews*, 105(8):2999–3094, 2005.

[163] Hongbo Zhao and Sumit Mazumdar. Electron-electron interaction effects on the optical excitations of semiconducting single-walled carbon nanotubes. *Phys. Rev. Lett.*, 93:157402, Oct 2004.

[164] Sergei Tretiak. Triplet state absorption in carbon nanotubes: A TD-DFT study. *Nano Letters*, 7(8):2201–2206, 2007.

[165] M. Baldoni, A. Sgamellotti, and F. Mercuri. Finite-length models of carbon nanotubes based on clar sextet theory. *Organic Letters*, 9(21):4267–4270, 2007.

[166] Alain Rochefort, Phaedon Avouris, Frédéric Lesage, and Dennis R. Salahub. Electrical and mechanical properties of distorted carbon nanotubes. *Phys. Rev. B*, 60:13824–13830, Nov 1999.

[167] Holger F. Bettinger. Effects of finite carbon nanotube length on sidewall addition of fluorine atom and methylene. *Organic Letters*, 6(5):731–734, 2014/07/10 2004.

[168] Christopher J Cramer. *Essentials of computational chemistry: theories and models*. John Wiley & Sons, 2013.

[169] Henryk A. Witek and Keiji Morokuma. Systematic study of vibrational frequencies calculated with the self-consistent charge density functional tight-binding method. *Journal of Computational Chemistry*, 25(15):1858–1864, 2004.

[170] Guishan Zheng, Stephan Irle, and Keiji Morokuma. Performance of the DFTB method in comparison to DFT and semiempirical methods for geometries and

energies of C_{20}–C_{86} fullerene isomers. *Chemical Physics Letters*, 412(1–3):210–216, 8 2005.

[171] Zhongfang Chen, De-en Jiang, Xin Lu, Holger F. Bettinger, Sheng Dai, Paul von Ragué Schleyer, and Kendall N. Houk. Open-shell singlet character of cyclacenes and short zigzag nanotubes. *Organic Letters*, 9(26):5449–5452, 2007.

[172] Johannes Hachmann, Jonathan J Dorando, Michael Avilés, and Garnet Kin-Lic Chan. The radical character of the acenes: A density matrix renormalization group study. *The Journal of chemical physics*, 127(13):134309, 2007.

[173] Yan Zhao and Donald G. Truhlar. A new local density functional for main-group thermochemistry, transition metal bonding, thermochemical kinetics, and noncovalent interactions. *The Journal of Chemical Physics*, 125(19):194101, 2006.

[174] Warren J Hehre, Leo Radom, Paul von R Schleyer, John A Pople, et al. *Ab initio molecular orbital theory*, volume 67. Wiley New York, 1986.

[175] B. I. Dunlap, J. W. D. Connolly, and J. R. Sabin. On some approximations in applications of Xα theory. *The Journal of Chemical Physics*, 71(8):3396–3402, 1979.

[176] O. Vahtras, J. Almlöf, and M. W. Feyereisen. Integral approximations for lcao-scf calculations. *Chemical Physics Letters*, 213(5–6):514–518, 10 1993.

[177] Marek Sierka, Annika Hogekamp, and Reinhart Ahlrichs. Fast evaluation of the coulomb potential for electron densities using multipole accelerated resolution of identity approximation. *The Journal of Chemical Physics*, 118(20):9136–9148, 2003.

[178] Robert Polly, Hans-Joachim Werner, Frederick R Manby, and Peter J Knowles. Fast hartree–fock theory using local density fitting approximations. *Molecular Physics*, 102(21–22):2311–2321, 2004.

[179] W. Heisenberg. Zur theorie des ferromagnetismus. 49(9-10):619–636, 1928.

[180] Paul Adrien Maurice Dirac. Quantum mechanics of many-electron systems. *Proc. R. Soc. London, Ser. A*, pages 714–733, 1929.

[181] JH Van Vleck. A survey of the theory of ferromagnetism. *Reviews of Modern Physics*, 17(1):27, 1945.

[182] J. C. Slater. Ferromagnetism and the band theory. *Rev. Mod. Phys.*, 25:199–210, Jan 1953.

[183] Louis Noodleman and Ernest R. Davidson. Ligand spin polarization and antiferromagnetic coupling in transition metal dimers. *Chemical Physics*, 109(1):131–143, 11 1986.

[184] Ernest R. Davidson and Aurora E. Clark. Spin polarization and annihilation for radicals and diradicals. *International Journal of Quantum Chemistry*, 103(1):1–9, 2005.

[185] S. Pittalis, S. Kurth, and E. K. U. Gross. On the degeneracy of atomic states within exact-exchange (spin-) density functional theory. *The Journal of Chemical Physics*, 125(8):084105, 2006.

[186] Tom Ziegler, Arvi Rauk, and Evert J. Baerends. On the calculation of multiplet energies by the hartree-fock-slater method. 43(3):261–271, 1977.

[187] Louis Noodleman. Valence bond description of antiferromagnetic coupling in transition metal dimers. *The Journal of Chemical Physics*, 74(10):5737–5743, 1981.

[188] Jean-Marie Mouesca, Jun L. Chen, Louis Noodleman, Donald Bashford, and David A. Case. Density functional/poisson-boltzmann calculations of redox potentials for iron-sulfur clusters. *Journal of the American Chemical Society*, 116(26):11898–11914, 1994.

[189] Sebastian Sinnecker, Frank Neese, Louis Noodleman, and Wolfgang Lubitz. Calculating the electron paramagnetic resonance parameters of exchange coupled transition metal complexes using broken symmetry density functional theory: Application to a Mn^{III}/Mn^{IV} model compound. *Journal of the American Chemical Society*, 126(8):2613–2622, 2004.

[190] K. Yamaguchi, F. Jensen, A. Dorigo, and K. N. Houk. A spin correction procedure for unrestricted hartree-fock and møller-plesset wavefunctions for singlet diradicals and polyradicals. *Chemical Physics Letters*, 149(5–6):537–542, 9 1988.

[191] T. Soda, Y. Kitagawa, T. Onishi, Y. Takano, Y. Shigeta, H. Nagao, Y. Yoshioka, and K. Yamaguchi. Ab initio computations of effective exchange integrals for H-H, H-He-H and Mn_2O_2 complex: comparison of broken-symmetry approaches. *Chemical Physics Letters*, 319(3-4):223–230, 3 2000.

[192] Ilaria Ciofini and Claude A. Daul. DFT calculations of molecular magnetic properties of coordination compounds. *Coordination Chemistry Reviews*, 238-239(0):187–209, 3 2003.

[193] Frank Neese. Prediction of molecular properties and molecular spectroscopy with density functional theory: From fundamental theory to exchange-coupling. *Coordination Chemistry Reviews*, 253(5-6):526–563, 3 2009.

[194] JN Harvey. *Struct. Bond.*, 112(151), 2004.

[195] Kerstin Andersson, Per-ke Malmqvist, and Björn O. Roos. Second-order perturbation theory with a complete active space self-consistent field reference function. *The Journal of Chemical Physics*, 96(2):1218–1226, 1992.

[196] JT Frey and DJ Doren. Tubegen version 3.3. Univerity of Delaware, Newark, DE, 2005.

[197] Yan Zhao and Donald G Truhlar. MN-GFM version 4.1. University of Minnesota, Minneapolis, 2008.

[198] MJEA Frisch, GW Trucks, Hs B Schlegel, GE Scuseria, MA Robb, JR Cheeseman, G Scalmani, V Barone, B Mennucci, GA Petersson, et al. Gaussian 03, revision d.01. *Gaussian Inc., Wallingford, CT*, 200, 2009.

[199] Gunnar Karlström, Roland Lindh, Per-ke Malmqvist, Björn O Roos, Ulf Ryde, Valera Veryazov, Per-Olof Widmark, Maurizio Cossi, Bernd Schimmelpfennig, Pavel Neogrady, and Luis Seijo. MOLCAS: a program package for computational chemistry. *Computational Materials Science*, 28(2):222–239, 10 2003.

[200] Yan Zhao and Donald G. Truhlar. A density functional that accounts for medium-range correlation energies in organic chemistry. *Organic Letters*, 8(25):5753–5755, 2006.

[201] Matthew D. Wodrich, Clémence Corminboeuf, Peter R. Schreiner, Andrey A. Fokin, and Paul von Ragué Schleyer. How accurate are DFT treatments of organic energies? *Organic Letters*, 9(10):1851–1854, 2007.

[202] Martin Kabeláč, Haydee Valdes, Edward C Sherer, Christopher J Cramer, and Pavel Hobza. Benchmark RI-MP2 database of nucleic acid base trimers: performance of different density functional models for prediction of structures and binding energies. *Physical Chemistry Chemical Physics*, 9(36):5000–5008, 2007.

[203] Yan Zhao and Donald G. Truhlar. Size-selective supramolecular chemistry in a hydrocarbon nanoring. *Journal of the American Chemical Society*, 129(27):8440–8442, 2007.

[204] A. D. Becke. Density-functional exchange-energy approximation with correct asymptotic behavior. *Phys. Rev. A*, 38:3098–3100, Sep 1988.

[205] Chengteh Lee, Weitao Yang, and Robert G. Parr. Development of the colle-salvetti correlation-energy formula into a functional of the electron density. *Phys. Rev. B*, 37:785–789, Jan 1988.

[206] Axel D. Becke. Density-functional thermochemistry. III. the role of exact exchange. *The Journal of Chemical Physics*, 98(7):5648–5652, 1993.

[207] P. J. Stephens, F. J. Devlin, C. F. Chabalowski, and M. J. Frisch. Ab initio calculation of vibrational absorption and circular dichroism spectra using density functional force fields. *The Journal of Physical Chemistry*, 98(45):11623–11627, 1994.

[208] Christopher J. Cramer, Marta Włoch, Piotr Piecuch, Cristina Puzzarini, and Laura Gagliardi. Theoretical models on the Cu_2O_2 torture track: Mechanistic implications for oxytyrosinase and small–molecule analogues. *The Journal of Physical Chemistry A*, 110(5):1991–2004, 2006.

[209] Christopher J. Cramer, Armagan Kinal, Marta Włoch, Piotr Piecuch, and Laura Gagliardi. Theoretical characterization of end-on and side-on peroxide coordination in ligated Cu_2O_2 models. *The Journal of Physical Chemistry A*, 110(40):11557–11568, 2006.

[210] John L. Lewin, David E. Heppner, and Christopher J. Cramer. Validation of density functional modeling protocols on experimental bis(μ-oxo)/μ-η^2:η^2-peroxo dicopper equilibria. 12(8):1221–1234, 2007.

[211] Per Åke Malmqvist, Kristine Pierloot, Abdul Rehaman Moughal Shahi, Christopher J. Cramer, and Laura Gagliardi. The restricted active space followed by second-order perturbation theory method: Theory and application to the study of CuO_2 and Cu_2O_2 systems. *The Journal of Chemical Physics*, 128(20):–, 2008.

Appendix A

Equations[1]

A.1 Gas-phase Enthalpies of Formation

A.1.1 Homodesmotic Formalism: Arenes

$$n\,C_6H_5X \longrightarrow (n-1)\,C_6H_6 + C_6H_{6-n}X_n$$

$$\Delta_r H^\circ = (n-1)\Delta_f H^\circ(C_6H_6) + \Delta_f H^\circ(C_6H_{6-n}X_n) - n\Delta_f H^\circ(C_6H_5X)$$

$$\Delta_f H^\circ(C_6H_{6-n}X_n) = \Delta_r H^\circ_{(DFT)} - (n-1)\Delta_f H^\circ_{(exp.)}(C_6H_6) + n\Delta_f H^\circ_{(exp.)}(C_6H_5X)$$

[1] **Adapted with permission from Sadowsky, D.; McNeill, K.; Cramer, C. J. Thermochemical Factors Affecting the Dehalogenation of Aromatics. *Environ. Sci. Technol.*, 2013, *47*, 14194–14203. Copyright 2013 American Chemical Society.**

$$\sigma_{\Delta_f H^\circ(C_6H_{6-n}X_n)} = \sqrt{(n-1)^2\sigma^2_{\Delta_f H^\circ(C_6H_6)} + n^2\sigma^2_{\Delta_f H^\circ(C_6H_5X)}}$$

A.1.2 Homodesmotic Formalism: Radicals

$$\mathrm{C_6H_5^\bullet} + n\,\mathrm{C_6H_5X} \longrightarrow n\,\mathrm{C_6H_6} + \mathrm{C_6H_{5-n}X_n^\bullet}$$

$$\Delta_r H^\circ = n\Delta_f H^\circ(C_6H_6) + \Delta_f H^\circ(C_6H_{5-n}X_n^\bullet) - \Delta_f H^\circ(C_6H_5^\bullet) - n\Delta_f H^\circ(C_6H_5X)$$

$$\Delta_f H^\circ(C_6H_{5-n}X_n^\bullet) = \Delta_r H^\circ_{(DFT)} - n\Delta_f H^\circ_{(exp.)}(C_6H_6) + \Delta_f H^\circ_{(exp.)}(C_6H_5^\bullet) + n\Delta_f H^\circ_{(exp.)}(C_6H_5X)$$

$$\sigma_{\Delta_f H^\circ(C_6H_{5-n}X_n^\bullet)} = \sqrt{n^2\sigma^2_{\Delta_f H^\circ(C_6H_6)} + \sigma^2_{\Delta_f H^\circ(C_6H_5^\bullet)} + n^2\sigma^2_{\Delta_f H^\circ(C_6H_5X)}}$$

A.1.3 Hyperhomodesmotic Formalism: Arenes

$$6(n-q)\,\mathrm{C_6H_5X} + q\,\mathrm{C_6X_6} \longrightarrow (6n-5q-6)\,\mathrm{C_6H_6} + 6\,\mathrm{C_6H_{6-n}X_n}$$

$$\Delta_r H^\circ = (6n-5q-6)\Delta_f H^\circ(C_6H_6) + 6\Delta_f H^\circ(C_6H_{6-n}X_n) - 6(n-q)\Delta_f H^\circ(C_6H_5X) - q\Delta_f H^\circ(C_6X_6)$$

$$\Delta_f H^\circ(C_6H_{6-n}X_n) = \frac{1}{6}\Delta_r H^\circ_{(DFT)} - \frac{6n-5q-6}{6}\Delta_f H^\circ_{(exp.)}(C_6H_6) + (n-q)\Delta_f H^\circ_{(exp.)}(C_6H_5X) + \frac{q}{6}\Delta_f H^\circ_{(exp.)}(C_6X_6)$$

$$\sigma_{\Delta_f H^\circ(C_6H_{6-n}X_n)} = \sqrt{\frac{(6n-5q-6)^2}{36}\sigma^2_{\Delta_f H^\circ(C_6H_6)} + (n-q)^2\sigma^2_{\Delta_f H^\circ(C_6H_5X)} + \frac{q^2}{36}\sigma^2_{\Delta_f H^\circ(C_6X_6)}}$$

A.1.4 Hyperhomodesmotic Formalism: Radicals

$$6\,\mathrm{C_6H_5^\bullet} + 6(n-q)\,\mathrm{C_6H_5X} + q\,\mathrm{C_6X_6} \longrightarrow (6n-5q)\,\mathrm{C_6H_6} + 6\,\mathrm{C_6H_{5-n}X_n^\bullet}$$

$$\Delta_r H^\circ = (6n-5q)\Delta_f H^\circ(C_6H_6) + 6\Delta_f H^\circ(C_6H_{5-n}X_n^\bullet) - 6\Delta_f H^\circ(C_6H_5^\bullet) - 6(n-q)\Delta_f H^\circ(C_6H_5X) - q\Delta_f H^\circ(C_6X_6)$$

$$\Delta_f H^\circ(C_6H_{5-n}X_n^\bullet) = \frac{1}{6}\Delta_r H^\circ_{(DFT)} - \frac{6n-5q}{6}\Delta_f H^\circ_{(exp.)}(C_6H_6) + \Delta_f H^\circ_{(exp.)}(C_6H_5^\bullet) + (n-q)\Delta_f H^\circ_{(exp.)}(C_6H_5X) + \\ + \frac{q}{6}\Delta_f H^\circ_{(exp.)}(C_6X_6)$$

$$\sigma_{\Delta_f H^\circ(C_6H_{5-n}X_n^\bullet)} = \sqrt{\frac{(6n-5q)^2}{36}\sigma^2_{\Delta_f H^\circ(C_6H_6)} + \sigma_{\Delta_f H^\circ(C_6H_5^\bullet)} + (n-q)^2\sigma^2_{\Delta_f H^\circ(C_6H_5X)} + \frac{q^2}{36}\sigma^2_{\Delta_f H^\circ(C_6X_6)}}$$

A.2 Aqueous Gibbs Free Energies of Formation

A.2.1 Arenes

$$\Delta_r G^\circ_{(aq.)} = (n-1)\Delta_f G^\circ_{(aq.)}(C_6H_6) + \Delta_f G^\circ_{(aq.)}(C_6H_{6-n}X_n) - n\Delta_f G^\circ_{(aq.)}(C_6H_5X)$$

$$\Delta_f G^\circ_{(aq.)}(C_6H_{6-n}X_n) = \Delta_r G^\circ_{(aq.,DFT)} - (n-1)\Big(\Delta_f H^\circ_{(g,exp.)}(C_6H_6) - TS_{(g,DFT)}(C_6H_6) + \Delta_{solv}G^\circ_{(exp.)}(C_6H_6)\Big) + \\ + n\Big((\Delta_f H^\circ_{(g,exp.)}(C_6H_5X) - TS_{(g,DFT)}(C_6H_5X) + \Delta_{solv}G^\circ_{(exp.)}(C_6H_5X)\Big)$$

$$\sigma_{\Delta_f G^\circ_{(aq.)}(C_6H_{6-n}X_n)} = \sqrt{(n-1)^2\Big(\sigma^2_{\Delta_f H^\circ_{(g)}(C_6H_6)} + \sigma^2_{\Delta_{solv}G^\circ(C_6H_6)}\Big) + n^2\Big(\sigma^2_{\Delta_f H^\circ_{(g)}(C_6H_5X)} + \sigma^2_{\Delta_{solv}G^\circ(C_6H_5X)}\Big)}$$

A.2.2 Radicals

$$\mathrm{C_6H_5^\bullet} + n\,\mathrm{C_6H_5X} \longrightarrow n\,\mathrm{C_6H_6} + \mathrm{C_6H_{5-n}X_n^\bullet}$$

$$\Delta_f G^\circ_{(aq.)}(C_6H_{5-n}X_n^\bullet) = \Delta_r G^\circ_{(aq.,DFT)} - n\Big(\Delta_f H^\circ_{(g,exp.)}(C_6H_6) - TS_{(g,DFT)}(C_6H_6) + \Delta_{solv}G^\circ_{(exp.)}(C_6H_6)\Big) + \Big(\Delta_f H^\circ_{(g,exp.)}(C_6H_5^\bullet) - \\ - TS_{(g,DFT)}(C_6H_5^\bullet) + \Delta_{solv}G^\circ_{(DFT)}(C_6H_5^\bullet)\Big) + n\Big(\Delta_f H^\circ_{(g,exp.)}(C_6H_5X) - TS_{(g,DFT)}(C_6H_5X) + \Delta_{solv}G^\circ_{(exp.)}(C_6H_5X)\Big)$$

$$\Delta_f G^\circ_{(aq.)}(C_6H_{5-n}X_n^\bullet) = \Delta_r G^\circ_{(aq.,DFT)} - n\Big(\Delta_f H^\circ_{(g,exp.)}(C_6H_6) - TS_{(g,DFT)}(C_6H_6) + \Delta_{solv}G^\circ_{(exp.)}(C_6H_6)\Big) + \Big(\Delta_f H^\circ_{(g,exp.)}(C_6H_5^\bullet) - \\ - TS_{(g,DFT)}(C_6H_5^\bullet) + \Delta_{solv}G^\circ_{(DFT)}(C_6H_5^\bullet)\Big) + n\Big(\Delta_f H^\circ_{(g,exp.)}(C_6H_5X) - TS_{(g,DFT)}(C_6H_5X) + \Delta_{solv}G^\circ_{(exp.)}(C_6H_5X)\Big)$$

$$\sigma_{\Delta_f G^\circ_{(aq.)}(C_6H_{5-n}X^\bullet_n)} = \sqrt{n^2\left(\sigma^2_{\Delta_f H^\circ_{(g)}(C_6H_6)} + \sigma^2_{\Delta_{solv}G^\circ(C_6H_6)}\right) + \sigma^2_{\Delta_f H^\circ_{(g)}(C_6H_5^\bullet)} + n^2\left(\sigma^2_{\Delta_f H^\circ_{(g)}(C_6H_5X)} + \sigma^2_{\Delta_{solv}G^\circ(C_6H_5X)}\right)}$$

Appendix B

Validation of the Use of a Non-Relativistic Model Chemistry[1]

Single point M06-2X, MP2, and CCSD(T) calculations with a 2nd order scalar DKH Hamiltonian and the aug-cc-pVTZ-DK basis set are carried out at the geometries optimized with the non-relativistic M06-2X/6-311+G(3df,2p) model chemistry. From these calculations, and from frequency calculations at the M06-2X/6-311+G(3df,2p) level of theory, the standard enthalpies of formation of two chlorinated and brominated benzenes are predicted through the homodesmotic reaction in Eq. B.1. In addition, the standard enthalpies of atomization for the same halogenated benzenes, as well as for benzene, chlorobenzene, and bromobenzene, are predicted (the enthalpy of atomization

[1] **Adapted with permission from Sadowsky, D.; McNeill, K.; Cramer, C. J. Thermochemical Factors Affecting the Dehalogenation of Aromatics. *Environ. Sci. Technol.*, 2013, *47*, 14194–14203. Copyright 2013 American Chemical Society.**

here is taken as the negative enthalpy of reaction for the reaction in Eq. B.2). The predictions are reported in Tables B.1 and B.2, respectively, along with the mean signed differences and root mean squared differences of each set of predictions from the relativistic CCSD(T) predictions. The results show that while the consideration of relativistic effects makes a significant impact on enthalpies of atomization, its impact on enthalpies of formations predicted through a homodesmotic reaction is much more subtle. This suggests that, while relativistic Hamiltonians are probably necessary for the direct predictions of most chemical properties, a non-relativistic model chemistry probably yields acceptable results for chemical properties that can be predicted through a careful use of experimental data with a homodesmotic formalism. The results also suggest that a more sophisticated treatment of electron correlation might be a better way of systematically improving the model chemistry used here than the consideration of relativistic effects with the DFT method.

$$n\,\mathrm{C_6H_5Br} \longrightarrow (n-1)\,\mathrm{C_6H_6} + \mathrm{C_6H_{6-n}Br_n} \tag{B.1}$$

$$6\,\mathrm{C}(^3P) + (6-n)\,\mathrm{H}(^2S) + n\,\mathrm{Br}(^2P) \longrightarrow \mathrm{C_6H_{6-n}Br_n} \tag{B.2}$$

Table B.1: Standard enthalpies of formation (in kcal/mol) of selected halogenated benzenes.

	non-relativistic	2nd order scalar relativistic		
	DFT	DFT	MP2	CCSD(T)
1,2-dichlorobenzene	5.9	6.2	5.9	5.7
1,3,5-trichlorobenzene	0.2	0.8	-0.2	-0.5
1,2-dibromobenzene	31.0	31.3	30.8	30.6
1,3,5-tribromobenzene	37.9	38.5	37.1	36.9
MSD	0.6	1.0	0.2	0.0
RMSD	0.7	1.1	0.3	0.0

Table B.2: Standard enthalplies of atomization (in kcal/mol) of selected halogenated benzenes.

	non-relativistic	2nd order scalar relativistic		
	DFT	DFT	MP2	CCSD(T)
benzene	1321.1	1318.4	1325.0	1288.8
chlorobenzene	1307.9	1303.6	1314.4	1271.5
1,2-dichlorobenzene	1293.9	1287.7	1302.3	1253.6
1,3,5-trichlorobenzene	1279.1	1270.9	1290.1	1235.1
bromobenzene	1291.7	1287.9	1306.9	1263.2
1,2-dibromobenzene	1261.7	1256.5	1288.3	1237.4
1,3,5-tribromobenzene	1230.6	1224.0	1269.0	1210.6
MSD	-32.1	-25.6	-53.2	0.0
RMSD	33.7	27.3	53.4	0.0